SAND2019-11296R

FY19 Status Report: SNL Research into Stress Corrosion Cracking of SNF Dry Storage Canisters

Spent Fuel and Waste Disposition

Prepared for
US Department of Energy
Spent Fuel and Waste Science and Technology

Schaller R., Knight A., Bryan C., and Schindelholz E.
Sandia National Laboratories

September 20, 2019
Milestone No. M2SF-19SN010201049
SAND2019-XXXX

Sandia National Laboratories is a multimission laboratory managed and operated by National Technology & Engineering Solutions of Sandia, LLC, a wholly owned subsidiary of Honeywell International Inc., for the U.S. Department of Energy's National Nuclear Security Administration under contract DE-NA0003525.

Prepared by
Sandia National Laboratories
Albuquerque, New Mexico 87185 and Livermore, California 94550

Sandia National Laboratories is a multimission laboratory managed and operated by National Technology and Engineering Solutions of Sandia, LLC, a wholly owned subsidiary of Honeywell International, Inc., for the U.S. Department of Energy's National Nuclear Security Administration under contract DE-NA0003525.

Sandia National Laboratories

SUMMARY

This progress report describes work done in FY19 at Sandia National Laboratories (SNL) to assess the localized corrosion performance of container/cask materials used in the interim storage of spent nuclear fuel (SNF). Of particular concern is stress corrosion cracking (SCC), by which a through-wall crack could potentially form in a canister outer wall over time intervals that are shorter than possible dry storage times. Work in FY19 refined our understanding of the chemical and physical environment on canister surfaces and evaluated the relationship between chemical and physical environment and the form and extent of corrosion that occurs.

Work to define the chemical and physical environment that could develop on storage canister surfaces in near-marine environments included continued characterization of samples from experiments run in FY18, to evaluate the thermal stability of magnesium chloride brines, representative of the first brines to form when sea-salts deliquesce, with the specific goal of understanding and interpreting results of sea-salt and magnesium chloride corrosion experiments carried out under accelerated conditions. The experiments confirmed that magnesium chloride brines, and by extension, low RH sea-salt deliquescent brines, are not stable at elevated temperatures, losing chloride *via* degassing of HCl and conversion to Mg-hydroxychlorides and carbonates. The experiments were carried out on an inert substrate to eliminate the effects of corrosion reactions, simulating brine stabilities in the absence of corrosion. In FY18, analysis of salts recovered from actively corroding metal samples showed that corrosion also drives conversion of magnesium chloride less deliquescent hydroxychloride phases. Samples collected from additional corrosion experiments in FY19 confirmed these reactions, and three different Mg-hydroxide or hydroxychloride phases have now been identified as forming. This process has significant implications on corrosion, as the secondary phases are less deliquescent than magnesium chloride; the conversion reaction results in decreases in brine volume, and potentially ultimately results in brine dry-out. To better predict the stability of Mg-chloride (and sea-salt) brines, SNL is working to develop a thermodynamic database for known magnesium hydroxide, chloride, and hydroxychloride phases. Thermodynamic and solubility data, available for a few phases, has been compiled, and a component contribution method has been used to estimate thermodynamic data for the other Mg phases of interest; those data are being refined by fitting of available solubility data.

Experimental efforts in FY19 to understand the relationship between surface environment and corrosion damage focused on four thrust areas: (1) generation of temporal statistical pitting data as function of environment; (2) hierarchal identification of features controlling pit-to-crack transitions; (3) definition of the surface environment-electrochemical relationship driving pitting and SCC; (4) definition of relative governance on material condition and stress relative to surface environmental conditions on electrochemical kinetics and SCC susceptibility. In FY19, work to characterize pitting damage and surface chemistry on 304L coupons loaded with sea-salt and exposed to ISFI-relevant fixed RH, T conditions continued. The final samples, exposed for two years in RH chambers, have been collected. Working with the Ohio State University (OSU), we have used optical profilometry to generate initial pit datasets for coupon exposure times up to 1.5 years. These data will be used to directly test the maximum pit size model incorporated into the SNL SCC model, and to develop statistical models in collaboration with Colorado School of Mines (CSM). Regarding (2), and in collaboration with OSU, experiments have been initiated to identify pit-to-crack transition features. Accomplishments include deposition of salt and exposure of tensile test specimens to the environmental conditions used in thrust (1) for up to six months, followed by an initial tensile loading experiment to identify pit features that might provide focal points for SCC initiation. Additionally, we have developed and tested a method for periodic loading of the specimens while under said environments. Regarding (3), the cathodic electrochemical kinetics that drive corrosion on stainless steel were measured for NaCl and $MgCl_2$ brines as analogs to expected brines compositions on the canisters at the upper end of expected ISFSI surface humidity range. These data were incorporated into SNL's SCC model and findings communicated in a peer-reviewed journal publication. Additional work with surrogate cathodic brines (without the influence of chlorides) was also

carried out. Work in area (4) included completion of 4-point bend experiments using stressed 304L bars loaded with sea salt and exposed to 35%RH, 50°C conditions in collaboration with CSM. The pit distribution on one of these bars was analyzed via optical profilometry with initial results suggesting pit frequency, depth and diameter was independent on material stress state within expected canister conditions. Comparisons to electrochemical investigations of similarly stressed 304L bars corroborate this finding for canister-relevant brines. Finally, we completed exposure of a salt-loaded mockup canister plates to elevated RH, T conditions to determine what portions of the canister may be most susceptible to SCC and their relationship to material condition and mechanical environment. Those samples are currently being evaluated for SCC cracks using three different NDE methods.

ACKNOWLEDGEMENTS

The authors acknowledge the contributions to this report from Mike Melia Jason Taylor, Jacob Carpenter, Angelica de Valle, Ryan Katona, Carlos Jove-Colon, Bonnie McKenzie, Steve Meserole, Cathy Alam, Mark Rodriguez, and Tony Ohlhausen, all at SNL; Rob Kelly at the University of Virginia; Jen Locke and Tim Weirich at Ohio State University; John Plumley and Fernando Garzon at the University of New Mexico, Zhenzhen Yu at the Colorado School of Mines, and Robert Kelly at the University of Virginia.

This page is intentionally left blank.

CONTENTS

LIST OF FIGURES

LIST OF TABLES

This page is intentionally left blank.

ACRONYMS

ASW	artificial seawater
CGR	crack growth rate
CRIEPI	[Japanese] Central Research Institute of the Electric Power Industry
CSM	Colorado School of Mines
DCPD	direct current potential drop
DOE	US Department of Energy
EDS	energy dispersive [X-ray] spectroscopy
EPRI	Electric Power Research institute
FCRD	Fuel Cycle Research and Development
FY	fiscal year
GWB	The Geochemist's Workbench
HER	hydrogen evolution reaction
IC	ion chromatography
IRP	integrated research project
ISFSI	independent spent fuel storage installation
NEUP	Nuclear Energy University Programs
NRC	Nuclear Regulatory Commission
ORR	oxygen reduction reaction
OSU	Ohio State University
PNNL	Pacific Northwest National Laboratory
RDE	rotating disc electrode
RH	relative humidity
SCC	stress corrosion cracking
SEM	scanning electron microscope
SFWST	Spent Fuel and Waste Science and Technology
SNF	spent nuclear fuel
SNL	Sandia National Laboratory
SRNL	Savannah River National Laboratory
SS	stainless steel
TOF-SIMS	time-of-flight secondary ion mass spectrometry
UVA	University of Virginia
XRD	X-ray Diffraction

This page is intentionally left blank.

SPENT FUEL AND WASTE SCIENCE AND TECHNOLOGY

SNL FY19 STATUS REPORT: RESEARCH INTO STRESS CORROSION CRACKING OF SPENT NUCLEAR FUEL DRY STORAGE CANISTERS

1. INTRODUCTION

In dry storage, spent nuclear fuel (SNF) is commonly stored in welded stainless steel (SS) canisters enclosed in passively-ventilated overpacks. As outside air advects through the overpacks, dust accumulates on the canister surfaces. Over time, as the SNF cools, the canister surface temperatures drop to the point that salts within that dust will deliquesce to form concentrated brines. If the salts contain aggressive species such as chloride, then the resulting brine can cause localized corrosion—pitting—to occur. In the presence of sufficient tensile stresses in the metal, the pitting can eventually convert to stress corrosion cracking (SCC), which over time could penetrate the canister wall. The risk of corrosion and SCC is greatest in near-marine settings, where chloride-rich sea-salt aerosols are deposited on the canister surface. Over the past few years, Sandia National Laboratories (SNL) has worked to develop a probabilistic model for stress corrosion cracking which utilizes mechanistically-based submodels to describe individual processes and events that occur during canister ageing and that could eventually lead to canister SCC (Figure 1). However, due to lack of data, the current model framework contains numerous assumptions and oversimplifications, many with insufficient mechanistic basis. Current SCC work at SNL focuses on acquiring data for improved submodel development, focusing mostly on determining the underlying mechanisms that govern (1) brine evolution, both before and after initiation of corrosion; (2) the corrosion processes of pitting, SCC crack initiation, and SCC crack growth. This includes developing high-quality data for salt compositions and deposition rates at ISFSI sites and for brine compositions in the evolving canister surface environment, and statistical pitting and SCC initiation and growth data for canister-relevant conditions. By improving submodel parameterization and validation, this work will reduce uncertainty in our estimates of the timing and occurrence of SCC.

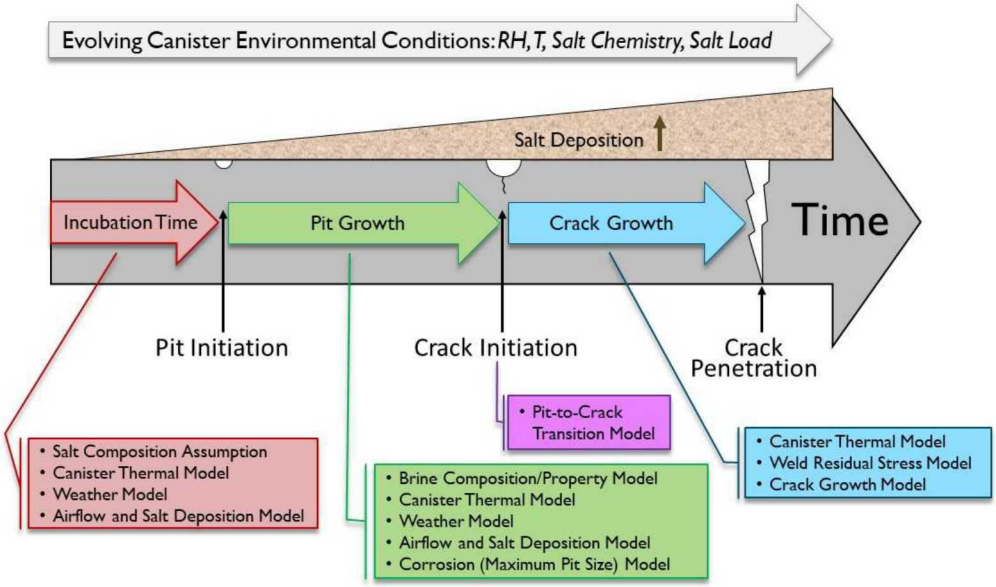

Figure 1. Probabilistic Model for SNF Dry Storage Canister Stress Corrosion Cracking.

1.1 Background

A timeline for SCC of spent nuclear fuel canisters in dry storage is shown in Figure 2. Several important events and processes occur during the development of through-wall SCC and understanding the timing of event initiation and the rates of these processes is critical to accurate evaluation of possible SCC penetration times. These parameters are highly dependent upon the evolving physical and chemical environment on the canister surface, and on the canister material properties, including composition, surface finish, and weld-related microstructure and residual stress levels. SNL and several collaborators are working to understand these dependencies, and their effect on potential canister penetration rates by SCC.

Once a canister is placed in a ventilated overpack, dust and salt aerosols begin to be deposited on the canister surface. Initially, canister surface temperatures may be too high to permit salt deliquescence or even development of adsorbed water layers on salts, and localized corrosion cannot occur. But as the canister cools, surface relative humidity (RH) values increase; eventually, salts will deliquesce and a brine forms on the metal surface, permitting corrosion to occur. Once a brine is present, corrosion may be delayed for a time, but this period is likely to be insignificant relative to storage time intervals. The period following emplacement and prior to corrosion is known as the incubation period and is a function of the physical environment—the temperature, RH, and salt load on the canister surface. The chemical composition of the deposited salts is also important, as it controls both the corrosiveness of the brine and the RH at which deliquescence occurs. SNL is evaluating the physical conditions and the chemical environment on the canister surface, both prior to and after initiation of corrosion. Of particular interest is the long-term stability of brines formed by sea-salt deliquescence on the heated canister surface, and the effect of atmospheric exchange reactions and corrosion reactions.

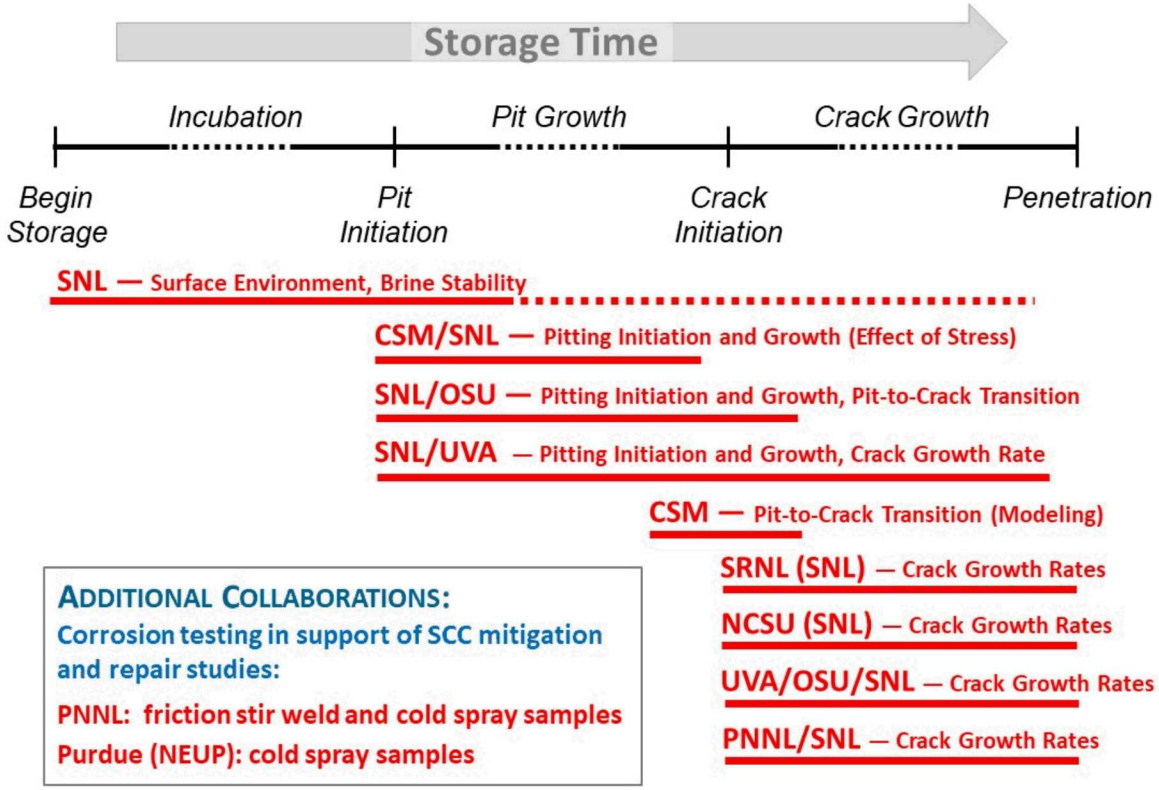

Figure 2. Timeline for stress corrosion cracking, showing current experimental work being carried out by SNL and collaborators.

Once deliquescence occurs, if the deliquescent brine is chemically aggressive (e.g., chloride-rich), then pitting corrosion will initiate. Pitting initiation and pit growth rates, and possible limitations on pit growth, are strongly controlled by environmental factors such as temperature, RH, and salt load, but also by material properties, including composition, surface finish, microstructure, and stress level. SNL has several collaborations with university groups evaluating aspects of pitting initiation and growth as a function of environmental conditions and material properties. SNL is collaborating with the Colorado School of Mines (CSM) as part of a DOE Integrated Research Project (IRP) to evaluate the effect of stress on pit growth rates; this work was completed in FY19. SNL is working with Ohio State University (OSU) to evaluate pit initiation and growth on unstrained samples with different surface finishes. SNL is also evaluating the effect of brine composition on the cathodic current generated in the region surrounding the pit, and the anodic current demand due to dissolution within the pit. In the SNL probabilistic SCC model, these values are used to determine the maximum pit size that can occur for a given set of environmental conditions (Chen and Kelly 2010). This work is being carried out in collaboration with the University of Virginia (UVA).

In the presence of tensile stresses, the current assumption is that pits that grow sufficiently large will eventually initiate SCC cracks. Existing models relate pit depth to crack initiation through the calculated crack tip stress intensity factor (e.g., Kondo, 1989; Turnbull et al., 2006). However, this approach must be implemented stochastically, and makes broad assumptions about the shape of the pit. To develop a more realistic relationship between pitting and crack initiation, SNL is working with OSU to experimentally evaluate conditions of pit-to-crack transition under controlled conditions. SNL is also evaluating pitting and crack initiation using large weld samples from a full-diameter canister mockup that SNL used to characterize weld residual stresses (Enos and Bryan, 2016).

Once a SCC crack initiates, the rate of crack growth will be controlled by the temperature and chemical environment, as well as, possibly, the salt surface load. The tensile stress profile through the metal is also important, as it is combined the depth of the crack to determine the crack tip stress intensity factor (Newman and Raju, 1979; Newman and Raju, 1981). SNL is working with colleagues at North Carolina State University (part of the CSM-led IRP); with Savannah River National Laboratory (SRNL); and with Pacific Northwest National Laboratory (PPNL) to measure crack growth rates as a function of canister surface environment (brine composition and temperature). For these efforts, SNL's role has largely been to help define the appropriate environments for testing, and to help interpret test results. However, in FY19, SNL installed load frames, and began its own testing, in collaboration with OSU, to determine the effects of canister surface environment on crack initiation and growth rates.

Finally, as industry begins to move towards strategies for mitigation and repair of SCC cracks, should they be observed on SNF dry storage canisters, SNL is supporting work to develop repair strategies. We are working with PNNL to evaluate simulated friction stir weld and cold spray repairs for compatibility and corrosion resistance. That work was recently published in the Spent Fuel and Waste Science and technology (SFWST) report *Corrosion Testing of Friction Stir Welded 304L Stainless Steel* (Schindelholz et al., 2019) and is not discussed here. Moreover, SNL is working as a collaborator in a Nuclear Energy University Programs (NEUP) project led by Purdue University to evaluate the corrosion properties of cold-spray repairs. This funding does not come from the SFWST) program, but the collaboration will allow us to leverage our funding for both projects.

1.2 FY19 Tasks and Current Status

Prediction of SCC formation initiation and growth requires both (1) a statistical description of the inherently stochastic process of pit formation, growth and conversion to a SCC crack under conditions (material and surface environment) representative of fielded canisters; and (2) a deterministic/mechanistic understanding of environment-material-electrochemical interrelationships. Purely statistical approaches provide a means of quantifying variability and uncertainty in material and surface condition but cannot be

confidently extrapolated beyond the range of conditions or the time interval under which the data were collected without a mechanistic understanding of the processes involved. Mechanistic studies serve to inform and provide confidence in statistical extrapolation for prediction of these processes. SNL, the IRP and other collaborators are pursuing both avenues for prediction of SCC behavior of used fuel nuclear waste containers at independent spent fuel storage installation (ISFSI) sites. Challenges common to both approaches are lack of data on canister surface environment, and an incomplete understanding of the relationships between environment, material, and corrosion response under field-relevant conditions. This challenge manifests itself in selection of appropriate environmental and material inputs for models, development of experiments relating environment/material to damage rates and distributions, and utilization of experimental data as inputs and benchmarking tools for predictive models.

Efforts at SNL take advantage of a unique combination of expertise and capabilities in geochemistry, surface science, metallurgy and electrochemistry to:

- Advance the quantitative definition of the physical and chemical environment on the surface of SNF interim storage canisters, and its temporal and spatial evolution to inform modeling and relevant laboratory experiments.
- Rigorously characterize the relationship between the surface environment and damage distributions and rates, with emphasis on electrochemical kinetics.
- Quantify the impact of materials variability (stress, strain, microstructure, surface finish) on electrochemical corrosion processes from pitting initiation to stress corrosion cracking.
- Quantify the effect of environmental controls (temperature, RH, salt composition, and load) and the evolution of brine properties on stress corrosion crack growth rates.

These efforts will provide knowledge and data necessary for relating canister-relevant surface environments and material conditions to corrosion processes. This understanding will support efforts at SNL and elsewhere to design and carry out relevant laboratory corrosion/SCC tests and to interpret the results of those tests. Ultimately, it will support improved modeling of storage canister performance during long-term interim storage (Figure 2).

Sandia research focuses on the thrust areas listed above. Testing is done at experimental conditions (salt compositions and loading, humidity, temperature) that bound expected canister surface conditions in marine coastal environments, which are expected to be the most severe case for SCC.

2. BRINE STABILITY ON HEATED STORAGE CANISTER SURFACES

2.1 Stability of Magnesium Chloride Brines

For the past two years, SNL has been evaluating the stability of magnesium chloride brines, the first brines to form as canisters cool and sea-salt aerosols deliquesce on the canister surface. Initial experiments (Schindelholz *et al.*, 2017) were performed at 48°C and 40% RH, conditions close to the highest temperatures at which bischofite ($MgCl_2$:$6H_2O$) could deliquesce in a real canister environment. These experiments showed that under these conditions, the brine would degas HCl and absorb CO_2, slowly converting to carbonate. Because of the low temperature and the low air flow rates through the environmental chamber, the degree of conversion was small over the 8-week duration of the experiment. However, the experiment demonstrated that the $MgCl_2$ brine was not stable under those conditions. In a second experiment, $MgCl_2$ brine stability was evaluated at 80°C and 35% RH for a duration of 8 weeks. Initial results were presented in last year's SFWST research summary (Bryan and Schindelholz, 2018). Conversion of the Mg-Cl brine droplets was initially verified by scanning electron microscope/energy dispersive X-ray spectroscopy (SEM/EDS) analysis. An example from one of the 8-week samples is shown in Figure 3. Over time, brine droplets on the inert substrate (25 mm diameter silicon wafers) slowly converted to a fibrous solid phase, losing chlorine, while oxygen concentrations and to a lesser degree, carbon concentrations, increased. Smaller droplets, with a large surface area to volume ratio, converted more thoroughly than larger droplets. Moreover, conversion was localized on the wafer, with some areas converting more than others. The fibrous phase was identified by X-ray diffraction analysis (XRD) as a magnesium hydroxychloride phase of the approximate composition $2Mg(OH)_2$:$MgCl_2$:$4H_2O$ (known in the literature as the 2-1-4 phase).

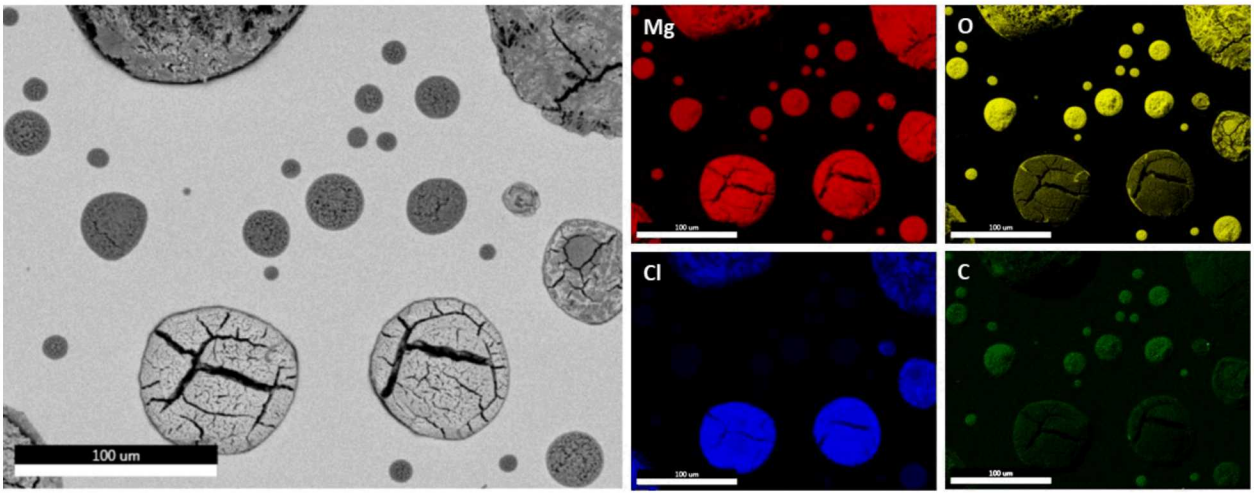

Figure 3. High magnification SEM BSE image and EDS element maps of 8-week $MgCl_2$ sample. Smaller, darker droplets are depleted in chloride and enriched in oxygen and carbon.

SEM/EDS analysis of small droplets on a matrix is subject to potential artifacts, and the relative degree of conversion, as well as the presence of small amounts of carbon as carbonate, required verification. For this reason, additional analyses were carried out using time-of-flight secondary ion mass spectrometry (ToF-SIMS). In this technique, the samples are bombarded with ions of bismuth, causing polyatomic fragments to spall off. The fragments are collected and analyzed by mass spectrometry to determine the fragment composition. Though quantitative analysis is difficult, differences in the relative abundances of elements can be determined. The results for one of the 8-week samples are shown in Figure 4. ToF-SIMS analysis confirmed conversion of droplets from $MgCl_2$ to Mg-hydroxychloride and Mg-carbonate species from the outer regions inward, and that conversion was more complete in smaller droplets.

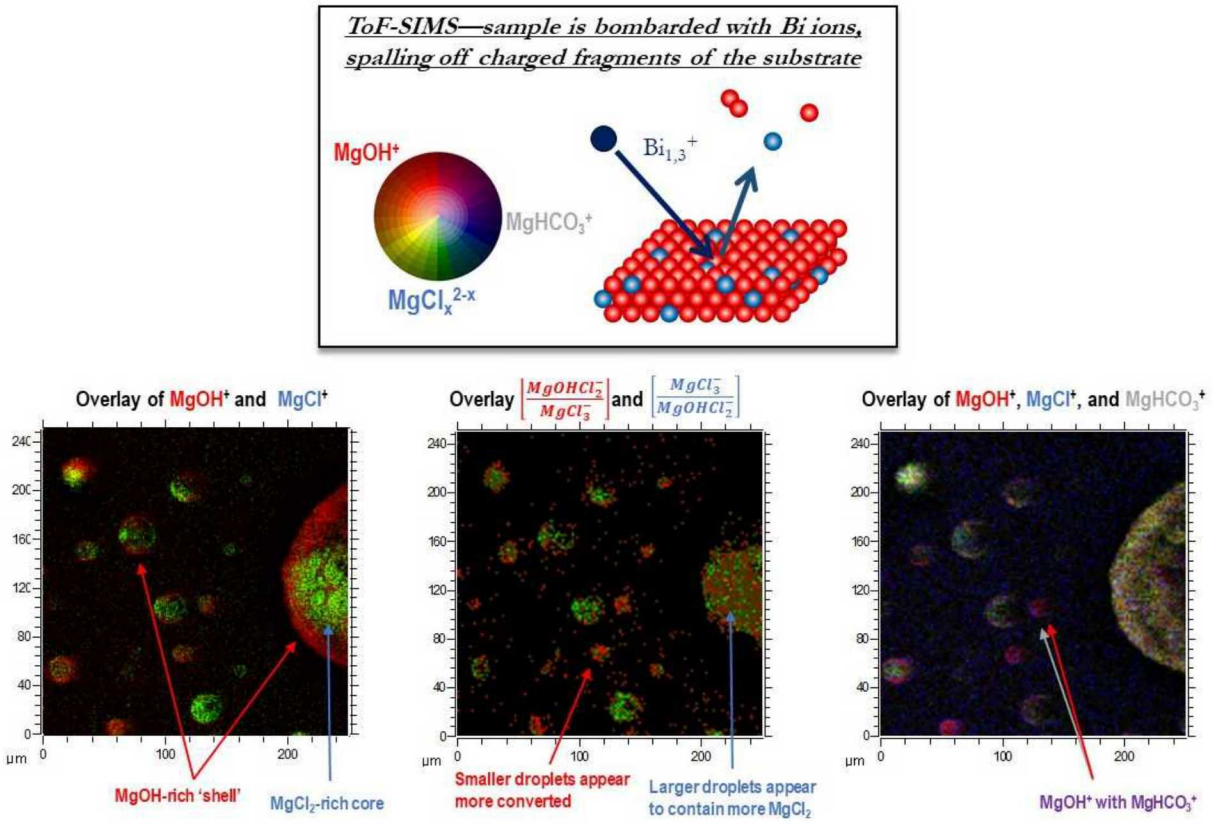

Figure 4. ToF-SIMS analysis confirms that magnesium chloride brine droplets are losing chloride and gaining hydroxyl and carbonate.

One of the 8-week samples was also analyzed by Raman spectroscopy and Fourier-transform infrared (FTIR) spectroscopy, using a microanalysis system capable of analyzing individual droplets on the wafer surface and of mapping across the entire sample. The Raman system used was a Witec Alpha 300 Raman Confocal Microscope. The sample was placed directly under the microscope and data was collected using the 532 nm laser with integration times of 0.25 seconds and 8 co-added scans per spectrum. However, it was not possible to get spectra with a good signal-to-noise from the areas of interest. For the FTIR analysis, a small sample cell was constructed with an IR-transparent KBr window and a desiccant chamber beneath the sample containing Drierite®. This allowed the sample to be analyzed without deliquescing in the room air. For analysis, the sample was placed under a Bruker Hyperion 3000 IR microscope connected to a Bruker Vertex 70V infrared bench. IR data were collected in reflectance mode, using a 15× IR objective. Data were collected at 4 cm^{-1} resolution, with 128 scan co-additions. The resultant Log reflectance spectra were calculated using an aluminum reflectance as the background (512 co-additions). However, the FTIR spectroscopy showed significant differences in the spectra at different locations on the wafer surface (Figure 5), corresponding to regions where different degrees of conversion were observed by SEM/EDS analysis. In regions where low conversion been observed, the hydroxyl stretch band from 3000 cm^{-1} and 3700 cm^{-1} was very broad, and there was a prominent hydroxyl bend band at 1600 cm^{-1}. This pattern matches that of bischofite ($MgCl_2{:}6H_2O$) which is the stable phase that precipitates from magnesium chloride brine upon dryout. In regions where conversion was most prominent, the stretch band was lower intensity and was narrower and sharper, and the hydroxyl bend band was largely missing. These differences indicate changes in the amount and bond structure of water and hydroxyl at the different locations, as would be expected if the magnesium chloride brine had degassed HCl and precipitated the Mg-hydroxychloride hydrate ($2Mg(OH)_2{:}MgCl_2{:}4H_2O$).

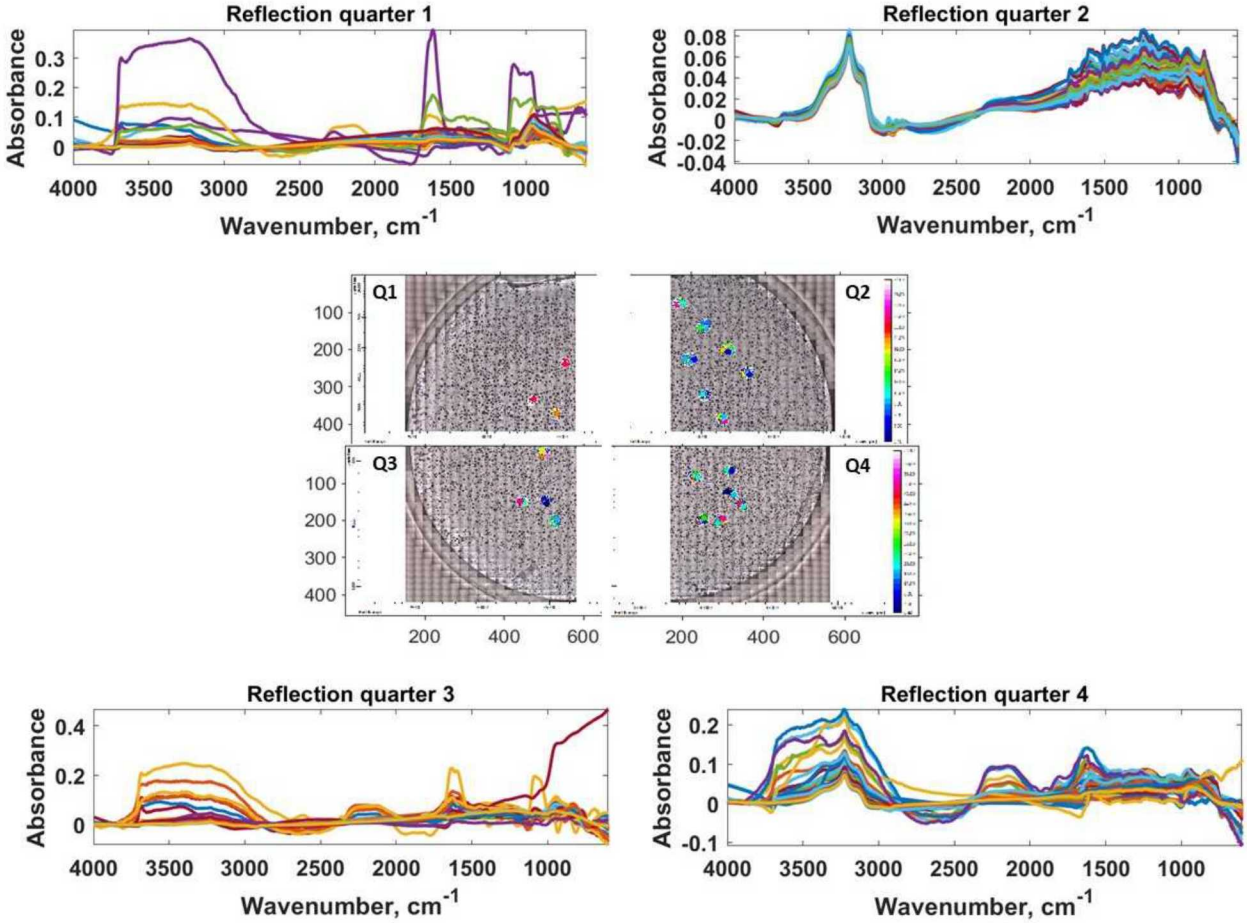

Figure 5. FTIR analysis of a brine droplet sample exposed for 8 weeks at 80°C and 35% RH. FTIR spectra show significant differences in the hydroxyl stretch band at 3000-3700 cm^{-1} and the hydroxyl bend band at 1620 cm^{-1} at different locations on the wafer surface.

Finally, once all non-destructive analyses were completed, each of the samples was leached with a known volume of deionized water to extract the salts on the wafer surface, and the solutions were analyzed by ion chromatography (IC) to determine soluble salt compositions. Anionic analytes were F^-, Cl^-, Br^-, NO_2^-, NO_3^-, SO_4^{2-}, and PO_4^{3-}; cationic analytes were Li^+, Na^+, NH_4^+, K^+, Mg^{2+}, and Ca^{2+}. For detailed analytical procedures, see Bryan and Enos (2016). All analyses were carried out using standards made by dilution of Dionex® pre-mixed multi-element stock solutions. All standards and electrolytes were purchased specifically for this analysis and were within their expiration date.

In addition to samples collected after 2, 4, and 8 weeks, three control samples were kept in a nitrogen-purged dry box over the duration of the experiment. These control samples represent the initial conditions on the samples. Finally, two uncoated wafers were kept in the RH chamber over the 8-week duration of the experiment for use as sample blanks. Results of the chemical analyses for the samples, controls, and blanks, are provided in micrograms per sample in Table 1. Since the deposited brine droplets were magnesium chloride, Mg^{2+} and Cl^- dominated the ions present; however, trace amounts of other ions were also detected. These were generally below the limit of quantitation, but in a few cases, the concentrations were significant—this is not surprising, given the potential for contamination during the preceding non-destructive analyses. The only other ion that was consistently above background was F^-, and trace fluorine was also detected in small droplets in the 8-week samples by Tof-SIMS. It seems

likely that this was derived from the silicon wafer, which may have been processed with HF at some point during manufacture.

Table 1. Measured ion concentrations on magnesium chloride stability experiment (µg/sample).

Exposure time, wks	Na^+	K^+	Mg^{2+}	Ca^{2+}	F^-	Cl^-	NO_3^-	SO_4^{2-}	$MgCl_2$ µg/sample
0	*3.7*	*n.a.*	372	*2.5*	*n.a.*	1030	*1.7*	3.9	1402
0	*4.0*	*n.a.*	493	*1.8*	*n.a.*	1375	*1.5*	4.3	1868
0	*3.8*	*n.a.*	478	*2.2*	*n.a.*	1327	*1.8*	4.1	1805
2	*4.4*	*n.a.*	191	*1.8*	3.4	452	3.0	5.2	643
2	*4.5*	*n.a.*	393	*2.9*	5.0	1030	3.8	4.3	1422
2	*2.5*	*n.a.*	285	*0.4*	4.0	703	3.0	4.3	988
4	*5.8*	*1.8*	261	37.0	6.2	757	2.9	5.7	1018
4	*3.2*	*n.a.*	291	*0.6*	6.4	713	3.3	5.1	1004
4	*4.2*	*1.3*	298	*1.2*	4.8	733	4.5	7.7	1031
8	*n.a.*	*n.a.*	190	*n.a.*	10.5	363	*n.a.*	*n.a.*	552
8	*n.a.*	*n.a.*	234	*n.a.*	8.5	424	*n.a.*	*n.a.*	657
8	*n.a.*	*n.a.*	298	*n.a.*	8.5	465	*n.a.*	*n.a.*	763
Blank	*1.4*	*0.8*	*n.a.*	13.5	*n.a.*	*0.7*	*1.5*	*1.6*	—
Blank	*2.0*	*1.0*	*n.a.*	13.8	*0.1*	3.6	*1.1*	*2.2*	—

The total deposited magnesium chloride on each sample varied considerably. A modified inkjet printer was used to deposit the magnesium chloride brine droplets on the wafers, and while this method provides consistent coatings for other salts, pure magnesium chloride brine tends to clog the print head, resulting in varying sample loads between samples. Moreover, some deposited salts were probably lost during the non-destructive testing that preceded the chemical analyses. However, for this study, the total quantity magnesium chloride present in not important; rather, changes in the relative amounts of Mg and Cl, which would indicate degassing of the chloride as HCl, are being evaluated. Measured ion concentrations are shown in microequivalents (µEq) per sample in Table 2. This unit allows direct comparison of the relative concentrations of magnesium and chloride, which in the original brine would have been present in the same number of equivalents; any discrepancy indicates loss of chloride. In the control samples, the number of equivalents of Mg and Cl are very similar, although Cl equivalents are consistently slightly lower than Mg. However, for the exposed samples, there is a clear deficiency in chloride, and this number is greatest in the 8-week exposures. The estimated amount of chloride lost as a function of exposure time is shown in Figure 6. There is a good deal of scatter, consistent with the wide variation in the degree of reaction that was observed in the SEM/EDS analysis. However, there is a clear trend of increasing chloride loss with exposure time, with samples exposed for 8 weeks losing ~40% of their chloride. Complete conversion to $2Mg(OH)_2{:}MgCl_2{:}4H_2O$, the 2-1-4 magnesium hydroxychloride identified by XRD, would result in 66% chloride lost.

The overall reaction that is occurring can be written as:

$$3Mg^{2+}_{(aq)} + 6Cl^{-}_{(aq)} + 8H_2O \rightarrow 2Mg(OH)_2{:}MgCl_2{:}4H_2O_{(s)} + 4HCl_{(g)} \quad \text{(Eq. 1)}$$

As discussed in Bryan and Schindelholz (2018), this phase has been observed as a surface precipitate in corrosion experiments performed under similar environmental conditions, indicating that it is less deliquescent than bischofite, and hence, that the brine would eventually dry out if this reaction goes to completion. Although these test conditions (80ºC and 35% RH) are not relevant to field conditions for SNF dry storage canisters, they have been used as accelerated testing conditions by SNL and others, and correct interpretation of the experimental results requires understanding that brine dryout will eventually occur. This work was presented at PATRAM 2019 (Bryan *et al.*, 2019).

Table 2. Measured ion concentrations in magnesium chloride stability experiment (µg/sample).

Exp time, weeks	Na^+	K^+	Mg^{2+}	Ca^{2+}	F^-	Cl^-	NO_3^-	SO_4^{2-}
0	*0.16*	*n.a.*	30.6	*0.12*	*n.a.*	29.1	*0.08*	0.16
0	*0.17*	*n.a.*	40.6	*0.09*	*n.a.*	38.8	*0.07*	0.18
0	*0.16*	*n.a.*	39.3	*0.11*	*n.a.*	37.4	*0.09*	0.17
2	*0.19*	*n.a.*	15.7	*0.09*	0.18	12.8	0.15	0.22
2	*0.19*	*n.a.*	32.3	*0.14*	0.26	29.0	0.19	0.18
2	*0.11*	*n.a.*	23.4	*0.02*	0.21	19.8	0.14	0.18
4	0.25	*0.05*	21.5	1.84	0.33	21.3	0.14	0.24
4	*0.14*	*n.a.*	24.0	*0.03*	0.34	20.1	0.16	0.21
4	*0.18*	*0.03*	24.5	*0.06*	0.25	20.7	0.22	0.32
8	*n.a.*	*n.a.*	15.6	*n.a.*	0.55	10.2	*n.a.*	*n.a.*
8	*n.a.*	*n.a.*	19.2	*n.a.*	0.45	12.0	*n.a.*	*n.a.*
8	*n.a.*	*n.a.*	24.5	*n.a.*	0.45	13.1	*n.a.*	*n.a.*
Blank	*0.06*	*0.02*	*n.a.*	0.68	*n.a.*	*0.02*	*0.07*	*0.07*
Blank	*0.09*	*0.03*	*0.03*	0.69	*n.a.*	*0.10*	*0.05*	*0.09*

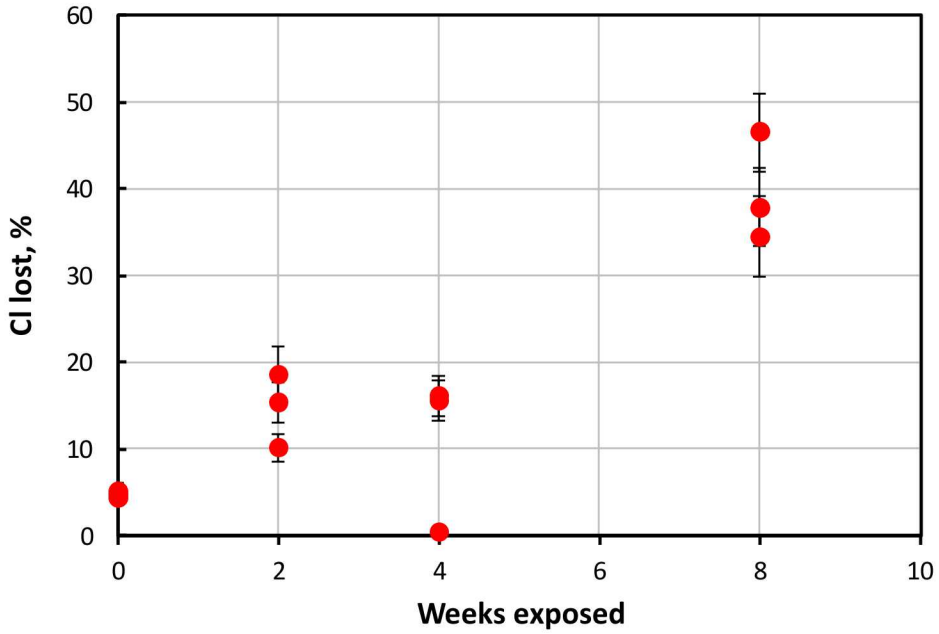

Figure 6. Estimated amount of chloride lost from the exposed samples, over the 8 week exposure period. The 8-week samples indicate loss of about 40% of the chloride that had been initially present.

It is a topic of current research to develop an understanding of magnesium chloride brine stability over the range of conditions that can occur on a SNF dry storage canister surface. The magnesium hydroxychloride phase that precipitates from a Mg-rich brine is a function of brine chemistry and temperature; the 2-1-4 phase has now been observed in several experiments at 80°C and 35% RH. As discussed in the following section, several magnesium hydroxychlorides exist, and different phases will form under different environmental conditions. Moreover, precipitation of magnesium hydroxychlorides has been observed in several corrosion experiments as well, due to hydroxide production in the cathode via the oxygen reduction reaction (ORR). Future experimental work will continue to evaluate brine

stability under relevant conditions, performing longer-term experiments in an effort to obtain a greater degree of reaction at only moderately elevated temperatures. This will allow better identification of the secondary phases that form. Also, some experiments will be carried out at RH values below the deliquescence RH, to determine if Mg-brine degassing and conversion to carbonates of hydroxy-chlorides can occur prior to formation of a bulk brine phase.

The reactions observed in these laboratory experiments are only a subset of the possible reactions that can occur in field conditions, where reactions with other atmospheric gases (H_2S and NO_x) can drive chloride degassing potentially much more efficiently than CO_2 reactions. We are beginning the evaluate these reactions thermodynamically, and in the coming year, will begin to assess their effects experimentally.

2.2 Magnesium Hydroxychloride Phase Stability

As observed in several experiments, including the brine degassing experiments on inert substrate discussed in Section 2.1; rotating disk electrode (RDE) experiments to measure cathodic kinetics discussed in Section 3; and the big mockup plate corrosion tests discussed in Section 6, magnesium chloride brines evolve to form magnesium hydroxychlorides phases in environments relevant to the surface of SNF dry storage canisters. The formation of magnesium hydroxychloride phases has significant implications on the likelihood and timing of SCC on SNF storage canisters, as the deliquescence RH of magnesium hydroxychlorides is higher than that of bischofite, and in some cases, higher than halite. Therefore, it becomes extremely important to assess the stability of magnesium hydroxychlorides phases under the conditions that could occur on the surface of the SNF storage canisters. Unfortunately, thermodynamic data for these phases are generally inadequate at room temperature and incomplete at high temperatures.

In order to develop a thermodynamic model of the brine evolution that accurately predicts the formation of magnesium hydroxychlorides over the temperature range from 25 ºC to 150 ºC, sufficient and accurate thermodynamic data are required. With the necessary thermodynamic data, we can create a suite of temperature-dependent LogK values grids for the phase dissociation reactions for incorporation into a thermodynamic database and use to evaluate the stability and evolution of Mg-rich sea-salt deliquescent brines. Our strategy to develop a thermodynamic library for magnesium hydroxychloride phases was a stepwise approach as follows:

- Compile known literature thermodynamic data for Mg-chloride, Mg-hydroxide, and Mg-hydroxychloride mineral phases.
- Calculate heat capacities (C_p) and Haas-Fisher heat capacity coefficients (*a, b, c, d, e*) using the ion-based group contribution method for inorganic salts, as described by Mostafa *et al.* (1996).
- Assume the thermodynamic values Gibbs Free Energy (ΔG_f^o) and entropy (S^o) (and *via* calculation, enthalpy, ΔH_f^o) for Mg-salts can be estimated as the stoichiometric sum of contributions from three components, MgO, $MgCl_2$, and H_2O. Use Excel Solver to solve for the contributions from each component by minimizing the summed squared difference between the literature values and the calculated values.
- Stoichiometrically combine best-fit component values for MgO, $MgCl_2$, and H_2O to calculate thermodynamic data for Mg-hydroxychloride phases that lack measured thermodynamic data, and use the Mostafa *et al.* (1996) method to calculate C_p data.
- Use the CHNOSZ package for R (Dick, 2019), to calculate LogK grids [0ºC - 25ºC - 60ºC - 100ºC - 150ºC] from ΔG_f^o, ΔH_f^o, S^o, C_p and Haas-Fisher heat capacity coefficients for the different Mg-chloride, Mg-hydroxide, and Mg-hydroxychloride phases. This method provides a starting point calculation of the LogK values.

- Geochemically model the Mg-OH-Cl system using The Geochemist's Workbench (GWB) (Bethke, 2008) and EQ3/6 (Wolery, 2010), comparing calculated phase solubilities and stability ranges with available experimental data Pannach *et al.* (2017).
- Using the values estimated by CHNOSZ as a starting point, fit the experimental data of Pannach *et al.* (2017) to further refine the LogK values.

2.2.1 Calculation of Thermodynamic Data for Mg-Bearing Mineral Phases

2.2.1.1 Calculation of C_P of Magnesium Mineral Phases

Heat capacities (C_p) for the various magnesium phases were determined using the method by Mostafa et al. (1996). The heat capacities are estimated by the following equation:

$$C_p = a + bT + \frac{c}{T^2} + dT^2 \qquad \text{(Eq. 2)}$$

in which coefficients a, b, c, and d are estimated by group contributions of ion-based groups with a multiple linear regression (Mostafa *et al.*, 1996). This method of using group contribution to predict the C_p-correlation coefficients has been verified for solid inorganic salts (Mostafa et al., 1996; Xiong et al., 2010). Therefore, we believe this is an appropriate method to estimate the C_p for Mg-bearing salts.

In order to determine C_p at any given temperature, the a, b, c, and d values must be derived. These coefficients are derived from the values in Table 3 and an expanded form of Equation 2 to account for the ion group contributions. As derived from Knacke and Kubaschewski (1990), Equation 3 is a reduced fundamental form to best fit known experimental values used to calculate C_p.

$$C_p = \sum_J n_j \Delta_{aj} + (\sum_J n_j \Delta_{bj}\ x\ 10^{-3})T + (\sum_J n_j \Delta_{cj}\ x\ 10^{6})\frac{1}{T^2} + (\sum_J n_j \Delta_{dj}\ x\ 10^{-6}) \qquad \text{(Eq. 3)}$$

Where n_j is the number of groups of the jth type, T is temperature in Kelvin (K), and k (k = a, b, c, or d) is the kth coefficient for the jth group. The values of Δ_{aj}, Δ_{bj}, Δ_{cj} , and Δ_{dj} from each elemental or group component used to calculate the C_p values for various Mg-bearing salts are summarized in Table 3.

Table 3. Solid inorganic groups used to calculate C_P for Mg-bearing salts with their associated Δ_{aj}, Δ_{bj}, Δ_{cj} , and Δ_{dj} term values from Mostafa *et al.* (1996)

Group	Δ_{aj}	Δ_{bj}	Δ_{cj}	Δ_{dj}
Mg^{2+}	14.639	-0.637	-0.074	-0.609
Cl^-	26.609	10.376	-0.251	0.657
H_2O	15.458	66.593	0.470	-40.518
OH^-	28.917	30.730	-0.628	3.527
O^{2-}	28.152	12.043	-0.747	-4.023

Using the solid inorganic groups and Equation 3, we estimated the C_p of a suite of Mg-bearing salts (Table 4); for the few salts with available literature values, the calculated and literature values were compared. Literature C_p values were only available for brucite, bischofite, and the 5-1-8 magnesium hydroxychloride phase. Our calculated values for brucite and the 5-1-8 magnesium hydroxychloride were consistent with literature values, however our value for bischofite was roughly 8% higher than the reported literature value from Wagman *et al.* (1982). Additionally, the literature value for the 5-1-8 phase determined by Xiong *et al.* (2010) was calculated by the same method as the one described here.

Table 4. Summary of calculated heat capacity coefficients, calculated and literature standard state (298.15 K) C_p values for several magnesium chloride, hydroxide, and hydroxychloride species.

Phase	Short Name	*a* (J/g*mol*K)	*b* (J/mol*K^2)	*c* (J*K/mol)	*d* (J/K^2*mol)	*e* (J/K^2*mol)	C_P (J/g*mol*K) Calculated	C_P (J/g*mol*K), Literature	Reference
$Mg(OH)_2$	Brucite	72.473	0.060823	-1.33×10^{6}	-	5.91×10^{-6}	76.17	77.03	(Wagman *et al.*, 1982)
$MgCl_2{:}6H_2O$	Bischofite	160.605	0.419673	-2.24×10^{6}	-	-2.42×10^{-4}	289.43	315.06	(Wagman *et al.*, 1982)
$MgCl_2{:}4H_2O$	-	-	-	-	-	-	215.43	*No Data*	-
$MgCl_2{:}2H_2O$	-	-	-	-	-	-	141.43	*No Data*	-
$MgCl_2{:}H_2O$	-	-	-	-	-	-	104.44	*No Data*	-
MgOHCl	-	-	-	-	-	-	71.80	*No Data*	-
$Mg_2(OH)_3Cl{:}4H_2O$	3-1-8	204.47	0.367664	-4.03×10^{5}	-	-1.53×10^{-4}	295.97	*No Data*	-
$Mg_3(OH)_5Cl{:}4H_2O$	5-1-8	276.943	0.428487	-1.73×10^{6}	-	-1.47×10^{-4}	372.14	372	(Xiong *et al.*, 2010)
$2Mg(OH)_2\text{-}MgCl_2{:}2H_2O$	2-1-2	243.719	0.274947	-2.30×10^{6}	-	-6.85×10^{-5}	293.77	*No Data*	-
$2Mg(OH)_2\text{-}MgCl_2{:}4H_2O$	2-1-4	274.635	0.408133	-1.36×10^{6}	-	-1.50×10^{-4}	367.77	*No Data*	-
$9Mg(OH)_2\text{-}MgCl_2{:}4H_2O$	9-1-4	781.946	0.833894	-1.07×10^{-7}	-	1.08×10^{-4}	900.96	*No Data*	-

Because of the paucity of literature values, an additional validation of the Mostafa *et al.* (1996) method was performed. Using our calculated heat capacity coefficients, C_p values for brucite were calculated over a range of temperatures and compared to experimentally-determined values reported by Robie and Hemingway (1995). The comparison is shown in Figure 7. Also shown is a best fit generated for the experimental data below 700ºC using the Haas-Fisher equation:

Haas Fischer Equation: $$C_p = a + bT + \frac{c}{T^2} + \frac{d}{\sqrt{T}} + eT^2 \quad \text{(Eq. 4)}$$

The Haas-Fisher equation is a frequently used approach for fitting experimental heat capacity data, and very similar to Mostafa *et al.* (1996) C_p equation in Equation 2, apart from the added *d* term. As seen in Figure 7, within the temperature range of interest, we see good agreement between the C_p values calculated by the Mostafa and the Haas-Fisher equations with the experimental data over the temperature range of interest (given the simplicity of the equations, it is commonly necessary to restrict the fit to a limited range of temperature data) . Based on this comparison, we are confident that the estimated values for C_p for other Mg-bearing mineral phases are reasonably accurate.

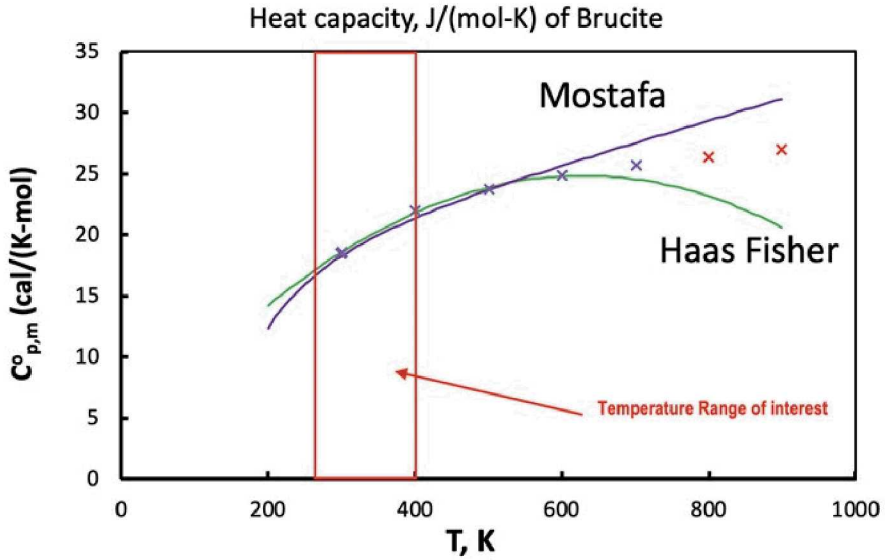

Figure 7. Verification of heat capacity calculations with available experimental data. Heat capacities calculated from the Mostafa *et al.* (1996) method (purple line) and calculated data fit using the Haas Fisher Equation (green line) both fit the experimental data from Robie and Hemingway (1995) well.

2.2.1.2 *Estimation of Thermodynamic Parameters ΔG_f^o, ΔH_f^o, and S^o for Mg-bearing Mineral Phases*

In order to estimate the ΔG_f^o, ΔH_f^o, and S^o, we first compiled literature values for Mg-bearing mineral phases. The reported literature values are summarized in Table 5. Some of the Mg-bearing phases, such as brucite, have sufficient data. However, the scatter in the data is fairly substantial. For brucite, the range for ΔG_f^o is -831.44 kJ/mol to -835.32 kJ/mol; for S^o is 50.6 J/mol to 64.4 J/mol; and for ΔH_f^o is -923 kJ/mol to -927.51 kJ/mol. Additionally, there are either limited or no thermodynamic data available for the phases relevant to SNF canister surface conditions or to conditions used in the corrosion experiments, such as the 2-1-4 magnesium hydroxychloride phase that we have routinely seen in experiments. Because of the lack of reliable thermodynamic data, we chose to estimate ΔG_f^o, ΔH_f^o, and S^o values using a sum of group contributions method (Hazen, 1985; Chermak and Rimstidt, 1989).

Table 5. Summary of available thermodynamic data in the literature (ΔG_f^o, S^o and ΔH_f^o) for several Mg-bearing mineral phases.

Phase	Short Name	ΔG_f^o (kJ/mol)	Reference	S^o (J/mol*K)	Reference	ΔH_f^o (kJ/mol)	Reference
$Mg(OH)_2$	Brucite	-832.3±1.1	(Giauque and Archibald, 1937; Xiong et al., 2010)	63.14	(Giauque and Archibald, 1937; Konigsberger et al., 1999; Altmaier et al., 2003; Xiong et al., 2010)	-923.3±1.1	(Xiong *et al.*, 2010)
		-831.44±1.1	(Harvie et al., 1984; Altmaier et al., 2003)	63.18	(Wagman et al., 1982; Konigsberger et al., 1999; Xiong et al., 2010)	-924.35±0.3	(Xiong *et al.*, 2010)
		-833.51	(Wagman et al., 1982; Konigsberger et al., 1999)	59.43	(Zhou et al., 2015; Liu et al., 2017)	-924.54	(Wagman et al., 1982; Ba and Guan, 2009; Xiong et al., 2010)
		-831.992	(Zhou et al., 2015; Liu et al., 2017)	50.6	(Brown et al., 1996; Konigsberger et al., 1999; Altmaier et al., 2003)	-924.142	(Zhou et al., 2015; Liu et al., 2017)
		-835.32	(Altmaier *et al.*, 2003)	63.2	(Robie, 1995)	-926.7	(Brown et al., 1996; Konigsberger et al., 1999; Altmaier et al., 2003)
		-831.9	(Brown et al., 1996; Konigsberger et al., 1999; Altmaier et al., 2003)	64.4	(Konigsberger *et al.*, 1999)	-927.51	(Konigsberger *et al.*, 1999)
		-833.5	(Robie, 1995; Konigsberger et al., 1999)	63	(Lothenbach et al., 2008; Liu et al., 2017)	-924.5	(Robie, 1995; Konigsberger et al., 1999)
		-832.1	(Altmaier *et al.*, 2003)	-	-	-925.5	(Konigsberger *et al.*, 1999)
		-833.58	(Ba and Guan, 2009)	-	-	-923	(Lothenbach et al., 2008; Liu et al., 2017)
		-832.23	(Lothenbach *et al.*, 2008)	-	-		
$MgCl_2:6H_2O$	Bischofite	-2114.8	(Harvie et al., 1984; Zhou et al., 2015; Liu et al., 2017)	339.73	(Zhou et al., 2015; Liu et al., 2017)	-2507.43	(Zhou et al., 2015; Liu et al., 2017)
		-2115.196	(Zhou et al., 2015; Liu et al., 2017)	366.1	(Wagman et al., 1982; Phutela et al., 1987)	-2499.02	(Wagman et al., 1982; Phutela et al., 1987)
		-2114.64	(Wagman et al., 1982; Phutela et al., 1987)	-	-	-	-
$MgCl_2:4H_2O$	-	-1623.29	(Wagman *et al.*, 1982)	264	(Wagman *et al.*, 1982)	-1898.99	(Wagman *et al.*, 1982)
$MgCl_2:2H_2O$	-	-1118	(Wagman *et al.*, 1982)	179.9	(Wagman *et al.*, 1982)	-1279.72	(Wagman *et al.*, 1982)
$MgCl_2:H_2O$	-	-861.74	(Wagman *et al.*, 1982)	137.2	(Wagman *et al.*, 1982)	-966.63	(Wagman *et al.*, 1982)
MgOHCl	-	-731.7	(Wagman *et al.*, 1982)	83.7	(Wagman *et al.*, 1982)	-799.6	(Wagman *et al.*, 1982)

Phase	Short Name	ΔG_f^o (kJ/mol)	Reference	S^o (J/mol*K)	Reference	ΔH_f^o (kJ/mol)	Reference
$Mg_2(OH)_3Cl{:}4H_2O$	**3-1-8**	-2557.1	(Ba and Guan, 2009; Liu et al., 2017)	292.74	(Altmaier et al., 2003; Zhou et al., 2015; Liu et al., 2017)	-2944.05	(Ba and Guan, 2009; Liu et al., 2017)
		-2552.33	(Harvie *et al.*, 1984)	-	-	-2947.2	(Altmaier et al., 2003; Zhou et al., 2015; Liu et al., 2017)
		-2552.08	(Altmaier et al., 2003; Liu et al., 2017)	-	-	-	-
		-2553.37	(Altmaier et al., 2003; Liu et al., 2017)	-	-	-	-
$Mg_3(OH)_5Cl{:}4H_2O$	**5-1-8**	-3388	(Ba and Guan, 2009; Liu et al., 2017)	394 ± 20	(Xiong et al., 2010; Liu et al., 2017)	-3863.55	(Ba and Guan, 2009; Liu et al., 2017)
		-3385± 2	(Xiong et al., 2010; Liu et al., 2017)	-	-	-3898 ± 6	(Xiong et al., 2010; Liu et al., 2017)
$2Mg(OH)_2$-$MgCl_2{:}2H_2O$	**2-1-2**	*No Data*	-	*No Data*	-	*No Data*	-
$2Mg(OH)_2$-$MgCl_2{:}4H_2O$	**2-1-4**	*No Data*	-	*No Data*	-	*No Data*	-
$9Mg(OH)_2$-$MgCl_2{:}4H_2O$	**9-1-4**	*No Data*	-	*No Data*	-	*No Data*	-

Thermodynamic values ΔG_f^o and S^o were calculated using group contributions. To keep the calculated thermodynamic values self-consistent, ΔH_f^o was calculated from ΔG_f^o and S^o using the Gibbs Free Energy equation:

$$\Delta G_f^o = \Delta H_f^o - T\Delta S^o \quad \text{(Eq. 5)}$$

where T is the temperature in Kelvin and S^o is the standard entropy of the elements. For the calculation of ΔG_f^o and S^o, we considered each Mg-bearing mineral phase as consisting of components, combined stoichiometrically. This method has been used previously to estimate the thermodynamics in silicate minerals (Hazen, 1985; Chermak and Rimstidt, 1989). In our system, the components were considered as:

$$xMgO - yMgCl_2 - zH_2O \quad \text{(Eq. 6)}$$

Where x, y, and z are the stoichiometric equivalents of that component. A summary of stoichiometric equivalents of each component is shown in Table 6 for the phases in interest.

Table 6. Unit equivalents for each magnesium hydroxychloride phase.

Phase	Short Name	MgO	$MgCl_2$	H_2O
$Mg(OH)_2$	Brucite	1	0	1
$MgCl_2{:}6H_2O$	Bischofite	0	1	6
$Mg_2(OH)_3Cl{:}4H_2O$	3-1-8	1.5	0.5	5.5
$Mg_3(OH)_5Cl{:}4H_2O$	5-1-8	2.5	0.5	6.5
$2Mg(OH)_2\text{-}MgCl_2{:}2H_2O$	2-1-2	2	1	4
$2Mg(OH)_2\text{-}MgCl_2{:}4H_2O$	2-1-4	2	1	6
$9Mg(OH)_2\text{-}MgCl_2{:}4H_2O$	9-1-4	9	1	14

To estimate the ΔG_f^o and S^o values for the MgO, $MgCl_2$, and H_2O components, Excel Solver was used to adjust these two values to minimize the summed squared difference between literature-reported ΔG_f^o and S^o values for a suite of Mg-bearing mineral phases and values calculated using the stoichiometrically combined components. The resulting ΔG_f^o and S^o contributions for each component are shown in Table 7. Also shown are the values for the equivalent free phases. As with the silicate system, the free thermodynamic properties of the free phases differ significantly from those of the individual components when present in a hydrated magnesium chloride, hydroxide or hydroxy-chloride salt.

Table 7. Calculated ΔG_f^o and S^o compared to literature values for basic units MgO, $MgCl_2$, and H_2O. These phases were used on the group contributions to estimate thermodynamic data for other Mg-bearing mineral phases.

Phase	ΔG_f^o (kJ/mol), Calculated	ΔG_f^o (kJ/mol), Literature	S^o (J/mol), Calculated	S^o (J/mol), Literature
MgO	-582.79	-597.53 (Harvie *et al.*, 1984)	21.72	26.94 (Wagman *et al.*, 1982)
$MgCl_2$	-619.61	-591.79 (Robie, 1995; Xiong et al., 2010)	96.30	89.62 (Robie, 1995; Xiong et al., 2010)
H_2O	-249.23	-237.15 (Xiong *et al.*, 2010)	42.36	46 ± 3 (Xiong *et al.*, 2010)

Using the calculated ΔG_f^o and S^o values for the individual components and the stoichiometric composition, we calculated ΔG_f^o and S^o values for a suite of Mg-bearing mineral species. Then, ΔH_f^o was calculated using Equation 5. The calculated values for ΔG_f^o, ΔH_f^o, and S^o are listed in Table 8. For some of these phases, literature data exist, and we were able to compare the calculated values with those reported in the literature.

Table 8. Summary of calculated ΔG_f^o, ΔH_f^o, and S^o values for several magnesium hydroxychloride species.

Phase	Short Name	ΔG_f^o (kJ/mol)	ΔH_f^o (kJ/mol)	S^o (J/mol*K)
$Mg(OH)_2$	Brucite	-832.02	-922.78	64.08
$MgCl_2{:}6H_2O$	Bischofite	-2114.97	-2504.00	350.45
$MgCl_2{:}4H_2O$	-	-1616.52	-1891.72	265.74
$MgCl_2{:}2H_2O$	-	-1118.07	-1279.44	181.02
$MgCl_2{:}H_2O$	-	-868.84	-973.29	138.66
MgOHCl	-	-725.82	-794.97	80.19
$Mg_2(OH)_3Cl{:}4H_2O$	3-1-8	-2554.74	-2942.31	313.70
$Mg_3(OH)_5Cl{:}4H_2O$	5-1-8	-3386.75	-3865.09	377.77
$2Mg(OH)_2\text{-}MgCl_2{:}2H_2O$	2-1-2	-2782.10	-3125.00	309.17
$2Mg(OH)_2\text{-}MgCl_2{:}4H_2O$	2-1-4	-3280.55	-3737.28	393.89
$9Mg(OH)_2\text{-}MgCl_2{:}4H_2O$	9-1-4	-9104.67	-9570.84	842.43

Overall, the calculated ΔG_f^o, ΔH_f^o, and S^o values were in good agreement to the literature reported values. The plots shown in Figure 8 present calculated values versus literature values. Note that there are more data points than there are phases, because the literature is inconsistent in the stoichiometries for similar phases; some of the phases in the literature had doubled stoichiometries. For both ΔG_f^o and ΔH_f^o, the R^2 value of a linear fit line is nearly unity, and the R^2 for the linear fit of S^o is ~0.97, which indicates a strong correlation as well. While the component addition method did result good fits with measured data, it is important to recognize calculation of LogK values depends not upon the absolute magnitude of these phases, but upon the difference between these values and the summed values of aqueous species on the other side of the dissolution reaction. Small changes in ΔG_f^o and ΔH_f^o can result in substantial deviations in the solubility of a given phase.

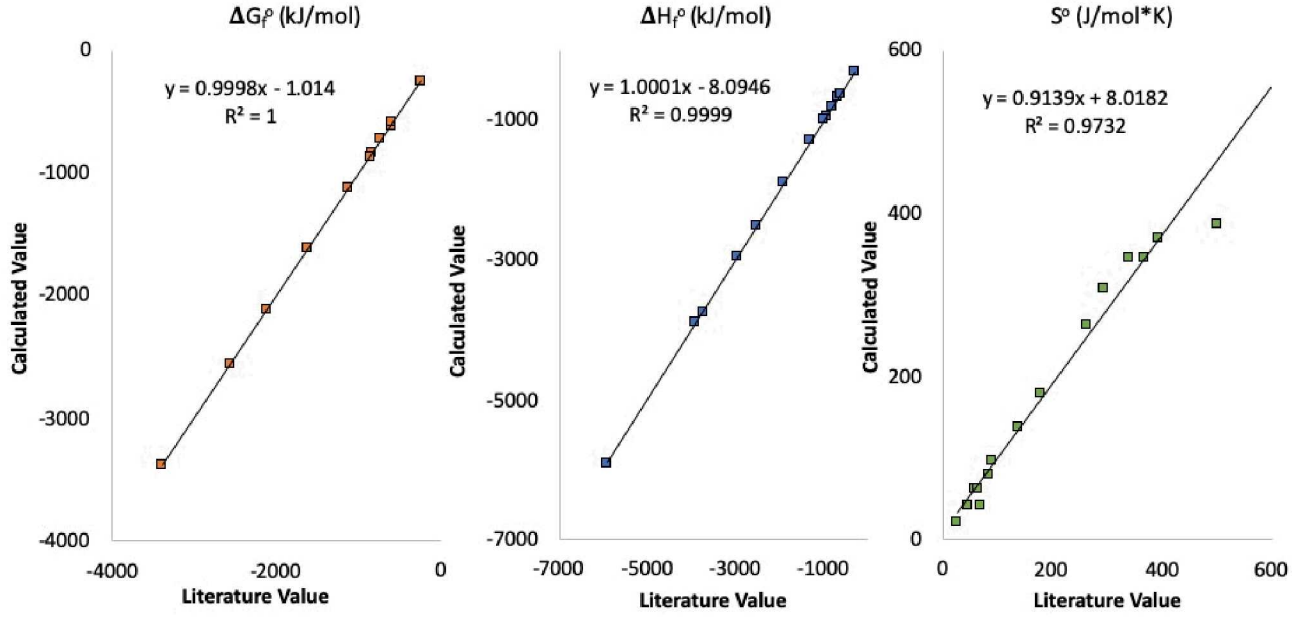

Figure 8. Comparison of the calculated versus literature values for ΔG_f^o, ΔH_f^o, and S^o

2.2.1.3 Calculation of LogK values for a temperature grid [0-25-60-100-150ºC] using CHNOSZ

For geochemical modeling in GWB (Bethke, 2008) and EQ3/6 (Wolery, 2010), grids of LogK values for the mineral dissolution reactions at different temperatures are required. Using our calculated C_p, heat capacity coefficients, ΔG_f^o, ΔH_f^o, and S^o, we can generate a LogK grid for the Mg-bearing mineral phases at temperatures [0-25-60-100-150]. This was accomplished with the geochemical modeling program CHNOSZ (Dick, 2019). The LogK grids calculated for the dissolution reactions of the Mg-bearing mineral species are shown in Table 9. The species and LogK values were added to the thermodynamic databases in GWB and EQ3/6 for geochemical modeling of Mg brine stabilities at elevated temperatures.

Table 9. Calculated LogK grid [0-25-60-100-150ºC] for the dissolution reactions of selected Mg-salt phases

Reaction	Short Name	0 ºC	25 ºC	60 ºC	100 ºC	150 ºC
$Mg(OH)_2 + 2H^+ \leftrightarrow Mg^{++} + 2\ H_2O$	Brucite	18.7256	16.8763	14.7804	12.9061	11.0969
$MgCl_2{:}6H_2O \leftrightarrow Mg^{++} + 2Cl^- + 6\ H_2O$	Bischofite*	4.5811	4.3570	4.0253	3.6643	3.2042
$Mg_2(OH)_3Cl{:}4H_2O + 3\ H^+ \leftrightarrow 2\ Mg^{++} + Cl^- + 7\ H_2O$	3-1-8	27.8999	25.3669	22.4905	19.9275	17.4543
$Mg_3(OH)_5Cl{:}4H_2O + 5\ H^+ \leftrightarrow 3\ Mg^{++} + Cl^- + 9\ H_2O$	5-1-8	46.6257	42.2434	37.270	32.8336	28.5463
$Mg_3(OH)_4Cl_2{:}2H_2O + 4\ H^+ \leftrightarrow 3\ Mg^{++} + 2\ Cl^- + 6\ H_2O$	2-1-2	51.6354	46.5187	40.5524	35.0495	29.5253
$Mg_3(OH)_4Cl_2{:}4H_2O + 4\ H^+ \leftrightarrow 3\ Mg^{++} + 2\ Cl^- + 8\ H_2O$	2-1-4	46.7816	42.2976	37.1018	32.3494	27.6207
$Mg_{10}(OH)18Cl_2{:}4H_2O + 18\ H^+ \leftrightarrow 10\ Mg^{++} + 2\ Cl^- + 22\ H_2O$	9-1-4	177.8625	160.4330	140.5648	122.6914	105.918

* LogK grid for bischofite remained unchanged from data0.ymp, original source (Pabalan and Pitzer, 1987).

There are inherent uncertainties in the accuracy of the values generated in this method. These values were intended to be used as an estimate, with further refinement based on fitting of experimental solubility data.

2.2.2 Thermodynamic Modeling of Magnesium Hydroxychloride Phases

In order to refine and validate the thermodynamic data provided above, we updated the thermodynamic databases in GWB and EQ3/6 and compared predicted Mg-mineral phase boundaries and solubilities with measured data over a range of temperatures and magnesium chloride brine concentrations. Experimental datasets for these systems (especially at elevated temperatures) are sparse, however, there are a few useful datasets to compare against (Einaga, 1981; Altmaier et al., 2003; Pannach et al., 2017). One recent dataset from Pannach *et al.* (2017), was especially useful because it provided experimental data over a large range of temperatures and brine concentrations (Figure 9); note that Figure 9 was modified from its original published form to highlight the stable regions for each Mg-hydroxide phase. As seen in Figure 9, the dominant Mg-hydroxide phase, and its solubility, is dependent the concentration of the $MgCl_2$ solution and the temperature. This solubility diagram agrees with our previous work (Bryan and Schindelholz, 2018), and current experimental data and observations from studies evaluating the stability of Mg-brines both before and after corrosion. At ambient temperatures, we have observed precipitation of the 3-1-8 phase, while the condition at which we have observed the 2-1-4 magnesium hydroxychloride phase (80ºC and 35% RH) falls within the stable region in Figure 9 for that phase. The ability to properly model the formation of the Mg hydroxychloride compounds is required to accurately assess the surface environment on the SNF storage canisters and the approximate temperature at which a corrosive brine could exist on the metal surface.

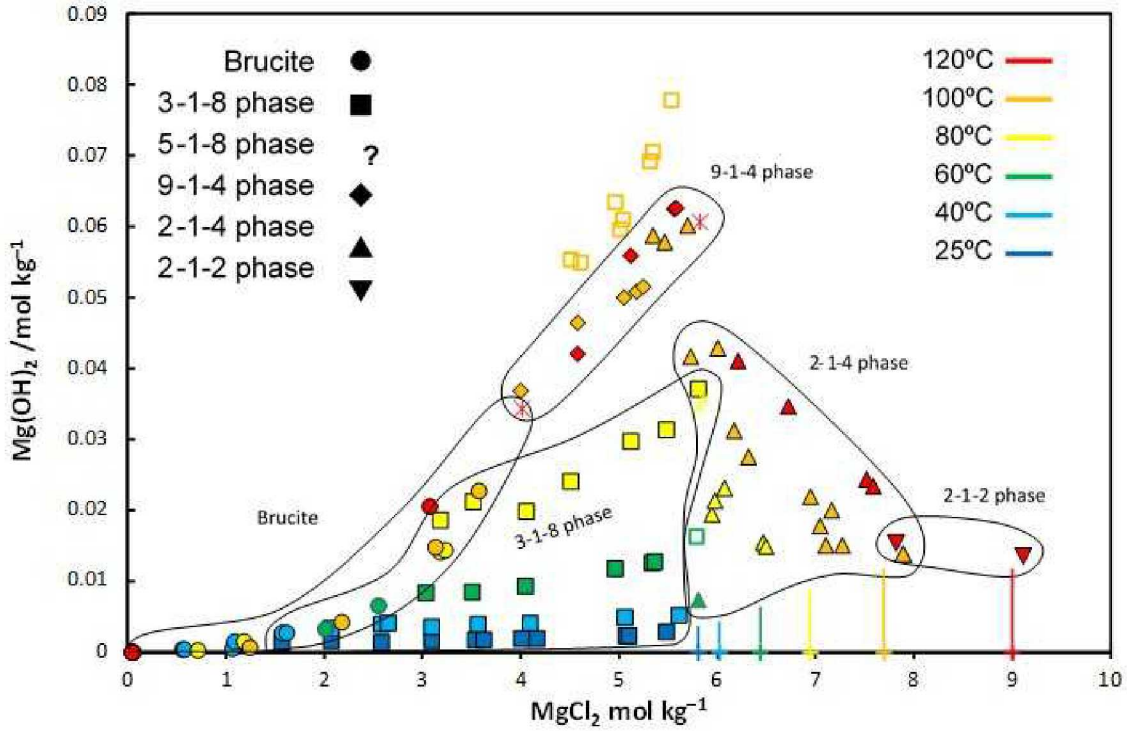

Figure 9. Diagram showing the solubility of various Mg-bear mineral species in the Mg-OH-Cl system from 25 ºC to 120 ºC, adapted from (Pannach *et al.*, 2017). The regions of stability for each phase are outlined, showing the dependence on temperature and $MgCl_2$ concentration.

Using the initial calculated LogK values, we simulated the Pannach *et al. (*2017) data using the Phase2 application in GWB. This was accomplished by performing a 2-D titration simulation at set temperature points [25-40-60-80-100-120ºC], in which $MgCl_2$ in the form of chloromagnesite ($MgCl_2$) was titrated in along the x-axis, and brucite ($Mg(OH)_2$) was titrated in along the y-axis. The resulting assemblages are plotted along with experimental data in Figure 10. Using our initial values of LogK, we are able to reasonably match the measured solubility data for the system at 25 ºC. There is significant spread in the available experimental data (Robie, 1995; Pannach et al., 2017), and our phase boundaries appear to fall in the middle of the experimental datasets. However, at elevated temperatures, our model no longer accurately reflects either the solubility or the phase boundaries, and this discrepancy is accentuated with increasing temperature. Specifically, the modeled solubility diagrams using our initial LogK values consistently underestimated the solubility of the system and failed to produce stable regions for the 2-1-2, 2-1-4, or the 9-1-4 magnesium hydroxychloride phases.

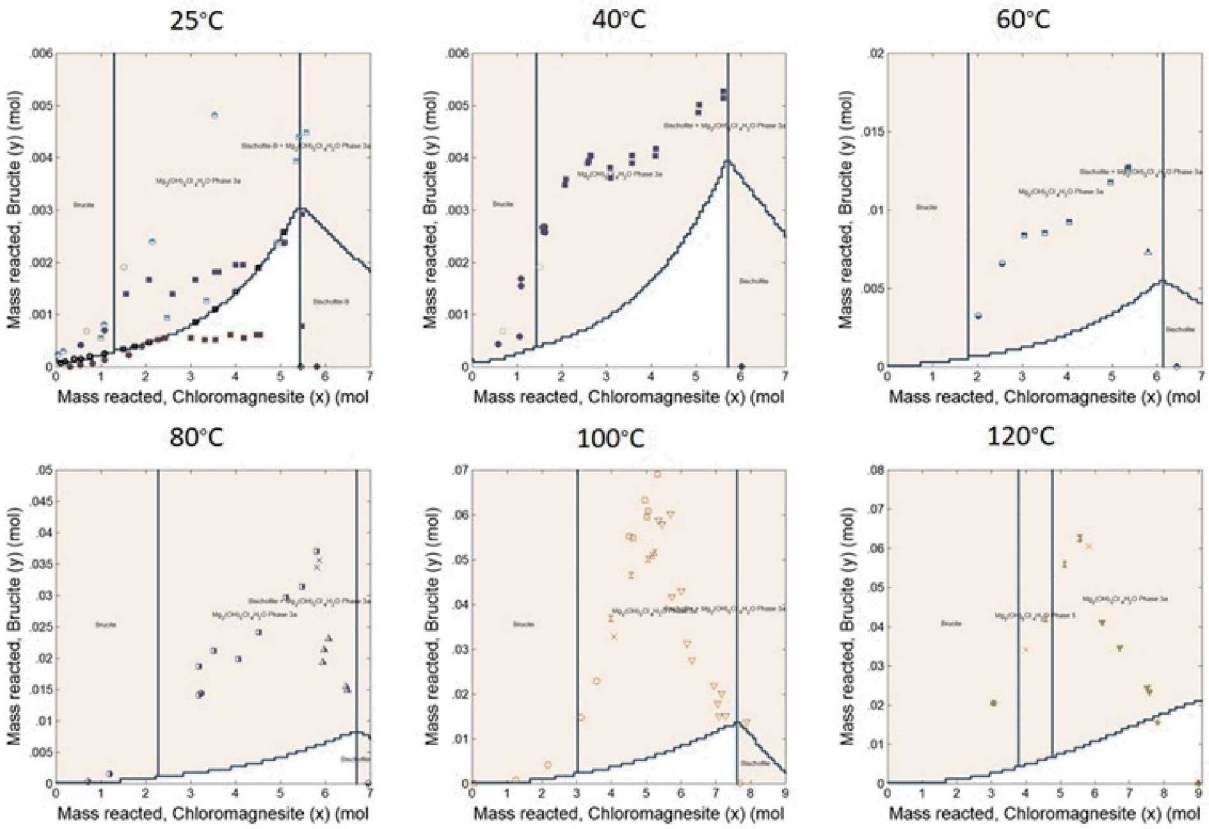

Figure 10. The Mg-OH-Cl system from 25 ºC to 120 ºC comparing our initial calculated LogK values to the experimentally determined solubilities of Mg-bearing mineral phases collected by Pannach *et al.* (2017)

We anticipated that the initial guesses would not fit the experimental data well; the method to calculate the LogK grids was only intended to identify good starting values for further refinement. However, the fits were worse than expected, especially at high temperature. As we have worked to refine the data, we have developed a collaborative relationship with the authors of the experimental data Pannach *et al.* (2017) at Institut für Anorganische Chemie in Germany, and are working together to improve the thermodynamic data for magnesium hydroxychloride species as a function of temperature. The collaborators at the Institut für Anorganische Chemie were also unable to properly fit the experimental data, and as with our predictions, the fits became worse as the temperature increased.

Currently, we are adjusting the LogK values to try to improve the fit with the experimental data, focusing first on lower temperature phases for which there is known thermodynamic data to compare to. Once a robust database for the ambient temperature phases has been stablished, we will fit the LogK values for the higher-temperature phases, for which little or nothing is known.

2.2.2.1 Evaluation of Bischofite, Brucite, and 3-1-8 Magnesium Hydroxychloride Stability at 25 ºC

To being to refine and verify the LogK values, we evaluated the fit between predicted values and experimental data for better known phases (i.e. brucite, bischofite, and 3-1-8 magnesium hydroxychloride) at 25 ºC. First, bischofite stability as a function of temperature and $MgCl_2$ concentration was compared against experimental data (Clynne and Potter, 1979; Krumgalz, 2017). As seen in Figure 11, we have good agreement between the experimental data and the modeled solubilities.

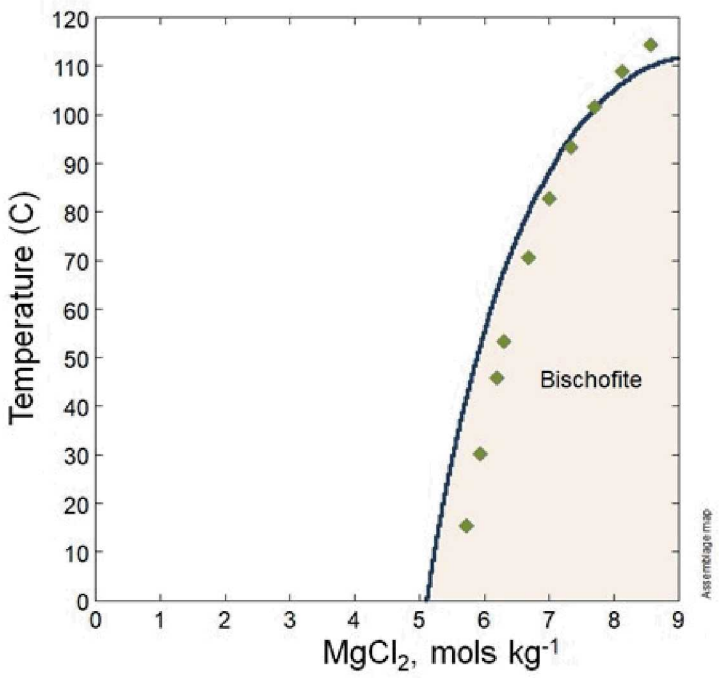

Figure 11. Plot showing temperature versus the amount of $MgCl_2$ in the system comparing modeled bischofite stability versus experimental data (Clynne and Potter, 1979; Krumgalz, 2017).

Hence, the LogK bischofite values in the Yucca Mountain database, from Pabalan and Pitzer (1987), are retained.

Brucite solubility using our derived $LogK_{brucite}$ at 25 ºC was compared to other proposed $LogK_{brucite}$ values (Altmaier et al., 2003; Xiong et al., 2010) and experimental data (Einaga, 1981). The amount of Mg^{++} in solution versus the pH is shown in Figure 12. From the figure, it is clear that the experimental data and the modeled data are slightly shifted. This is likely due to the challenges associated with experimentally measuring the pH in these concentrated brine solutions. Additionally, Eniaga (1981) propose additional aqueous species beyond the ones that exist in the YMP thermodynamic database, specifically $Mg_2(OH_2)^{2+}$ and $Mg_3(OH)_4^{2+}$. The YMP thermodynamic database we use only explicitly accounts for the formation of Mg^{2+} and $MgOH^+$ as Mg-based aqueous species; however, it does include Pitzer interactions that implicitly account for the formation of the $Mg_2(OH_2)^{2+}$ and $Mg_3(OH)_4^{2+}$. Therefore, adding these species explicitly is not possible, as that would result in increasing their potential impact via "double-counting". Our calculated $LogK_{brucite}$ of 16.8763 is in good agreement with the value proposed by Altmaier *et al.*, 2003, $LogK_{brucite}$ =17.1 ± 0.2. *As a preliminary choice, we have decided to keep our $LogK_{brucite}$ at 25 ºC unchanged from the initial calculated value.*

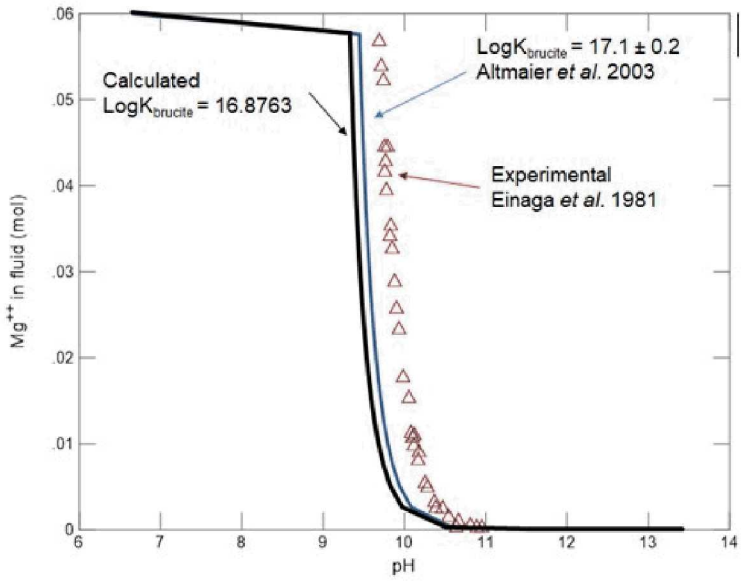

Figure 12. Plot showing [Mg] in solution versus solution pH at 25 ºC comparing calculated LogK$_{brucite}$ (black line), LogK$_{brucite}$ values of Altmaier *et al.* , 2003 (blue line) and experimentally determined data from Einaga (1981)

Keeping the LogK$_{bischofite}$ and LogK$_{brucite}$ at 25 ºC unchanged, the accuracy of our calculated LogK$_{3\text{-}1\text{-}8}$ was evaluated by comparing to experimental studies by Altmaier *et al.* 2003. Using our calculated LogK values, we were able to appropriately predict the phase boundary in the experimental data as seen in Figure 13. However, our predicted solubilities were slightly low. Our calculated LogK$_{3\text{-}1\text{-}8}$ = 25.3669 is slightly outside of the range of uncertainty for the LogK$_{3\text{-}1\text{-}8}$ derived by Altmaier *et al.*2003 (LogK$_{3\text{-}1\text{-}8}$ = 26.0 ± 0.2) by fitting their solubility data (Altmaier *et al.*, 2003).

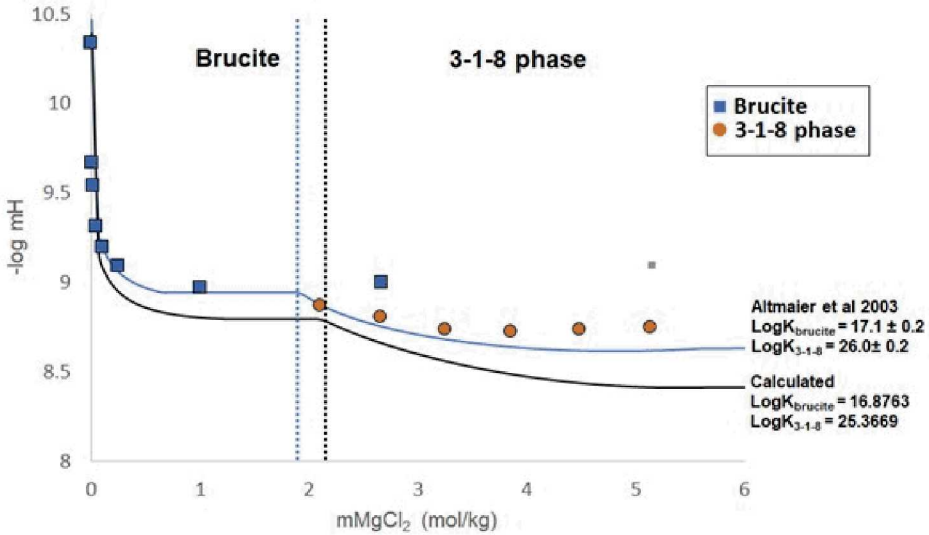

Figure 13. Plot of -log mH$^+$ versus mMgCl$_2$ at 25 ºC showing the solubilities and the phase transition for brucite and the 3-1-8 magnesium hydroxychloride, using LogK values and those Altmaier *et al.* 2003. Solubility data from Altmaier *et al.* 2003 are also shown (note that the gray square represents meta-stable brucite formation).

In Figure 14, we compare the phase diagram generated using our proposed $LogK_{bruite}$ and $LogK_{3\text{-}1\text{-}8}$ with phase boundaries and solubilities generated using the values of Xiong *et al.* (2010) and Altmaier *et al.* (2003), and compare them to the experimental data from Pannach *et al.* (2017) and Robinson and Waggaman (1908) at 25 ºC. There is a great deal of scatter in the experimental data, and our proposed value falls between the two data sets. However, as seen in Figure 14, our estimated logK values most accurately describe the maximum solubility of the system, as defined by the Pannach data, whereas the other LogK values overestimate the solubility significantly. Additionally, our model most accurately fits the phase boundary between brucite and the 3-1-8 phase as indicated by the experimental data of Pannach *et al.* (2017). However, this varies significantly from the phase boundary described by the earlier data of Robinson and Waggaman (1908), which is better fit by the Xiong *et al.* (2010) and Altmaier *et al.* (2003) data. *Because our proposed LogK values seem to capture the overall trend of the experimental data better than the other values, we have decided to keep the $LogK_{3\text{-}1\text{-}8}$ at 25 ºC unchanged from our initial calculated value.*

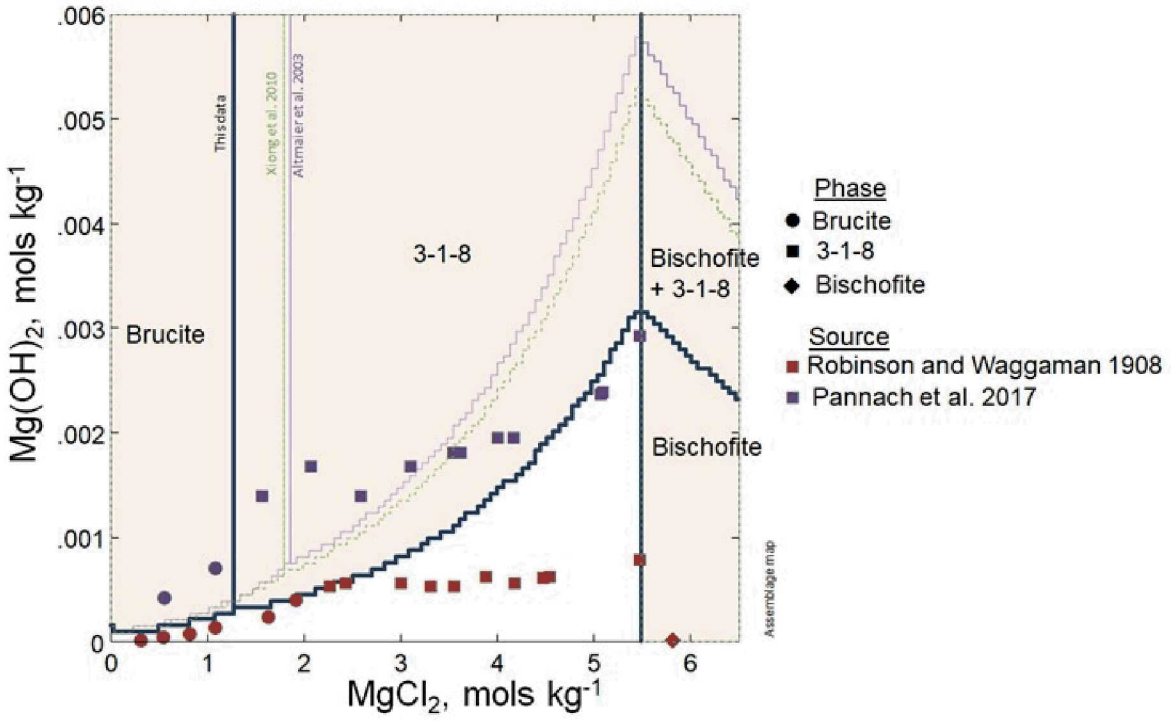

Figure 14. The Mg-OH-Cl system at 25 ºC comparing our calculated $LogK_{brucite}$, $LogK_{3\text{-}1\text{-}8}$, and $LogK_{bischofite}$ compared with those proposed by Xiong *et al.* (2010) and Altmaier *et al.* (2003) presented with experimental data.

2.2.2.2 *LogK Adjustments to Improve the Fit with Experimental Data as a Function of Temperature*

To better fit the experimental data of Pannach *et al.* (2017) at higher temperatures, we iteratively made small adjustments to the LogK values for the phases occurring at higher temperatures and then re-ran the simulation. In GWB, LogK input blocks only exist for 0ºC, 25ºC, 60ºC, 100ºC, and 150ºC; therefore we can only directly adjust values to fit the experimental data at 25 ºC, 60 ºC, and 100 ºC, and allow the software to interpolate between those LogKs to estimate values at 40 ºC, 80 ºC, and 120 ºC. As discussed previously, our calculated LogK values at 25 ºC have been retained, so those remained unchanged while the LogK values at 60 ºC and 100 ºC were adjusted to qualitatively best fit the experimental data in terms of phase solubility and phase boundaries.

Adjusted LogK Values to Fit 60º Experimental Data

At 60 ºC, the simulation using the initial calculated LogK values for 60ºC did not fit the experimental data well, as seen in Figure 15 (gray line); the solubility of the system is underestimated, the phase boundaries are incorrect, and the simulation was unable to predict the formation of the 2-1-4 phase, which forms at higher concentrations of $MgCl_2$. The improved fit, as seen in Figure 15 (heavy blue line), involved adjusting the 60ºC LogK values as follows: $LogK_{brucite}$ from 17.7804 to 15.37, $LogK_{3\text{-}1\text{-}8}$ from 22.4905 to 23.8, and $LogK_{2\text{-}1\text{-}4}$ from 37.1018 to 34.29. The 5-1-8 phase was suppressed as there was no experimental data to fit it to (it is generally considered to be metastable). While the simulation with the adjusted LogK values accurately predicts the maximum solubility of the system and the phase boundaries, it fails to accurately fit the shape of the solubility curves, especially the change in slope that occurs when new phases are formed. The largest discrepancies was the apparent solubility of the 2-1-4 phase, which experimentally precipitated at ~5.9 M $MgCl_2$ and ~ 0.0075 M $Mg(OH)_2$, whereas our model predicts a much higher solubility. The 2-1-4 phase is a phase of interest to us; from these results, we would likely be able to determine the concentration of Mg required for the 2-1-4 phase to form, but the predicted solubility of the phase would be much higher than the experimental data suggests.

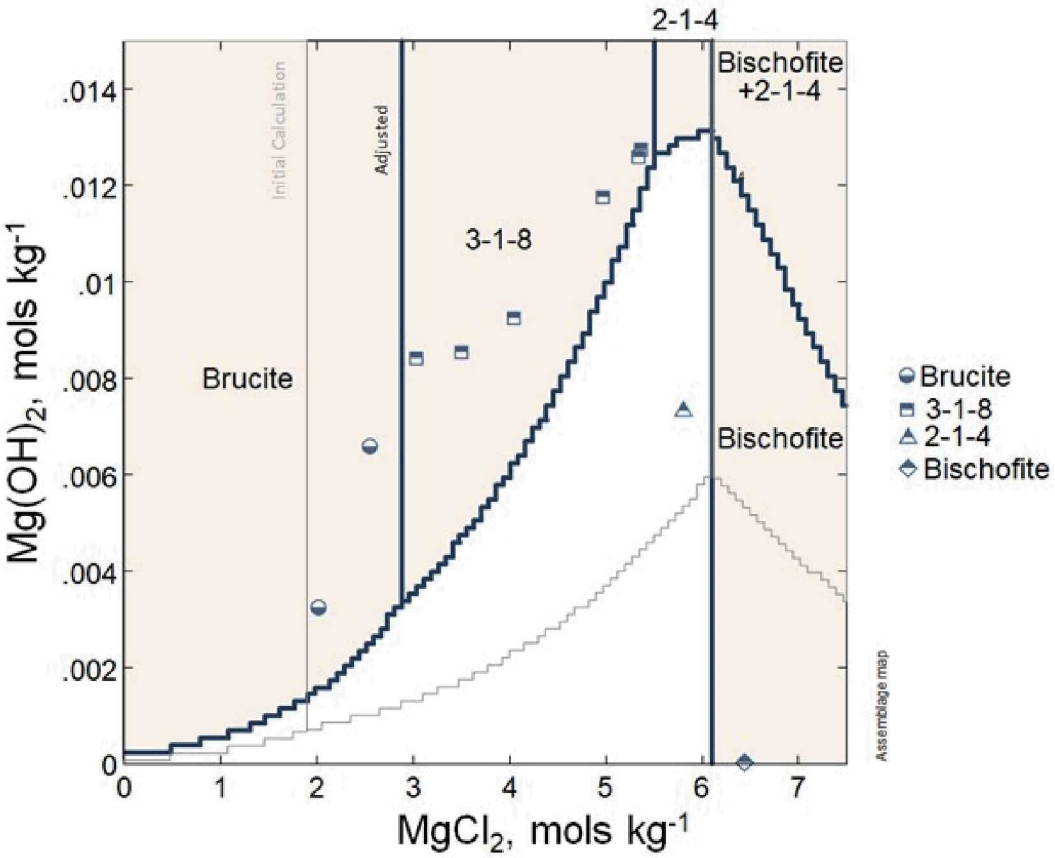

Figure 15. The Mg-OH-Cl system at 60 ºC where the gray line is the solubility using initial LogK values, and blue line is our adjusted LogK values to fit the data.

Adjusted LogK Values to Fit 100º Experimental Data

The simulated fit using the original calculated LogK values at 100 ºC can be seen in Figure 16 (gray lines). Phase solubilities are underestimated, with the deviation increasing as the temperature increases; the initial fit at 100ºC is very poor, and completely fails to predict the formation of the two high

temperature phases seen experimentally, the 9-1-4 and 2-1-4 hydroxychlorides. The improved fit (blue lines) was the result of adjusting the 100ºC LogK values as follows: $LogK_{brucite}$ from 12.9061 to 14.4728, $LogK_{3\text{-}1\text{-}8}$ from 19.9275 to 23 (shown as a metastable phase experimentally), $LogK_{9\text{-}1\text{-}4}$ from 122.6914 to 132.8, $LogK_{2\text{-}1\text{-}4}$ from 32.3494 to 32.3, and $LogK_{2\text{-}1\text{-}2}$ from 35.0495 to 32.85. The 5-1-8 phase was again suppressed. Overall, the fit is greatly improved; our predicted phase boundaries and solubilities for brucite and the 9-1-4 phase appear to be in good agreement, and even match the invariant point (~ 4 M $MgCl_2$ and ~0.03 M $Mg(OH)_2$). However, the simulation does not predict the formation of the 2-1-2 and 2-1-4 phases accurately; the formation of the 2-1-4 phase is not predicted at all and the 2-1-2 phase is predicted to be stable over the entire range occupied by both phases in the experimental data. This result was actually intentional because the it resulted in a more rapid decrease in the amount of $Mg(OH)_2$ in the system as the amount of $MgCl_2$ increased. It is also not entirely certain how accurately the phase boundary between the 2-1-2 and 2-1-4 phases is known, especially at 100 ºC. Pannach *et al.* (2017) mention that the 2-1-4 phase can transform into the 2-1-2 phase as the $MgCl_2$ content increases. The authors identified the Mg hydroxychloride phase *via* XRD, and the reported pattern for the 2-1-4 phase has a high signal-to-noise ratio; moreover, there is no reported pattern for 2-1-2 phase, so the identification of this phase may be questionable.

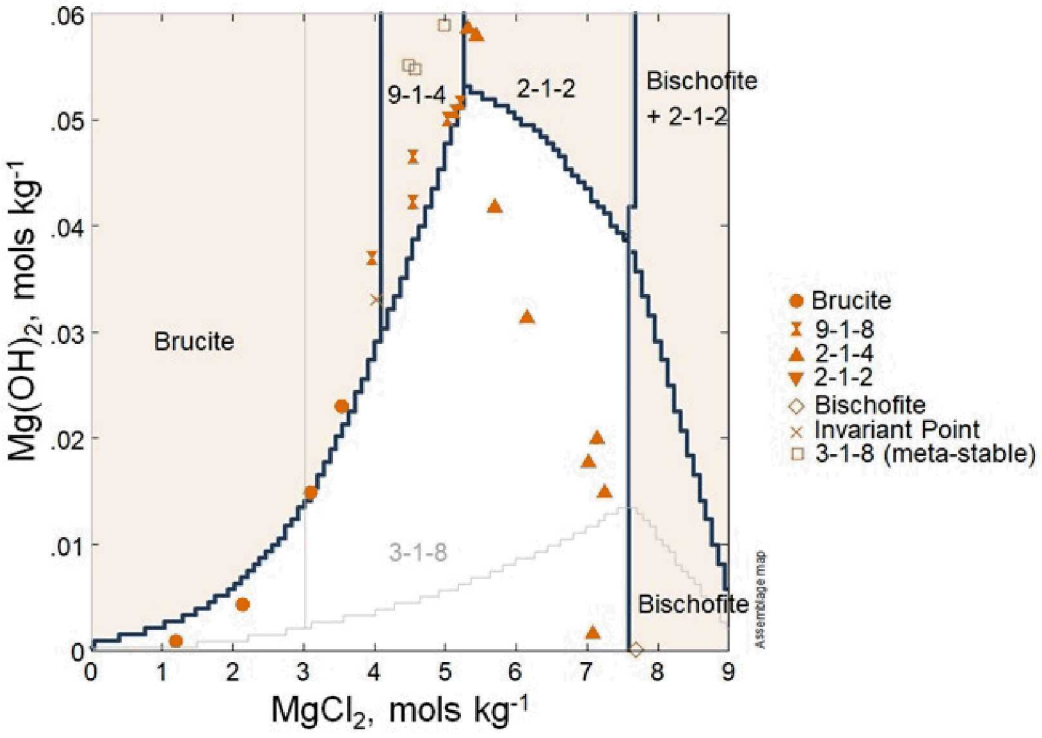

Figure 16. The Mg-OH-Cl system at 100 ºC where the gray line is the solubility using initial LogK values, and blue line is our adjusted LogK values to fit the data.

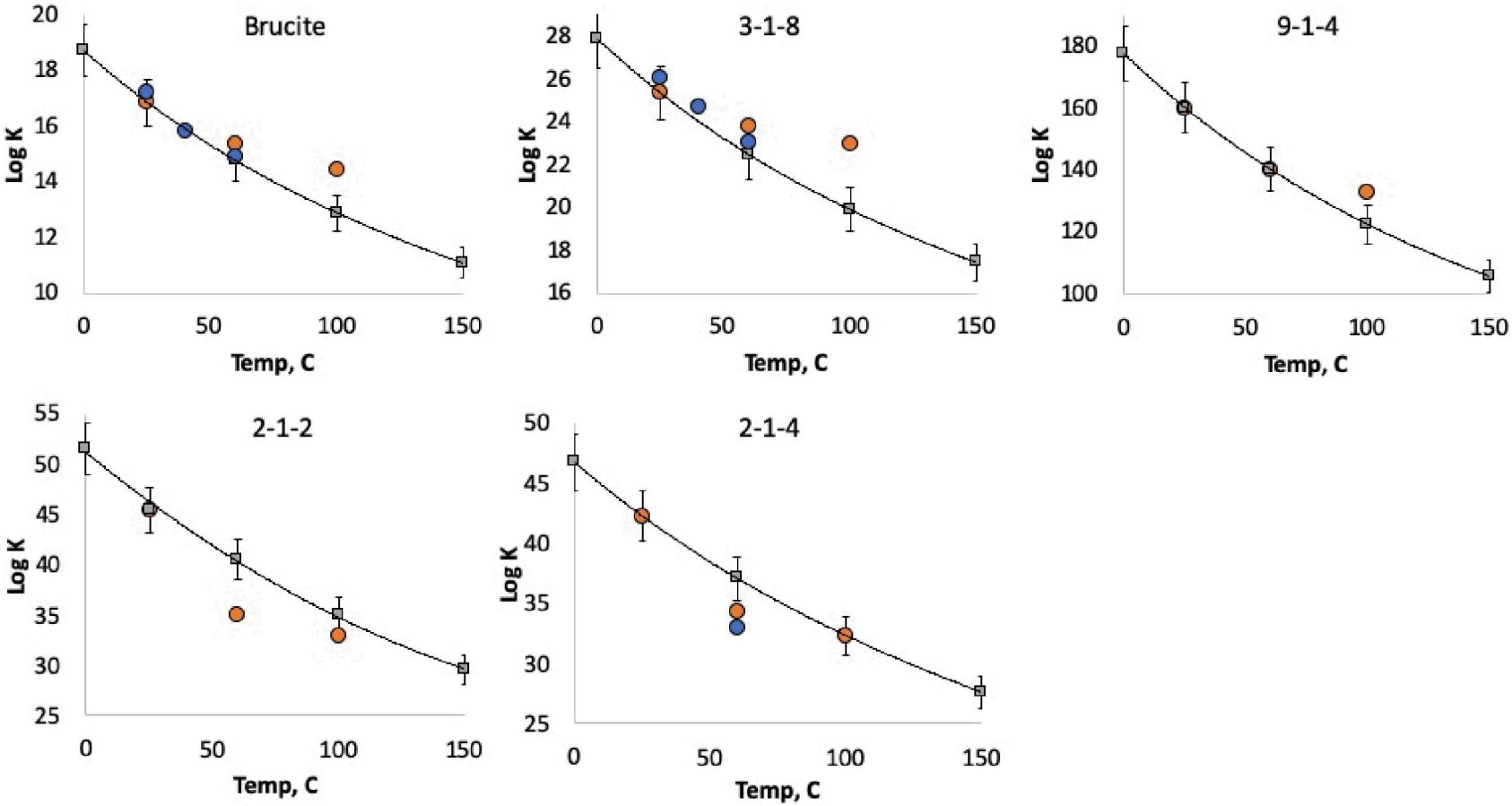

Figure 17. LogK grids as a function of Temperature showing the initial calculation (line and grey square), adjusted LogK (orange circle), and literature Log K values (blue circle).

A comparison of the LogK values from the initial calculation, adjusted to fit experimental data, and other proposed values (Pannach, 2019) is shown in Figure 17. In general, the initial calculated values agree well at lower temperatures, however as the temperature increased, the LogK values had to be increasingly adjusted to fit the data. In some cases, the adjustments made were relatively small and reasonable. However, large changes, like the adjustment of 10 LogK units made for the 9-1-4 phase at 100 ºC, suggests larger issues. Additionally, when there are other proposed LogK values to compare to (Pannach, 2019), both our adjusted values and the proposed values are shifted to higher LogK values than our initial guesses indicated. This is consistent with the consistent underestimation of the solubility using our initial values.

A composite assemblage plot of $MgCl_2$ versus temperature with a fixed amount of brucite in the system (0.075 mols/kg^{-1}), is plotted with experimental data from Pannach *et al.* (2017), shows the quality of the fit as a function of the temperature (Figure 18). As mentioned previously, at lower temperatures (<60 ºC) the predicted phases and solubilities match well with experimental data. However, as the temperature increases, the fit grows progressively worse; it is poor at predicting the stability fields for the 2-1-4 and 2-1-2 phases, and the 9-1-4 region is completely incorrect. The poor model fit at 80 ºC may be in part due to having to adjust the LogK values in the temperature grid at 60ºC and 100ºC to change the values used at 80 ºC.

One reason for the greater discrepancy between predicted values and experimental values at high temperatures could be associated with the challenges of experimentally performing the high temperature analysis. We are having discussions with the authors of Pannach *et al.* (2017) and have discussed mutual challenges in fitting the high temperature data. Without additional experimental data, we are limited to fitting our LogK values to the Pannach *et al.* (2017) dataset.

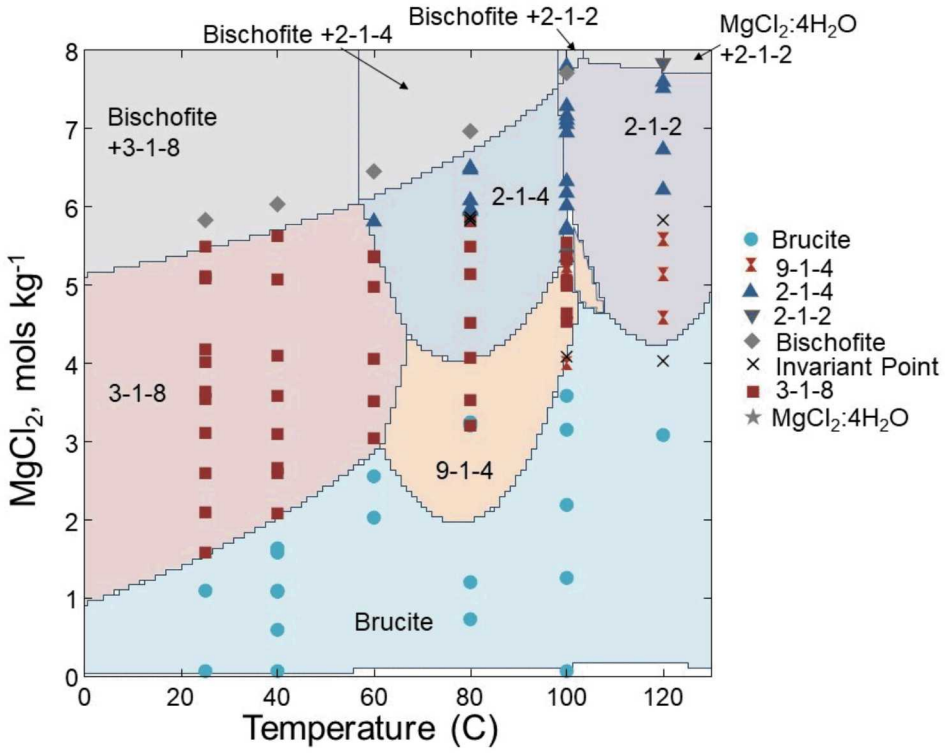

Figure 18. Mg-OH-Cl system as a function of temperature and $MgCl_2$ with a fixed amount of $Mg(OH)_2$ added (~0.075 mols/kg^{-1}) . The LogK values have been adjusted to best fit the experimental data from Pannach *et al.* (2017).

The final set of LogK values, adjusted for the best fit to the experimental data, are shown in Table 10, with the adjusted values in boldface. Work continues to improve the fit to the experimental data at higher temperatures.

Table 10. Updated LogK grid [0-25-60-100-150] for the dissociated reaction of various Mg-bearing mineral phases calculated using CHNOSZ and adjusted to fit experimental data.

Reaction	Short Name	0 ºC	25 ºC	60 ºC	100 ºC	150 ºC
$Mg(OH)_2 + 2H^+ \leftrightarrow Mg^{++} + 2\,H_2O$	Brucite	18.7256	16.8763	15.37	14.4728	11.0969
$MgCl_2{:}6H_2O \leftrightarrow Mg^{++} + 2Cl^- + 6\,H_2O$	Bischofite*	4.5811	4.3570	4.0253	3.6643	3.2042
$Mg_2(OH)_3Cl{:}4H_2O + 3\,H^+ \leftrightarrow 2\,Mg^{++} + Cl^- + 7\,H_2O$	3-1-8	27.8999	25.3669	23.8	23[b]	17.4543
$Mg_3(OH)_5Cl{:}4H_2O + 5\,H^+ \leftrightarrow 3\,Mg^{++} + Cl^- + 9\,H_2O$	5-1-8[a]	46.6257	42.2434	37.270	32.8336	28.5463
$Mg_3(OH)_4Cl_2{:}2H_2O + 4\,H^+ \leftrightarrow 3\,Mg^{++} + 2\,Cl^- + 6\,H_2O$	2-1-2	51.6354	46.5187	40.5524	32.85	29.5253
$Mg_3(OH)_4Cl_2{:}4H_2O + 4\,H^+ \leftrightarrow 3\,Mg^{++} + 2\,Cl^- + 8\,H_2O$	2-1-4	46.7816	42.2976	34.29	32.3	27.6207
$Mg_{10}(OH)18Cl_2{:}4H_2O + 18\,H^+ \leftrightarrow 10\,Mg^{++} + 2\,Cl^- + 22\,H_2O$	9-1-4	177.8625	160.4330	140.5648	132.8	105 918

*LogK grid for bischofite remained unchanged from data0.ymp, original source (Pabalan and Pitzer, 1987).

[a] Phase was suppressed because no experimental data available.

[b] Phase was meta-stable in the experimental data set.

2.2.3 Path Forward

In FY20, we plan to continue to improve the LogK values to accurately predict the solubility and stability fields of the magnesium hydroxychloride phases as a function of temperature and composition, to improve our ability to predict the evolving brine environment on the surface of the SNF dry storage canisters. As shown in Figure 19, the deliquesce RH for a magnesium chloride brine is highly dependent upon which phase is stable on the SNF canister surface. If bischofite degasses to form a magnesium hydroxychloride phase, as seen in laboratory experiments, sea-salt brines will require a much higher RH, and hence a much lower temperature on the canister surface, before deliquescence will occur, which would delay the timing of SCC initiation. Working closely with the group at Institut für Anorganische Chemie, we will create a consistent thermodynamic database that appropriately agrees with the experimental observations. Additionally, we will synthesize and characterize magnesium hydroxychloride phases ourselves to further characterize their properties and conditions of stability. Our ultimate goal is to develop and experimentally verify a set of LogK values for use in predicting magnesium-containing brine stabilities on a heated SNF storage canister surface.

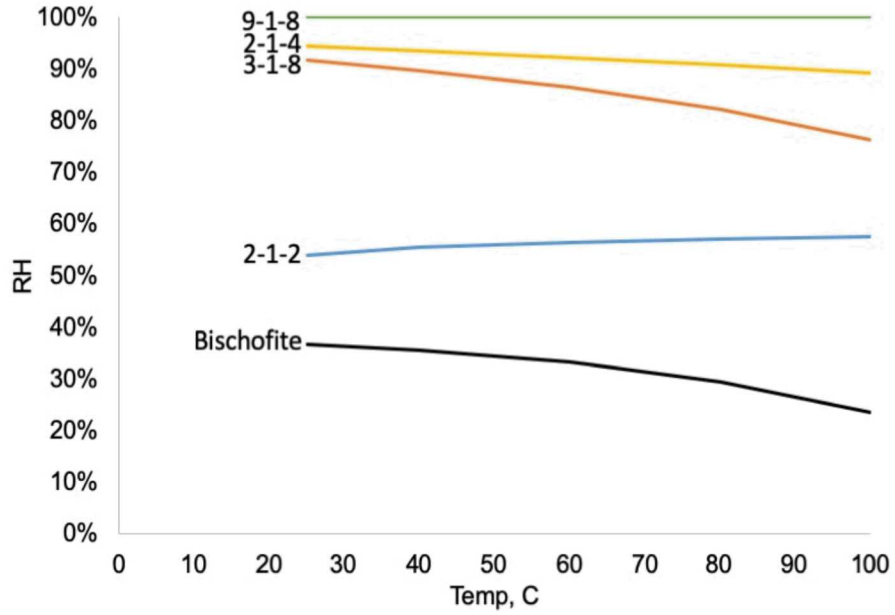

Figure 19. Predicted deliquescence RH as a function of temperature for the Mg-OH-Cl system using LogK values derived from fitting the experimental data.

This page is intentionally left blank.

3. Parameterization of the Maximum Pit Size Model

As discussed in Bryan and Schindelholz (2018), corrosion of SNF dry storage canisters at near-marine Independent Spent Fuel Storage Installations (ISFSIs) occurs because sea-salt aerosols are deposited on the metal surfaces and deliquesce to produce corrosive, chloride-rich brines. The character and extent of corrosion is believed to be linked to the chemical and physical properties of the deliquescent brines, and these properties are strongly governed by environmental parameters including relative humidity (RH), temperature, deposited salt load, and distribution of salts on the metal surface. The SNL probabilistic SCC model (O'Brien *et al.*, 2019) utilizes these parameters to calculate the properties of the brine layer that is present on the canister surface. These brine properties are then used to estimate the maximum possible cathode current, and in turn, the maximum possible pit size that can be present at any given canister surface location and point in time. As pits grow larger, transition to a SCC crack becomes more and more likely. The maximum pit size model is based on that of Chen and Kelly (2010). The maximum cathode current is given by the following equation:

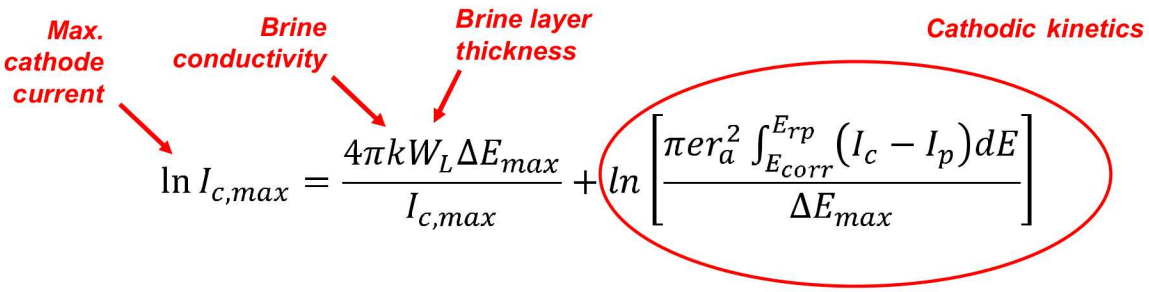

Where:

$I_{c,max}$ = maximum cathode current, Amps

k = brine conductivity, Siemens/meter

W_L = brine layer thickness, m

E_{rp} = repassivation potential, V_{SCE}

E_{corr} = corrosion potential, V_{SCE}

$\Delta E_{max} = E_{corr} - E_{rp}$

I_c = cathode current density, Amps/meter^2

I_p = passive current density, Amps/meter^2

R_a = pit diameter, m

e = Euler's number, 2.71828

The maximum cathode current is a function of brine conductivity, brine layer thickness, and electrochemical parameters that determine the kinetics of oxygen reduction at the cathode—the region surrounding the pit. In order to parameterize this equation, we have experimentally evaluated each of these parameters over a range of brine compositions.

3.1 Brine Properties

We have implemented standard thermodynamic modeling to determine the composition of brines formed by sea-salt deliquescence, as a function of RH and temperature. This process is described in a previous SFWST report (Schindelholz, 2017), and is not repeated here. We then mixed brines to represent specific RH values and characterized those brines, measuring conductivity and density. The theoretical and experimental data were used to calculate brine volumes as a function of RH and salt load. We have also

estimated and measured brine viscosities and dissolved oxygen concentrations, two parameters that are important for interpreting measured cathodic polarization curves to understand processes controlling cathode kinetics. These data provide insights into the structure and composition of deliquescent brines. With measured cathodic polarization curves and anodic kinetics described later in this section, the data provide the necessary inputs to both test the validity of the maximum put size model and to evaluate potential limits on the extent of atmospheric corrosion on heated metal surfaces.

To estimate these values over the range of interest, several brine compositions along the predicted evolutionary pathway for seawater evaporation at 25ºC were mixed using ACS certified salts, and the above properties were measured experimentally. The brines correspond to the predicted compositions at RH values of 98.15% (unevaporated seawater), 90%, 78%, 73.4%, 66%, 56%, and 38%. The compositions are given in Table 11. Using these brines predicted for sea-salt deliquescence at 25ºC introduces some error at other temperatures; however, the errors are relatively small, and these brines are stable at room temperature and higher temperature allowing simple mixing and brine property measurement. Otherwise, individual brines would have to be mixed at each temperature of interest.

Table 11. Composition of brines used for experimental measurement of brine properties

Brine RH	Species Concentration (molality)									
	Na^+	K^+	Mg^{2+}	Ca^{2+}	Cl^-	Br^-	F^-	SO_4^{2-}	BO_3^{3-}	HCO_3^-
SW - 98.19%	0.486	0.011	0.055	0.010	0.567	0.001	0.0001	0.029	0.0004	0.002
90%	2.337	0.05	0.266	0.031	2.723	0.004	—	0.126	0.002	0.001
78%	4.507	0.096	0.513	0.015	5.25	0.008	—	0.196	0.004	0.006
73.4%	5.225	0.111	0.597	0.011	6.109	0.009		0.210	0.005	0.011
66%	2.047	0.166	2.701	0.004	6.396	0.047		0.568	0.024	0.032
56%	0.719	0.144	3.907	0.003	7.941	0.077	—	0.289	0.04	0.064
38%	0.145	0.032	5.500	0.003	10.61	0.181	—	0.059	0.093	0.215

Brine conductivities were determined over a temperature range from ambient room temperature to ~65ºC, using a Jenway 4510 conductivity meter with a maximum working temperature of 80ºC and Jenway conductivity probes with ranges of 0-150 mS/cm and 0-500 mS/cm. For any given brine, measured conductivities increase linearly as a function of temperature, so these data can be used to estimate brine conductivities at moderately higher and lower temperatures. Brine densities are necessary for calculating brine volumes from the thermodynamic model results. They were measured for the brines of interest over a range of temperatures, using Durac hydrometers calibrated for specific gravity ranges 1.000-1.220 and 1.20-1.420 (density and specific gravity differ by less than 0.01%). The hydrometers were calibrated at temperatures of 60ºF (15°C) and a slight error is introduced at other temperatures. Hydrometer accuracies at temperatures above their calibration temperature were verified by measuring the density of saturated NaCl solutions at the temperatures of interest, as described by Thurmond *et al.* (1984). Measurement errors were less than 0.005 units.

Other brine properties of interest are those that contribute to the kinetics of oxygen reduction at the cathode. These include brine viscosity (a metric for O_2 diffusivity), and dissolved oxygen concentration. Brine viscosities were measured over the temperature range from 20º to 60ºC using a Brookfield AMETEK LDTV2T Viscometer with a low viscosity adaptor. Finally, dissolved oxygen concentrations were measured for some brines at selected temperatures using the standard iodometric titration technique (Carpenter, 1965), to verify predictions from the thermodynamic model. The results of these measurements are shown in Figure 20.

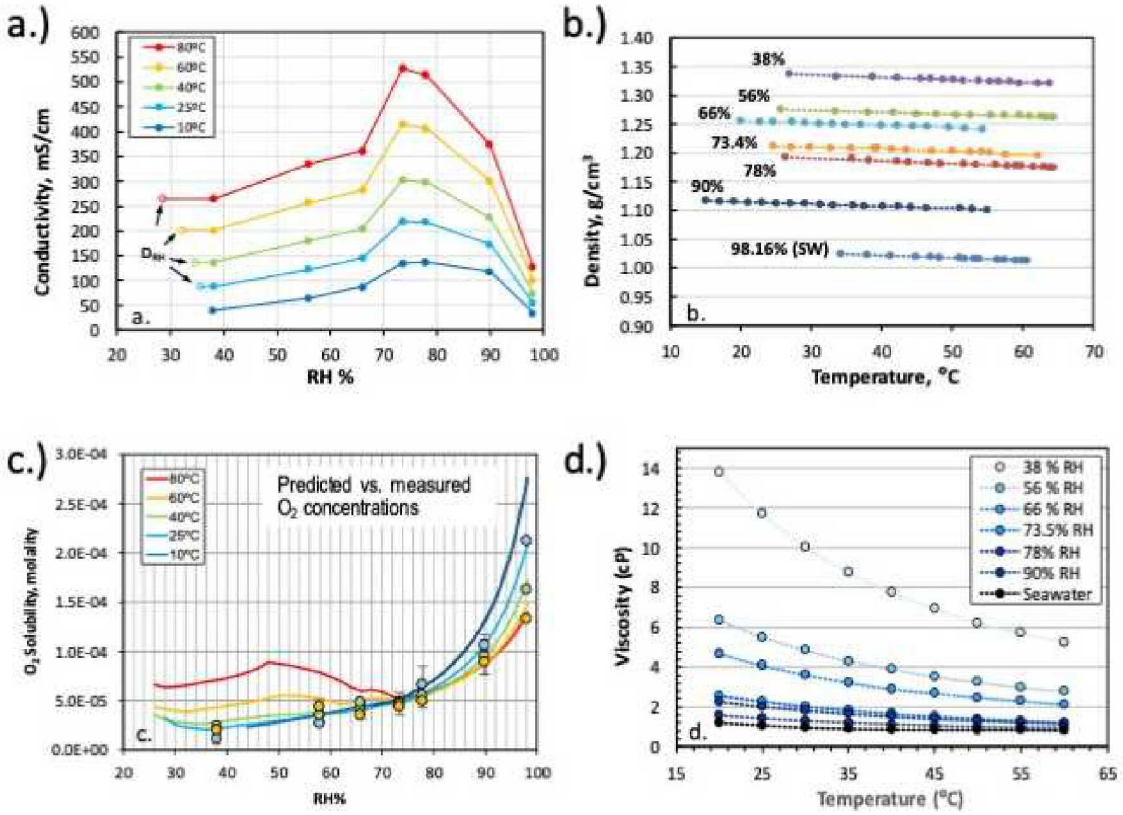

Figure 20. Brine properties as a function of temperature and RH. a) Conductivity; b) density; c) dissolved oxygen concentration (solid lines are modeled values, points are measured values); d) brine viscosity.

Along with brine-specific determination of cathodic and anodic kinetics described below, these data can be used to parameterize the Chen and Kelly maximum pit size model.

3.2 Cathodic Kinetics

As previously established, parameterization of the cathodic kinetics pertinent to the maximum pit size model is key to establishing an overall SCC model for ISFSI relevant conditions. Current deterministic models for atmospheric pitting and SCC provide insight into how surface environmental conditions can affect kinetics and extent of damage (Macdonald and Urquidi-Macdonald, 1991; Newman, 2002; Chen and Kelly, 2010). In several SCC and pitting models, the surface external to the crack (or pit) acts as the cathode, supplying the electrochemical driving force for pit or crack growth (Figure 21). Thus, under atmospheric conditions, the surface environment, dependent on humidity, temperature and aerosol deposition, would be expected to control damage rates. The relationship between surface state and electrochemical processes (cathodic kinetics) outside of a pit or a crack and electrochemical processes within them is not well understood. Efforts in this thrust aim to address this by quantitatively linking expected canister surface conditions to the electrochemical processes driving pitting and SCC, using existing models as initial basis for understanding.

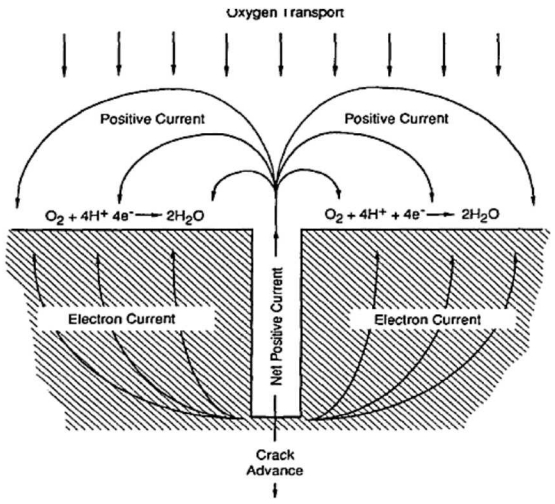

Figure 21. Conceptual schematic of electrochemical SCC model proposed by MacDonald showing coupling of oxygen reduction reaction on steel surface with internal environment From Macdonald and Urquidi-Macdonald (1991).

Of initial interest is the impact of expected surface electrolyte physicochemical state on cathodic electrochemical kinetics that drive corrosion on stainless steel surfaces. In FY18, experiments were performed to measure the oxygen reduction reaction (ORR) kinetics on 304L and 316L in analog brines representative of chemistries and conditions expected on canisters. In FY19, this was expanded to include additional brine solutions as well as anodic kinetics. Anodic kinetics in ISFSI relevant brines help establish specifically the pit stability product ($(i \cdot x)_{sf}$) and the repassivation potential (E_{rp}), for input into the maximum pit size model and prediction of maximum pit depths. Additionally, kinetic parameters were explored in surrogate alkaline brines, devoid of chlorides, to determine the effect of surface chemistry on subsequent cathodic kinetics. Datasets generated from maximum pit depths will serve as direct input for SNL's current probabilistic SCC model.

As mentioned, in FY19, measurements focused on relevant NaCl solutions, but were expanded to include other sea salt and simulated brines expected under canister relevant conditions ($MgCl_2$ and artificial seawater (ASW)) as well as alkaline solutions. The focus was to both generate data as input for SNL's SCC model and develop an understanding of cathodic and anodic kinetic mechanisms controlling pit growth and the maximum pit size. The NaCl study findings are summarized in a journal paper (see Appendix B). Nonetheless, a brief summary of the type of data collected and how it can be applied in the SNL SCC model is provided here.

Figure 22 shows representative polarization curves measured on 304L after cycles of anodic holds to determine relevant pitting parameters, E_{rp} and $i_{lim,}$ as inputs for the maximum pit size model developed by Chen and Kelly (2010). From i_{lim}, the pit stability product $(i \cdot x)_{sf}$ with the application of Fick's first law can be determined as follows:

$$i_L d = nFD_{M+}\Delta C = nFD_{M+}C_{M+}^{sat} = (i \cdot x)_{sf} \quad \text{(Eq. 7)}$$

Where n is the number of electrons transferred, F is Faraday's constant ($F = 96{,}485\ C/mol$), D_{M+} is the diffusion coefficient of metal cations, and ΔC is the concentration difference of metal cations at the bottom of the pit and the bulk solution and it is assumed that the concentration at the mouth of the pit is zero at sufficiently deep pits.

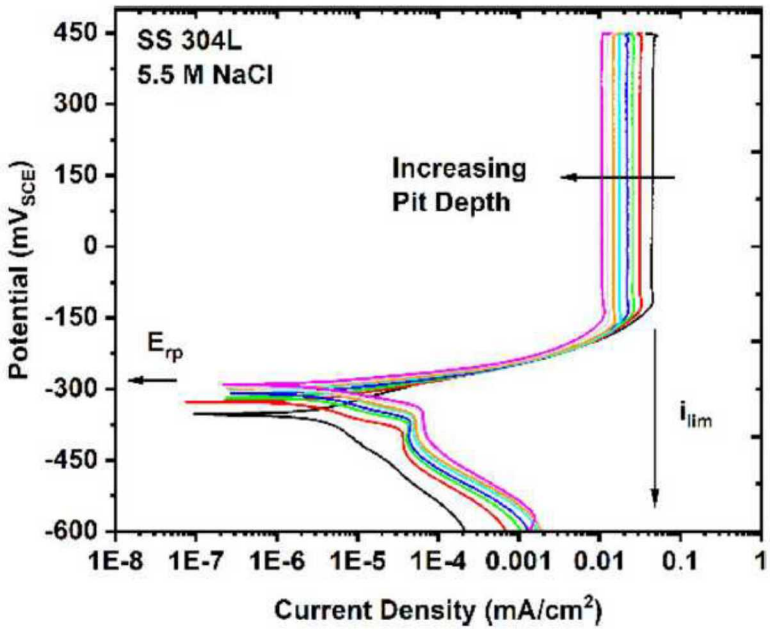

Figure 22. Successive polarization scans of SS304L in 5.5 M NaCl at 25°C after pit growth by anodic holds at both +750 mV_{SCE} and +450 mV_{SCE}. Cathodic polarization was initiated at +450 mV_{SCE} and scanned to −600 mV_{SCE} at a scan rate of 5 mV/sec. Extraction of desired parameters, E_{rp} and i_{lim} are labeled.

The maximum pit size, r_{max}, can be determined from the intersection of the anodic current demand:

$$I_{LC} = \left(\frac{i_{pit}}{r_{pit}}\right)_{crit} r_a \qquad \text{(Eq. 8)}$$

where i_{pit}/r_{pit} is the pit stability (related to $i{\cdot}x$ by geometry) and I_{LC} is the current required to produce a pit of radius r_a, with the maximum cathode capacity (calculated from the acquired cathodic polarizations). Results of calculations for 0.6 and 5.5 M NaCl are shown below in Figure 23, where the intersection of the I_{cath} (solid line) and the corresponding I/r (dotted line) represents the maximum pit size predicted under the tested brine and exposure conditions. Using the maximum pit size framework, the combination of appropriate anodic and cathodic kinetics yields an increase in pit size and cathode radius with increasing chloride and temperature. It is significant to note, that in both cases, the effect of increasing chloride is larger than that of increasing temperature over the ranges studied.

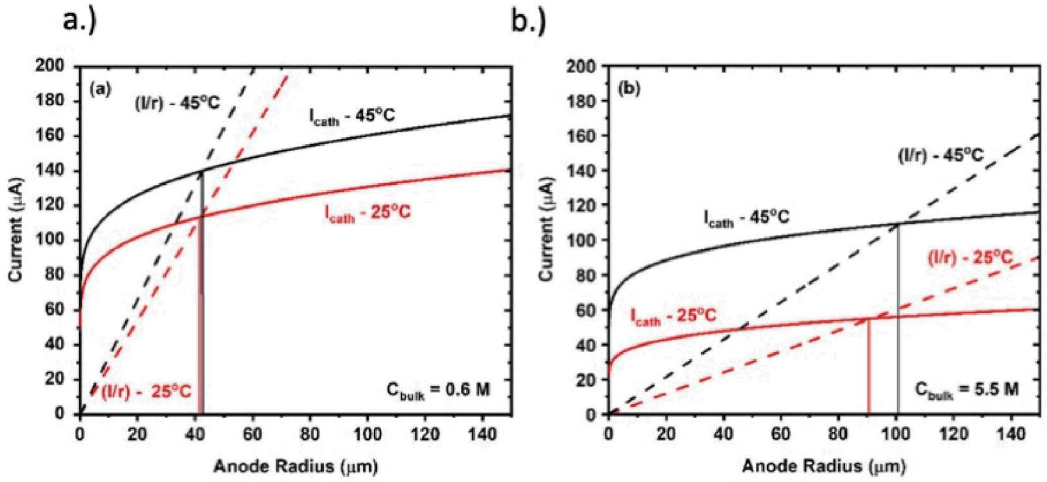

Figure 23. Cathode current and anode current for a.) C_{bulk} = 0.6 M and b.) 5.5 M NaCl at both 25°C and 45°C. A salt loading density of 200 μg/cm^2 was used in these calculations.

While the data provided in this figure should only be taken as conceptual, given several assumptions made in the model, critical combinations of environmental parameters at which there is a risk of SCC can be defined through the maximum pit size model and empirical measures of electrochemical kinetics. These assumptions here include treating the pits as hemispherical in shape, the brine layer as a uniform thin film with static properties, and exposure in a homogeneous material and mechanical environment (e.g., stress/strain). Additional experiments performed in FY19 in $MgCl_2$ solutions (Figure 24) highlight some of the possible limitations of the assumptions in the currently applied maximum pit size model. In $MgCl_2$ solutions, it has been demonstrated that while cathodic reduction on platinum alloys follows the 2-electron oxygen reduction reaction (ORR), cathodic reductions on SS304L are a mix between ORR and the hydrogen evolution reaction (HER) becoming dominated by HER in saturated solutions (Figure 24). It was determined that HER was caused by a buffering effect of the Mg^{2+} ion in solution by the formation of $Mg(OH)_2$. When the pH is buffered, the surface pH decreases, and decreases the over potential for HER, causing HER to become the primary reaction. Solution conductivity is one of the important factors in the current pitting model. When there are solid products, such as an insoluble hydroxide or carbonate, the conductivity decreases in solution. In addition, cathodic sites can be physically blocked as solids precipitate. A decrease in conductivity will decrease the overall cathodic current available for dissolution, thus the maximum achievable pit size will decrease, all else being held constant. This is currently unaccounted for, as the current model applies the assumption of a constant brine without changing conductivity over time. Another phenomenon that can occur in these $MgCl_2$ solutions is dry-out of the cathode. As pointed out by Bryan and Schindelholz (2018), highly deliquescent $MgCl_2$ can be replaced with a non-deliquescent solid and the brine will dry out as reactions on the surface (corrosion) progress to completion (Figure 25). This means one of two things can happen: (1) the equivalent cathode size can decrease or (2) the water layer will decrease. In both cases, the current the cathode can supply will decrease, and decrease the maximum attainable pit on the surface. Again, in the current maximum pit model, dynamic brine conditions, such as dry-out, are unaccounted for. This unique phenomenon may have the possibility to decrease the severity of pitting corrosion due to decreased conductivity and brine dry-out. However, an increase in SCC due to hydrogen embrittlement is of concern as hydrogen, produced by HER, will be readily available on the cathode surface near a pit.

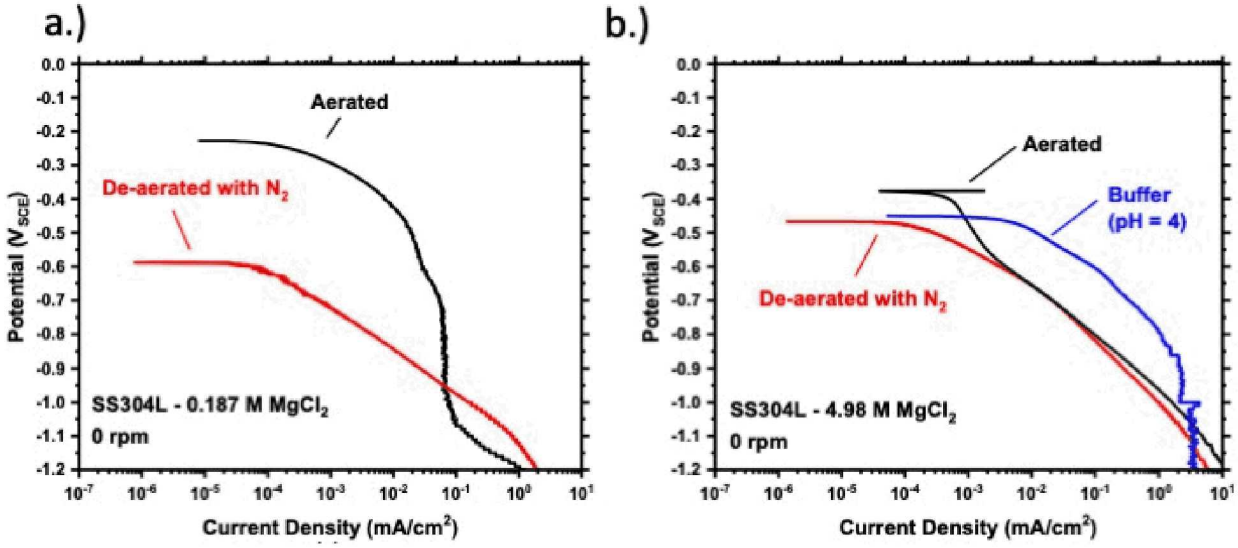

Figure 24. Comparison of aerated and de-aerated with N_2 for a.) 0. 187 M and b.) 4.98 M $MgCl_2$ under aerated conditions. Also shown in b.) is a polarization scan with an acetic acid buffer added to solution.

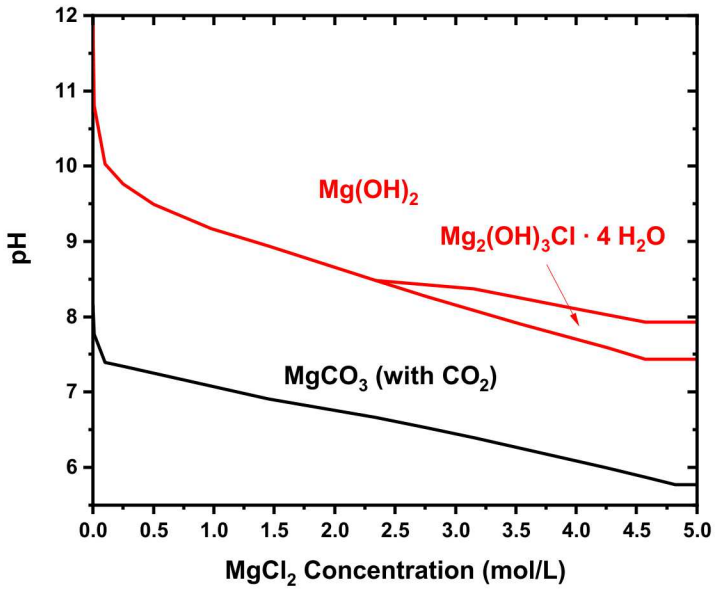

Figure 25. Stability diagram for dissolved $MgCl_2$ created in EQ3/6 using the Yucca Mountain Program thermodynamic database with the utilization of the Pitzer formulism.

The maximum pit size model is currently incorporated into SNL's probabilistic model to determine bounding pit sizes on canisters as function of environment. With respect to the pit to-crack-transition, this model uses the Kondo criterion and uses the predicted maximum pit size to determine conditions under which pit-to-crack transition is most likely to occur. Similarly, conditions where cracking will not take place can also be determined. If the theoretical maximum pit size is smaller than the critical pit size

required for SCC crack initiation (given the local stresses and environmental conditions that are present) then crack initiation is unlikely. Thus, if the environmental parameters and material properties for a system are known, this model can be used to map regions where there is a risk of SCC, requiring more detailed experimentation. Although of great potential utility, this model has not been benchmarked under canister-relevant conditions. Pitting statistics collected in FY18 and 19 will aid in providing a large dataset with which to explore the applicability of the Chen and Kelly model. This will provide insights into the validity of the assumptions made in these models, i.e., the assumption of hemispherical pit geometry. It is clear from the datasets presented that pit morphologies often deviate from the hemispherical assumption. Benchmarking the model with these datasets will allow determination of the significance of the assumption of a hemispherical pit, and whether it is valid for ISFSI conditions. Reliable determination of the maximum pit size, applicability of the Kondo criterion if a non-hemispherical pit is present (for instance, how greatly will stress concentrators and thus K_{ISCC} be altered if the pit is irregular?), and the subsequent SCC cracking susceptibility in ISFSI-relevant conditions are all dependent on these assumptions; thus, their validation is key. Other assumptions made within the model must also be tested, such as the static environmental conditions (which are known to vary over time and throughout the corrosion process), the presence of a continuous electrolyte thin film (under atmospheric exposures, a brine film on metal commonly occurs as droplets), and the homogenous material and stress conditions (these parameters known to vary across canisters, specifically at welds). Each of these assumptions is being addressed through the corrosion studies presented here.

To address the influences of one of these assumptions, preliminary studies in FY19 explored the extent to which brine evolves on the surface and how, in turn, this evolution can impact cathodic corrosion kinetics through the application of a dual-electrode droplet experiment (Figure 26-a). This experiment provides the capability to evaluate the anode and cathode regions separately while exposed simultaneously under the same conditions. Additionally, surface-sensitive analytical methods were applied to map the brine chemistry/corrosion products that developed on the coupons post-exposure in the respective anodic and cathodic regions. The dual electrode cell also provides the capability to monitor the total charge consumed during the corrosion process through measurement of the current passed during exposure (Figure 26-b). The anode and cathode are set by an applied voltage differential (0.8 V). The current passed can then be compared to the surface electrolyte (Figure 27), as known droplet volumes and chemistries were deposited, and the dominant corrosion mechanisms can then be determined (Figure 28) displays the hypothesized corrosion pathways). Initial studies have shown the redistribution of the Mg^{2+} toward the cathode and the Cl^- toward the anode over time. Preliminary corrosion product identification has found the formation of iron oxides and iron hydroxides beneath the droplet on the anodic stainless steel and Mg-hydroxychlorides on the cathodic stainless steel (shown in the schematic in Figure 28). The consumption of Mg^{2+} and the precipitation of iron oxide product coincides with visible brine reduction (Figure 27) and may lead to total brine dry-out and shut off of the corrosion current, thus stifling pit growth, over exposure time. If corrosion products and thus corrosion pathways, can be determined along with the total current or charge passed for a given known brine exposure, the resultant corrosion damage for a specific environment could be predicted. In other words, the probability of a pit to grow or for a specific corrosion environment to stifle, may be determined from the known initial environment conditions. The knowledge of such conditions would further help refine the model assumptions, which currently account for a constant electrolyte brine that does not interact with either the environment (RH and T) nor the surface (or evolution of the brine due to corrosion) over time.

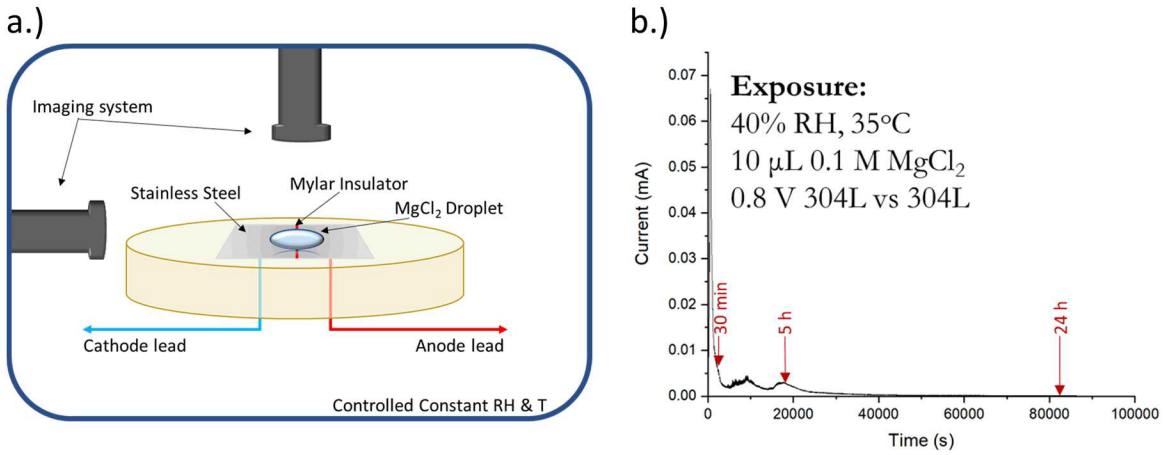

Figure 26. a.) Schematic of dual electrode exposure; and b.) current density vs. time for dual electrode exposure of 304L SS under a 0.1 M $MgCl_2$ 10 µL droplet for 24 h at 40% RH and 35°C.

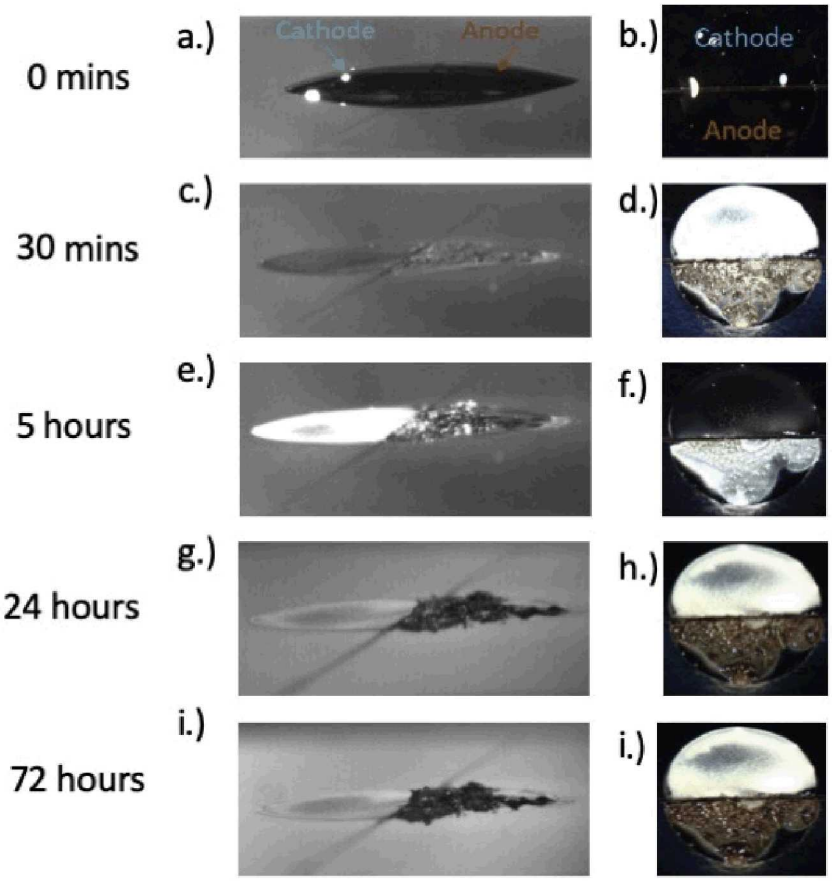

Figure 27. Time lapse images of the dual electrode exposure of 304L SS under a 0. 1 M $MgCl_2$ 10 µL droplet for 72 hours at 40% RH and 35° C, side view (a, c, e, g, i) with the cathode oriented to the left of the image and the anode to the right and top view (b, d, f, h, j) with the cathode oriented at the top and the anode at the bottom.

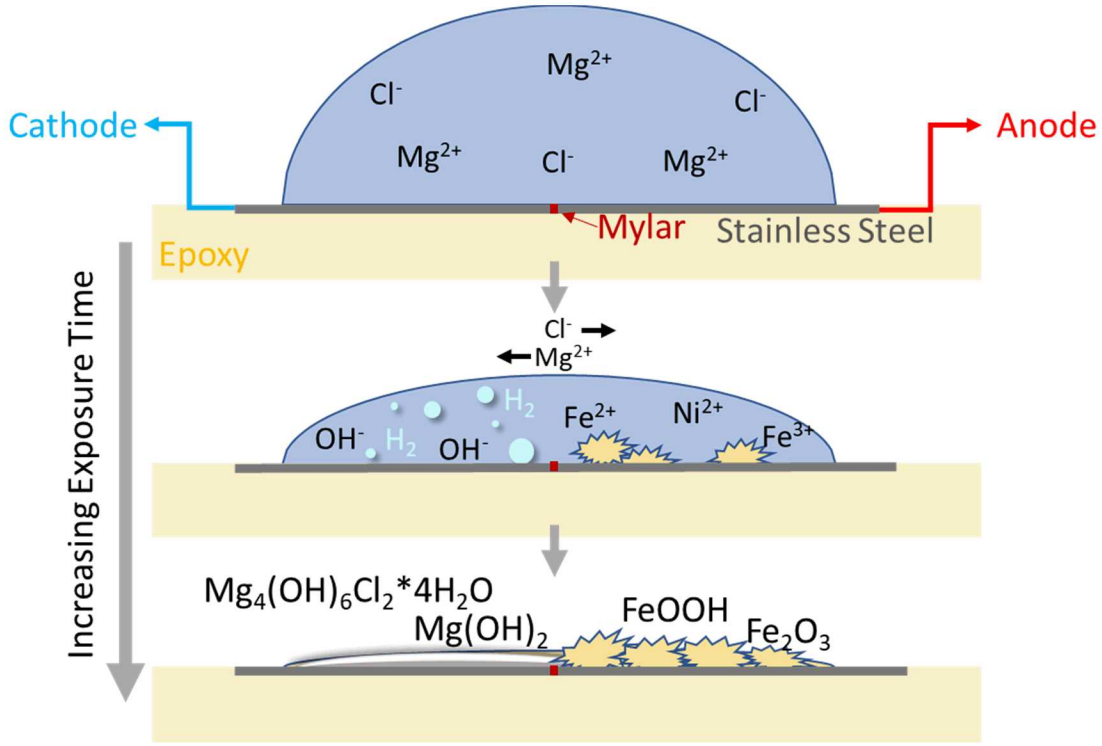

Figure 28. Schematic of brine evolution in an $MgCl_2$ droplet above the anode and cathode over exposure time at constant RH and T.

In FY20, we will continue to explore the relationship of initial brine conditions, brine evolution and corrosion product formation, total corrosion current, and corrosion damage to determine the corrosion pathways under the ISFSI relevant environments. Longer term dual electrode experiments with controlled chloride concentrations will be carried out to relate the corrosion rate and possible stifling with brine conditions. Determination of the brine evolution and these corrosion pathways will provide the necessary knowledge of the effects of the changing brine on corrosion to help enable validation and/or refinement of assumptions made in the maximum pit size model to better enhance the overall SCC cracking predictions.

4. Pitting: Relationship Between Corrosion Damage, Material, Mechanical Environment, and Environment

Work in FY18 implemented a series of experiments to quantify damage that evolves on austenitic stainless steels exposed to ISFSI-relevant fixed humidity and temperature conditions which were continued into FY19. These experiments were utilized to develop datasets on pit frequency and size distributions as a function of time, environment, and material. The following sections discuss the pertinence of the various environmental and material factors to pitting severity.

4.1 Effect of Stress

One possible significant environmental factor that may be deleterious to pitting damage is the residual stress present in the stainless steel. These stresses could be due to canister formation or welding of the canisters (either upon fabrication or repair). In previous literature studies, residual stresses have been observed to influence pitting behavior (Navai and Debbouz, 1999; Yang et al., 2003; de Abreu et al., 2017; Kadowaki et al., 2017; Nazarov et al., 2017). However, data relevant to ISFSI exposure conditions and possible residual stress levels present in dry storage canisters is lacking. This task addresses this by testing atmospheric exposures of 4-point bend bars to simulate the residual stress conditions expected in spent fuel canisters. The data generated here will be utilized to inform and benchmark statistical and deterministic SCC models under development at SNL, OSU and CSM.

Work in FY19 continued with additional analysis of the existing data and generation of larger statistical datasets for the stressed (4-point bend specimen) vs. unstressed (coupon) exposures in ISFSI-relevant atmospheric conditions. The primary focus was to determine the relative importance of stress as a parameter in pitting susceptibility of the canisters. Stressed 304L 4-point bend specimens along with unstressed coupons were loaded with artificial sea salt (400 $\mu g/m^2$) and exposed for 50 days to 35% RH and 50°C by CSM. Corrosion product was cleaned from these samples and surface profilometry used to analyze corrosion pits resultant from exposure. Initial results in FY18 of profilometry measurements suggested that stress alone did not influence pitting behavior under the conditions of the experiment. In FY19, the analysis areas were expanded to measure the entire stressed region of 16 mm x 200 mm (example scan in Figure 30-b), and an area of 16 mm x 24 mm of the unstressed coupon. Statistics on each of the pit characteristics, including roundness, area, pit depth distribution, and the ten deepest pits per region were measured by analyzing each pit individually (Figure 31). No difference in the pitting distributions was observable across the three different regions or with respect to the 304L coupon. However, the ten deepest pits were observed to increase in depth slightly from tensile to neutral to the compressive region, with a larger spread in depths for the stressed bar compared to the unstressed coupon. However, as there was no difference in the average depth across the regions explored, this may be an anomaly and needs further analysis to verify. These enhanced pitting statistics still suggest that stress alone, under the exposure conditions and stress levels examined here, did not influence greatly the pitting behavior of the 304L specimens.

To further explore the influence of stress on electrochemical pitting parameters, namely the open circuit potential (E_{ocp}), the pitting potential (E_{pit}), and passive current density (i_{pass}), additional electrochemical investigations were carried out. A microelectrochemical cell (Figure 32), with an exposed working area of about 380 μm^2 as compared to the traditional flat cell with a 1 cm^2 working area, was applied to measure electrochemical parameters while distinguishing the local stress-affected regions. This enabled electrochemical mapping of the stressed bar, which was categorized into three distinct zones across the 4-point bend sample; 1) tensile (from 1.5 to 4.5 mm perpendicular to the bending direction, along L1), 2) neutral (from 6.5 to 9.5 mm), and 3) compressive (from 11.5 mm to 14.5mm), based on the digital image correlation stress maps produced by CSM in Figure 29-a-c. For the microelectrochemical cell measurements, a similar unexposed 304L bar, polished and stressed in the same fashion as the exposed sample was studied. These regions of the stressed sample were compared to similar microelectrochemical

cell measurements performed on unstressed regions under the same conditions. In addition to testing in the brine concentration of the atmospheric exposure environment (provided in Table 12), the combined effects of chloride concentration and stress were explored. Anodic polarizations were performed to determine the electrochemical parameters. In low chloride concentrations, no observable difference in pitting susceptibility is observable (Figure 33). At higher chloride concentrations (1 M NaCl) a difference in passive current density, indicative of the susceptibility of the material, was observed with the lowest i_{pass} in the compressive region, then neutral region, then highest in the tensile region (Figure 33-b). In the surrogate brine of interest (56% $MgCl_2$ determined from Table 12), again there was not a discernable difference in the anodic polarizations scans nor electrochemical parameters across the varied stress regions (Figure 33-c). This may be important to canister sites, as this highlights that the influence of stress could be combined with or dependent upon the exposure environment. Additionally, ellipsometry measurements were applied to observe possible localized effects of stress on the passive oxide layer. The passive film was measured to be 6 nm with no distinct differences across the stressed regions, therefore stress-affected breakdown of the passive layer did not likely occur under these conditions.

Further examination of the stressed vs unstressed 304L specimens was carried out through scanning electron microscopy. No quantitative nor qualitative discernible differences were observed across the varied stressed regions, nor between the stressed vs. unstressed 304L. However, distinct features of the pits that formed were observed across both samples, examples shown in Figure 35. EBSD analysis in Figure 36 (higher resolution micrographs of each region) and Figure 37 (sample montage) displays no obvious differences across the sample in terms of residual stresses on the microstructural features that might affect pit initiation or growth, there is no evidence of near surface strain induced martensite at low or high magnification across the different regions. Additionally, the FCC versus BCC (martensite or delta ferrite) distribution appears unaffected by stresses induced on the 4-point bend bar, Figure 36– g, h, i, and Figure 37-c.

Work will continue into FY20 with expanded analysis of additional 4-point bend (stressed)samples. FY19 experiments were carried out for one exposure environment. Also, in FY19, CSM has conducted additional experiments across a wider parameter space, including time of exposure, salt deposition density, surface finish, stress load, material properties (weld and/or sensitization, rolling direction), and laboratory vs. field environment. FY20 will focus on similar analysis of this larger sample set to gain insight into the possible combined effect/ interaction of residual stress and exposure environment on pitting. The initial information gained in FY18 and FY19 serves as basis to study the pitting and SCC behavior of these more complex weld zone regions where residual stresses are present, building an electrochemical description of weld zone regions on the canister for prediction of pitting and SCC susceptible zones and informing/updating the SNL SCC model.

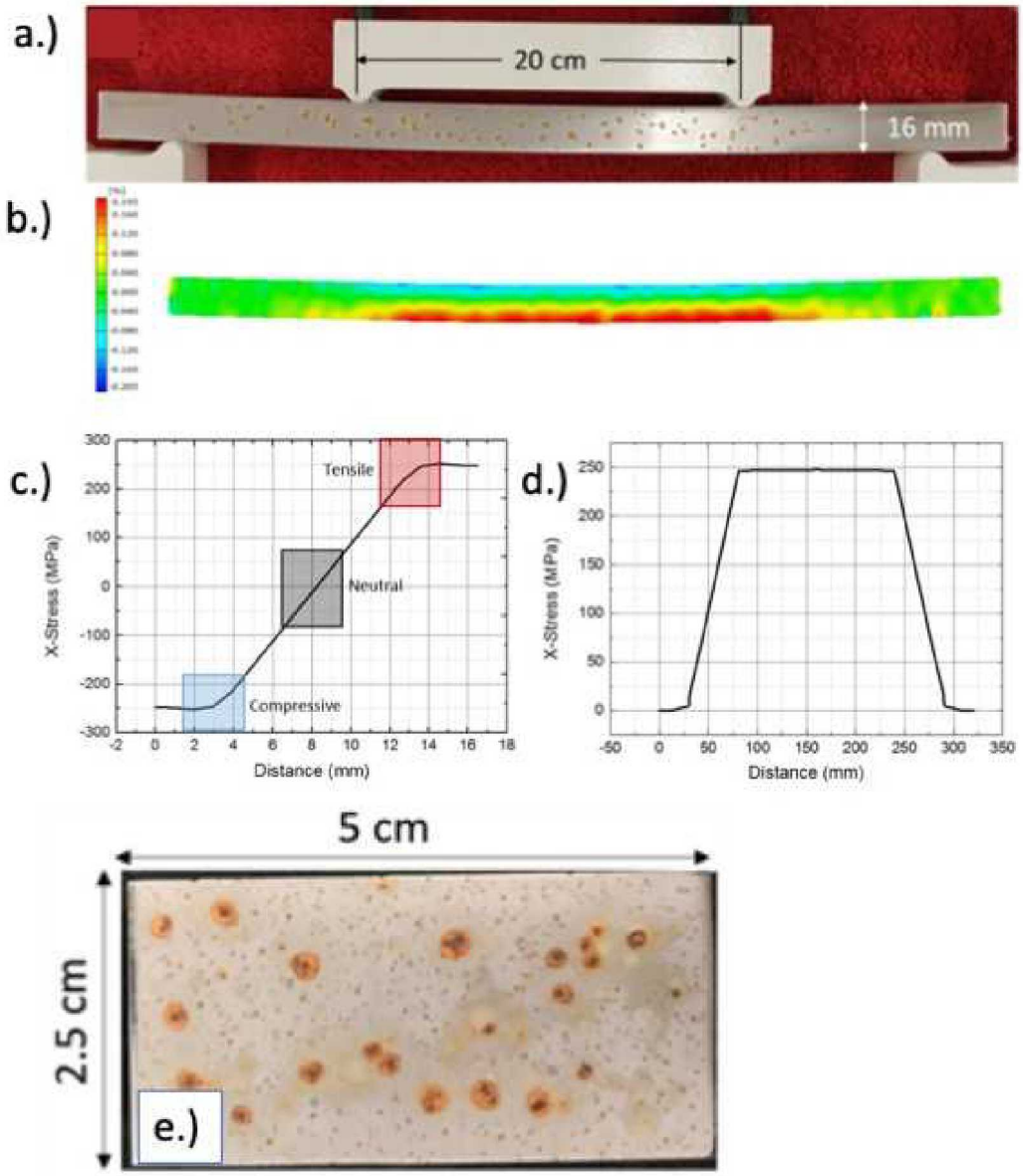

Figure 29. a.) Stressed 304L 4-point bend specimen; b.) digital image correlation stress map of the same specimen and profiles of c.) the cross-section and d.) the specimen length; and e.), unstressed coupon after depositing 400 µg/cm^2 sea-salt and exposing for 50 days at 50°C and 35% RH.

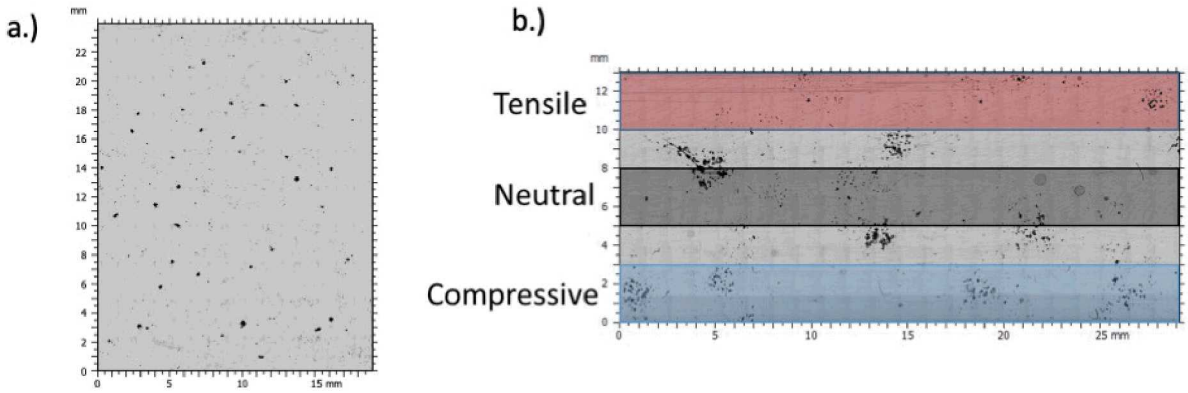

Figure 30. Images of representative analyzed areas on a cleaned a.) unstressed 304L coupon, and b.) a section of the stressed 4-point bend sample b.) after exposure with 400 µg/cm^2 sea salt at 50°C and 35% RH.

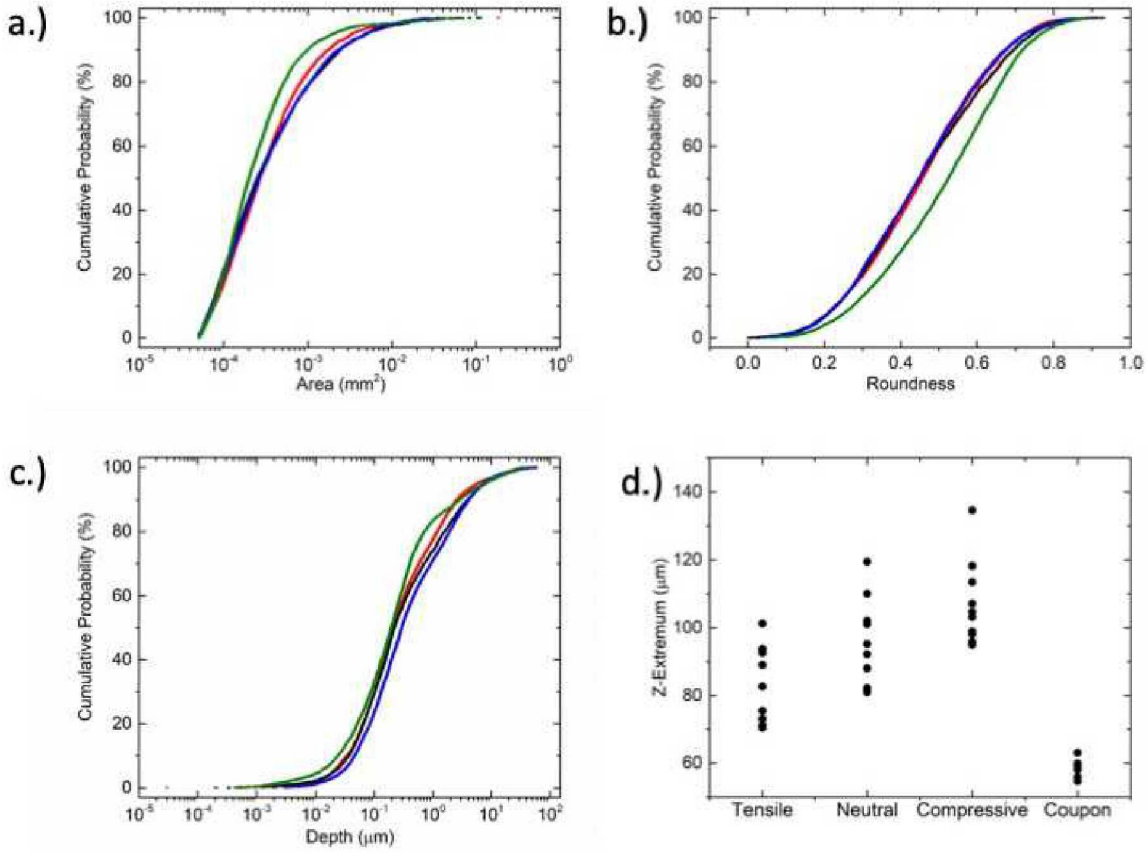

Figure 31. Post exposure profilometry distributions on the 304L 4 pt bend bar of the tensile (red), neutral (black), and compressive (blue) regions vs an unstressed (green) 304L coupon for the pitting statistics collected of a.) area, b.) roundness, c.) depth, and d.) 10 deepest pits per region.

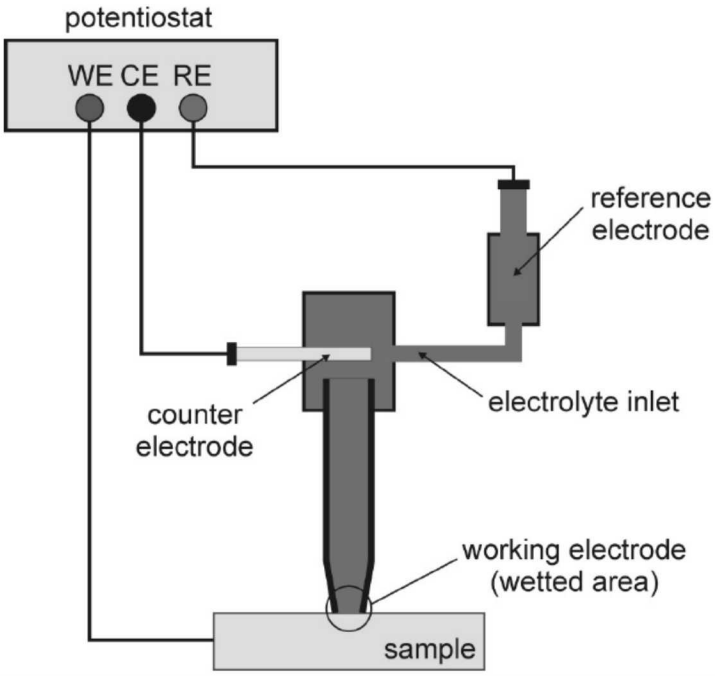

Figure 32. Schematic of microelectrochemical cell.

Table 12. Brine concentration calculated for 50 ºC, 34.9 % RH

Salt	Mass added, g
NaCl	6. 0517
KCl	2.5982
$MgCl_2:6H_2O$	1179.1101
$CaCl_2$ (anhydrous)	0.4538
$MgSO_4$	2.8845
$MgCO_3$	7.9663
$MgBr_2:6H_2O$	29.4986
H_3BO_3	6.4246
H_2O	338.463

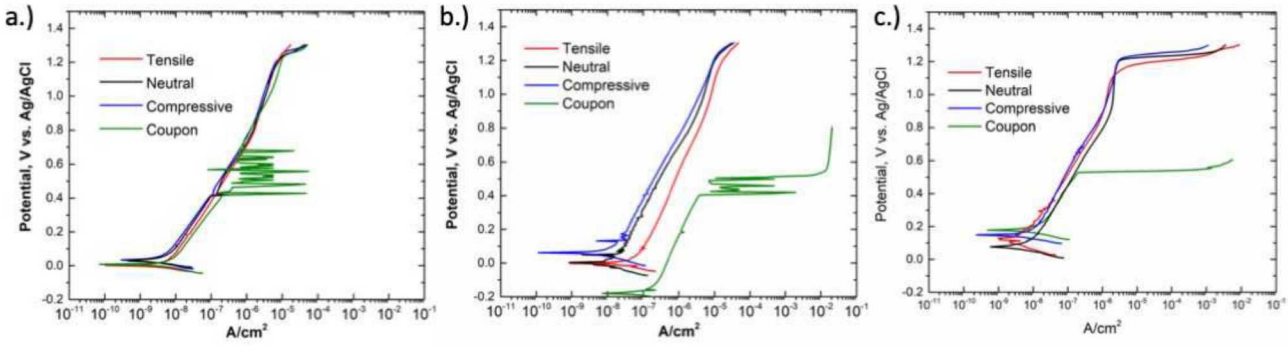

Figure 33. Microelectrochemical cell anodic scans of 304L 4-pt bend bar vs 304L coupons in a) 0.1 M NaCl, b) 1 M NaCl, and c) 56% $MgCl_2$ brine determined for equivalent conditions of seawater at 34.9 % RH and 50°C (Table 12).

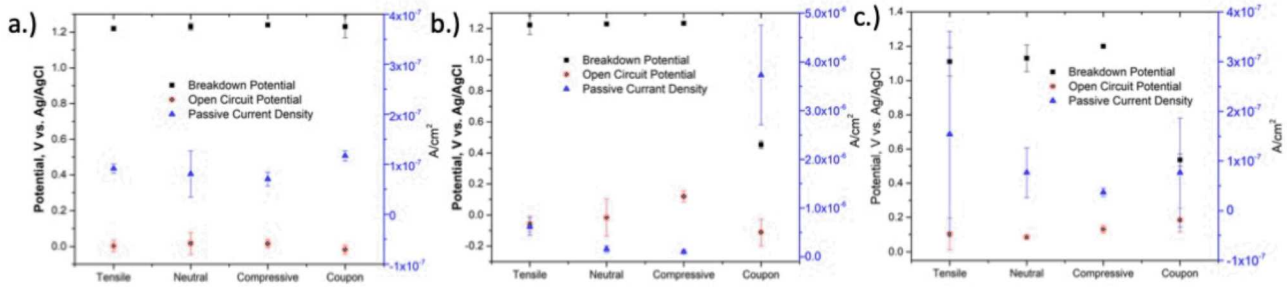

Figure 34. Electrochemical parameters as determined by microelectrochemical anodic polarization for a.) 0.1 M, b.) 1 M NaCl, and c.) 56% $MgCl_2$ solution for the 4 pt bend bar regions vs the unstressed 304L SS.

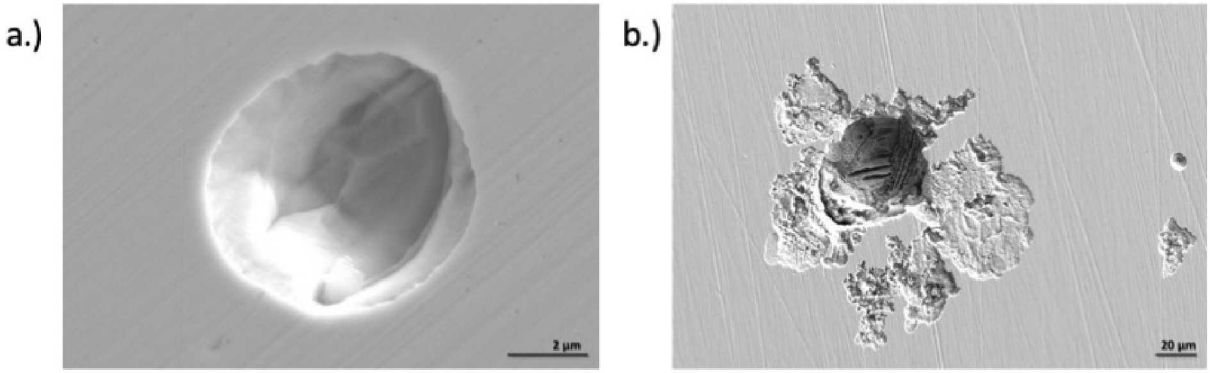

Figure 35. Representative SEM micrographs of typical pits observed across the stressed and unstressed 304L specimens post exposure and corrosion product removal. a.) Typical hemispherical pit attack and b.) larger, non-hemispherical pit with microstructurally influenced corrosion attack.

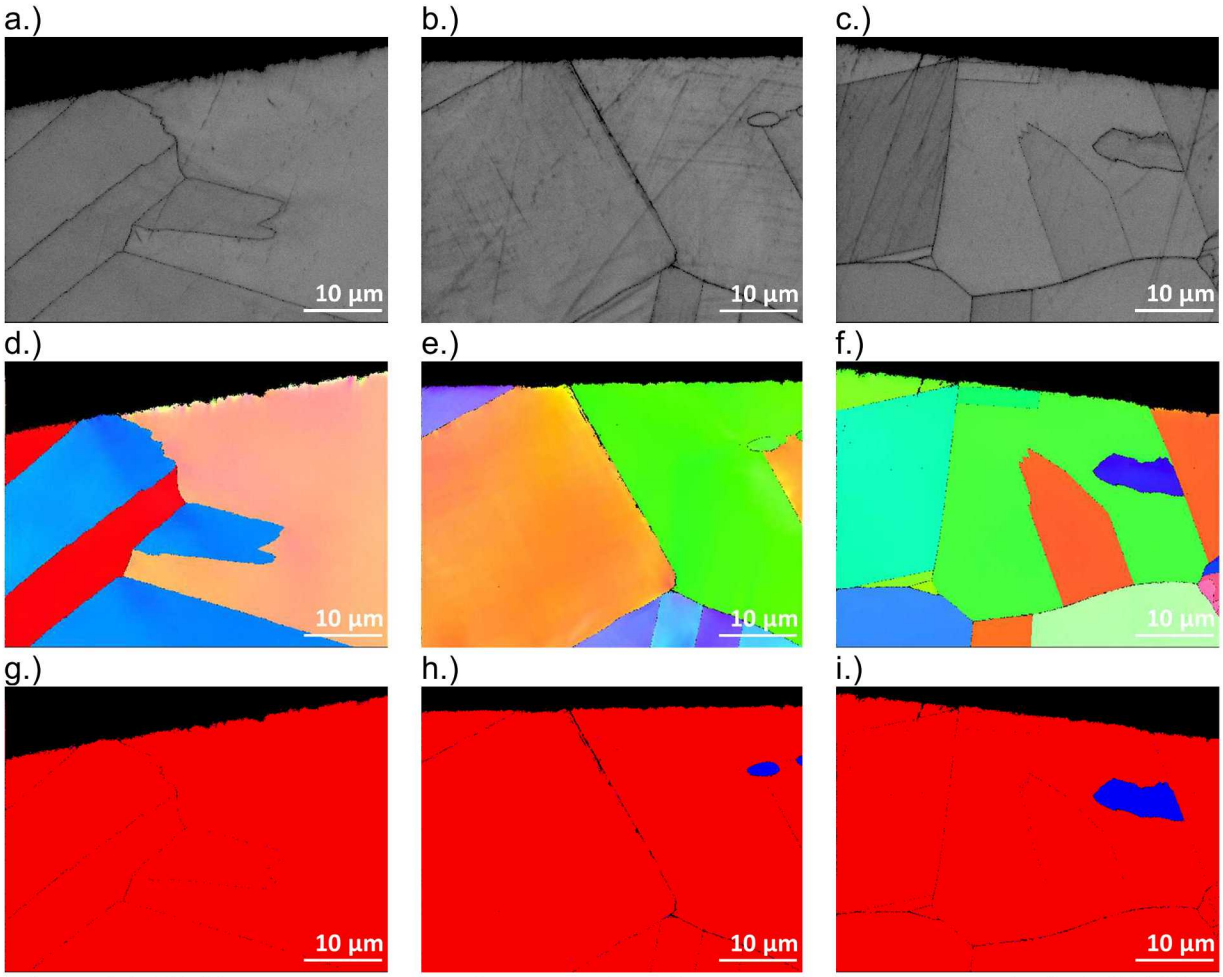

Figure 36. EBSD post-exposure band contrast, IPF X map, and phase contrast (red – FCC, blue – BCC), of cross sections of the tensile (a, d, and g); neutral (b, e, and h); compressive (c, f, and i) regions of the 4-pt bend bar, respectively.

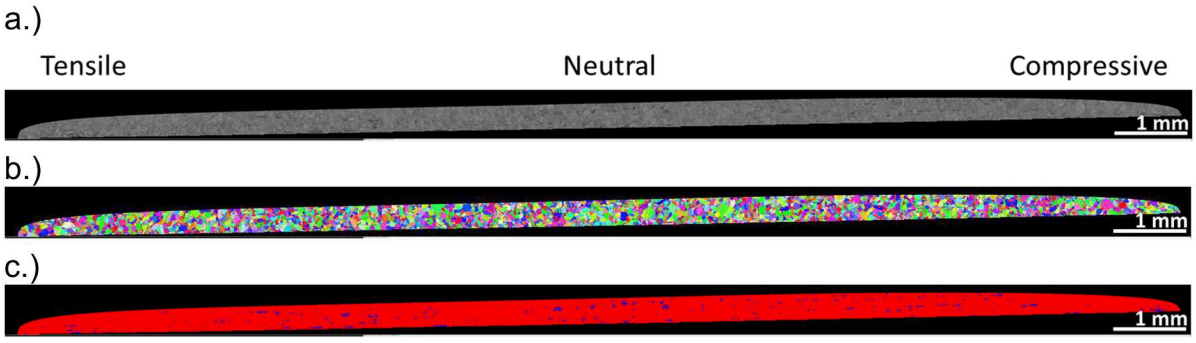

Figure 37. EBSD post-exposure cross section of the entire 4-pt bend bar of a.) band contrast, b.) IPF X map, and c.) phase contrast (red – FCC, blue – BCC)

4.2 Effect of Surface Finish and Environment (RH, T, Salt Load)

In FY18, a series of experiments were initiated to quantify damage that evolves on austenitic stainless steels exposed to ISFSI-relevant fixed humidity and temperature conditions; these samples were subsequently analyzed in FY19. In addition to the previous data collected on the influence of residual stress on pitting, the exposures described here evaluated the influence of material surface finish and exposure environment (salt load, T and RH) on pitting. This data will also be utilized to inform and benchmark the statistical and deterministic SCC models.

304L coupons were loaded with ASTM D1141 artificial sea salt and placed in environmental chambers for exposure at two RH conditions and an elevated temperature (35°C) for up to two years. Sets of coupons were removed periodically to measure corrosion damage using optical profilometry. The profilometry was carried out with Prof. Jenifer Locke and The Ohio State University. The environmental conditions relevant to expected canister conditions are shown in Table 13**;** the selected conditions are highlighted in green, and represent two plausible extremes of expected deliquesced brines. These are two humidity conditions where potentially severe pitting is expected: 40% RH is slightly above the deliquescence RH for magnesium chloride, resulting in a highly concentrated but small volume of magnesium-chloride rich brine, while at 75% RH, the seawater brine is comprised of a much larger volume of near-saturated NaCl (~6 M). Artificial sea-salt loadings of 10 and 300 µg/cm^2 were chosen for this test, representing values within the lower and upper bounds reportedly measured on canisters or surrogate surfaces in marine conditions (EPRI, 2015).

Table 13. Expected Corrosive Environmental Conditions on Canister Surfaces

%RH	Temperature (°C)				
75	35				
70	35				
65	35				
60	35				
55	35	40			
50	35	40			
45	35	40	45		
40	35	40	45		
35	35	40	45	50	
30	35	40	45	50	

Rectangular coupons measuring 1" x 2" with two surface finishes were examined, a mirror finish (R_a = 0.05 µm) and a 120 grit "mill" rough finish (R_a = 2.8 µm). These two surface finishes were selected to represent two extreme bounds of roughness expected on the canisters. Surface finish is expected to have considerable impact on pitting kinetics and size distributions (Burstein and Pistorius, 1995; Moayed et al., 2003). Rougher surfaces are generally more prone to pit initiation, which has been attributed to occluded regions in the ground surface and, possibly, localized residual stress/strain that can act as pit initiators.

The experimental approach utilized a novel, high-throughput sample preparation and analysis methodology. An inkjet printing technique deposited controlled amounts of ASTM D1141, artificial seawater (ASTM International, 2008) particles on the sample surfaces (Schindelholz and Kelly, 2010)**.** The salt loading pattern on the coupons for two different loading densities is shown in Figure 38. Corrosion damage morphology (e.g. pitting) was analyzed using a white light profilometer at OSU to create 3D profiles of the exposed coupons. The profiles were analyzed using a commercial software package capable of automatic detection and measuring of individual pit features.

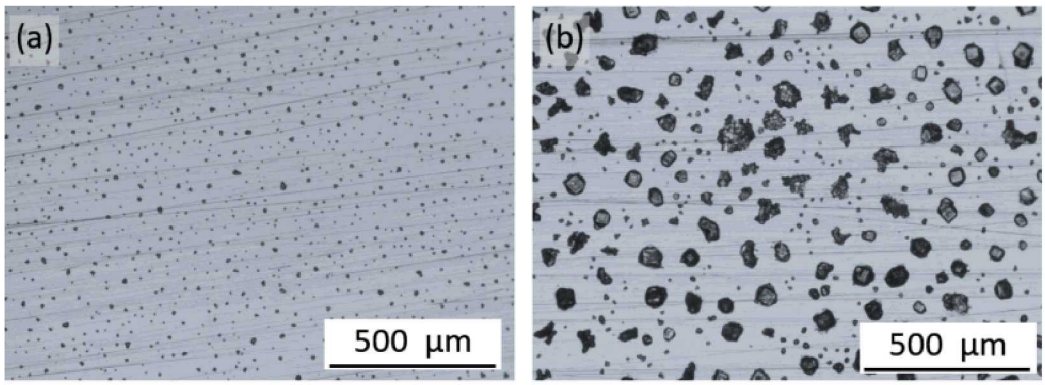

Figure 38 Sea salt particles after printing a.) 10 µg/cm^2 and b.) 300 µg/cm^2 on mirror finish 304L coupons.

The experimental matrix is given in Table 14. The values given for each time represent the number of replicate coupons for each surface finish pulled from the humidity chambers for analysis. Extra samples were included at 6 months and 18 months for leaching and chemical analysis to evaluate potential changes in the soluble salt compositions due to the atmospheric exchange reactions or corrosion reactions during the exposure period. To date, all samples have been pulled, and analysis has been carried out for samples up to 18 months of exposure. Analysis of the 2-year samples is underway and will be completed in Q1 of FY20.

Table 14. Experimental Matrix for Pit Characterization Experiments

Environment	Salt Load (µg/cm^2)	1 wk	2 wk	1 mo.	6 mo.	12 mo.	18 mo.	24 mo.
35°C, 75%RH	10	7	7	7	14	7	14	7
35°C, 75%RH	300	7	7	7	14	7	14	7
35°C, 40%RH	10	7	7	7	14	7	14	7
35°C, 40%RH	300	7	7	7	14	7	14	7

After exposure and optical imaging, the rust was removed using a nitric acid solution following the ASTM G-1 cleaning procedure and pitting damage was measured using a profilometer. An example of the analysis procedure is given Appendix A. Efforts in FY19 focused on an enhanced analysis of the pitting data sets. The initial analysis for the ground coupons has been published in the manuscript in Appendix A. However, the following provides a detailed description of the path forward with regards to the remainder of the data, with expansion to the mirror polished samples and plans for future analysis and exposures.

Pitting statistics were developed for exposures from 1 week to 18 months using an optical profilometer, with images taken from the analysis patterns shown in Figure 39. Sample pattern “a” was applied for the studies presented in Appendix A, however, results presented here applied the sampling methodology in “b”, which measured the same area with enhanced detection capability for pitting. This pattern was applied to achieve results for the mirror samples as pits were undetected with the first analysis method. However, even with the enhanced profilometry analysis, no pits were observed on any of the coupons polished to a mirror finish that were exposed. For the samples ground to 120 grit, as can be seen in Figure 40, corrosion damage, in terms of total volume lost, and the number of pits across time, both reach limiting values at longer exposure times, greater than about 56 weeks. This initial trend may indicate a possible stifling of pitting over exposure time, however further analysis is necessary to validate this.

Profilometry measurements of 2 year exposure coupons from the same exposure set will take place in FY 20 to further validate this trend.

In addition to statistical analysis of pitting morphology from profilometry measurements, SEM has been applied to visually characterize typically observable pit morphologies. Again, no pits were found on all mirror polished coupons exposed up to 18 months. Across both the 76 and 40 % RH exposures for the 120 grit finish coupons, both individual and coalesced pits were observed. Two general pitting morphologies were seen, smooth, hemispherical-like attack on the 76% RH exposures, or irregular attack with microstructural etching in hatched patterns on the 40% RH exposures. Micro-cracks associated with pits were only observed in the 40 % RH exposures which exhibited the irregular pit morphologies Figure 41. Differences in the pitting morphologies are related to the differences in the electrolyte or brine at the two exposure RHs. As the brine concentration and volume change based on the exposure RH, the cathodic kinetics, which can limit or control pit growth, vary. At the high RH, 76%, the brine volume is larger and the chemistry is dominated by a high NaCl concentration, whereas at the 40% RH, the brine dries out, therefore the droplet volume shrinks, some salts precipitate out, and the brine chemistry is dominated by $MgCl_2$. These differences lead to changes in the cathodic kinetics, as the cathode area is affected by brine volume, the transport can be affected by an ohmic drop (as salt particles precipitate out and physically block transport), and while the charge transfer kinetics remain similar, the diffusion controlled kinetics change as O_2 concentration and diffusivity vary in the different brine chemistries. These changes in parameters that affect the available cathodic current density may give rise to the variance in pit morphology across the different exposure RHs. In FY19, a small set of samples fully immersed in brine solutions at the same T (35°C) and for a time period of 47 days was carried out to explore the effects of cathode area limitation. As in full immersion, the cathode area is essentially unlimited compared to the drop, this allows for normalization of the cathode area in the different brines. However, the difference in pit morphology was still observed, where smooth hemispherical pits were found in the brine composition equivalent of the 76% RH exposure, and microstructurally attacked pits were observed in the brine equivalent of the 40 %RH exposure (Figure 42). Work in FY20 will continue to evaluate the influence of cathodic kinetics, specifically those that are affected by RH and environment, on the subsequent pit morphology. Continuation of the full immersion experiments in simulated and surrogate brines has been initiated to further determine the influence of brine chemistry on the pit morphology.

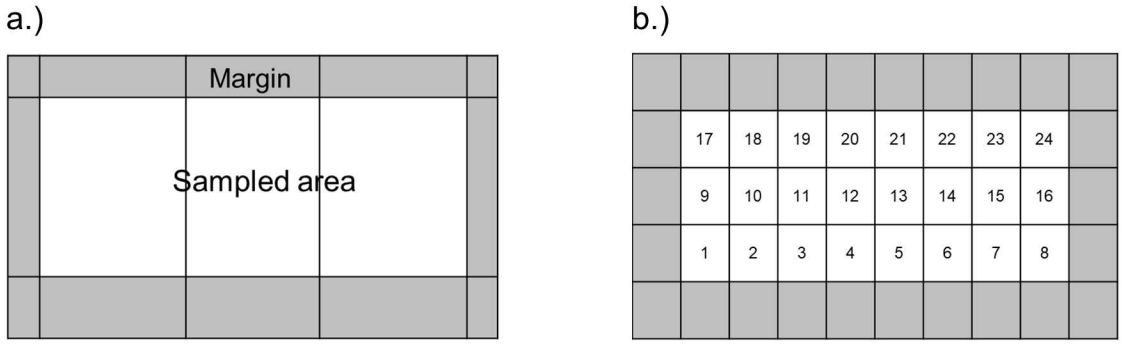

Figure 39. Samples analysis patterns for data collected for a.) Appendix A JECS paper: 3 equally-spaced areas 12 mm × 12 mm sampled, margin of at least 5 mm away from the edge, and b.) current analysis: 24 equally-spaced area of 5 mm × 5 mm sampled, labeled 1-24, margin of 5 mm from the edge.

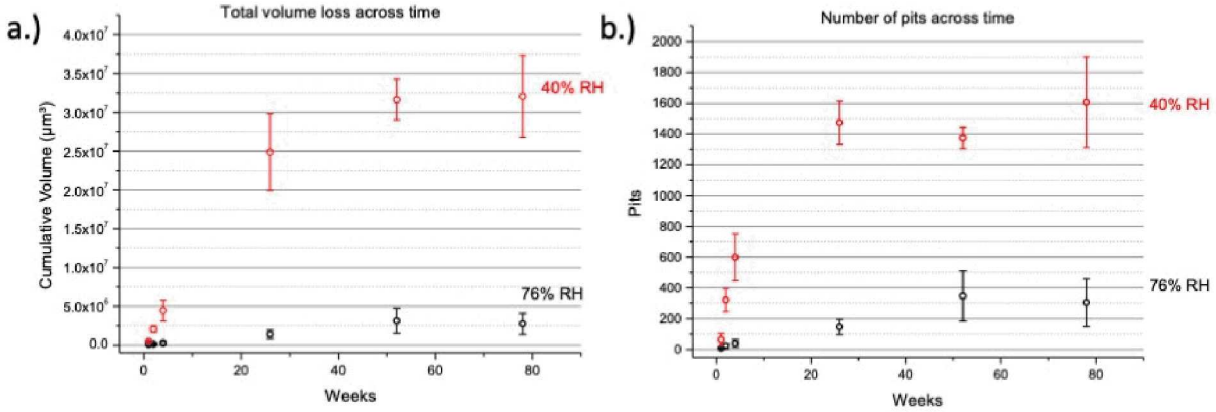

Figure 40. a.) Volume loss versus time and b.) number of pits versus time for 304L SS coupons with 300 µg/cm^2 artificial seawater exposed at 76%(black) and 40% (red) RH at 35^{o}C for time periods from 1 week to 18 months.

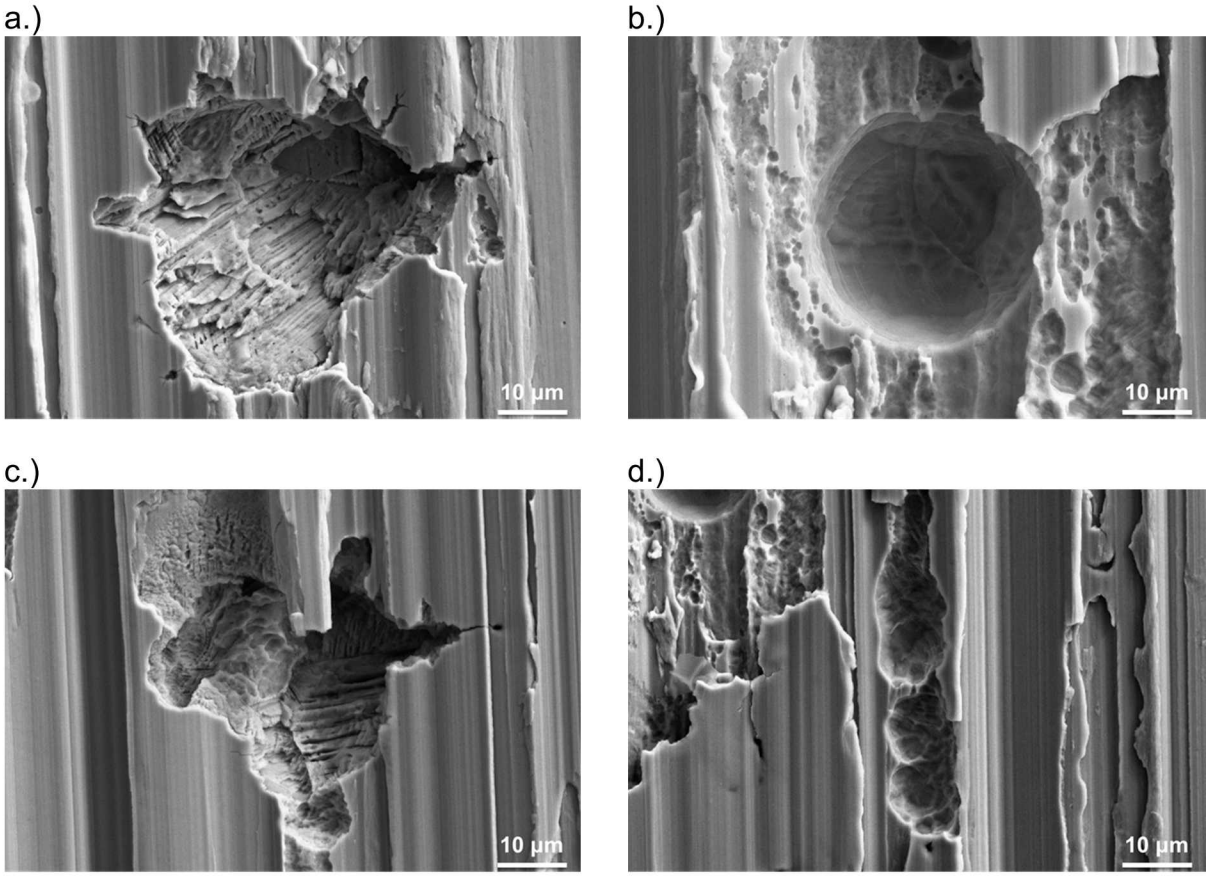

Figure 41. Typical pitting morphologies (individual – a & b and coalesced – c & d) for 304 L SS exposed for 2 weeks with 300 µg/cm^2 artificial seawater at 35 ^{o}C at a & c) 40% and b & d) 76% RH.

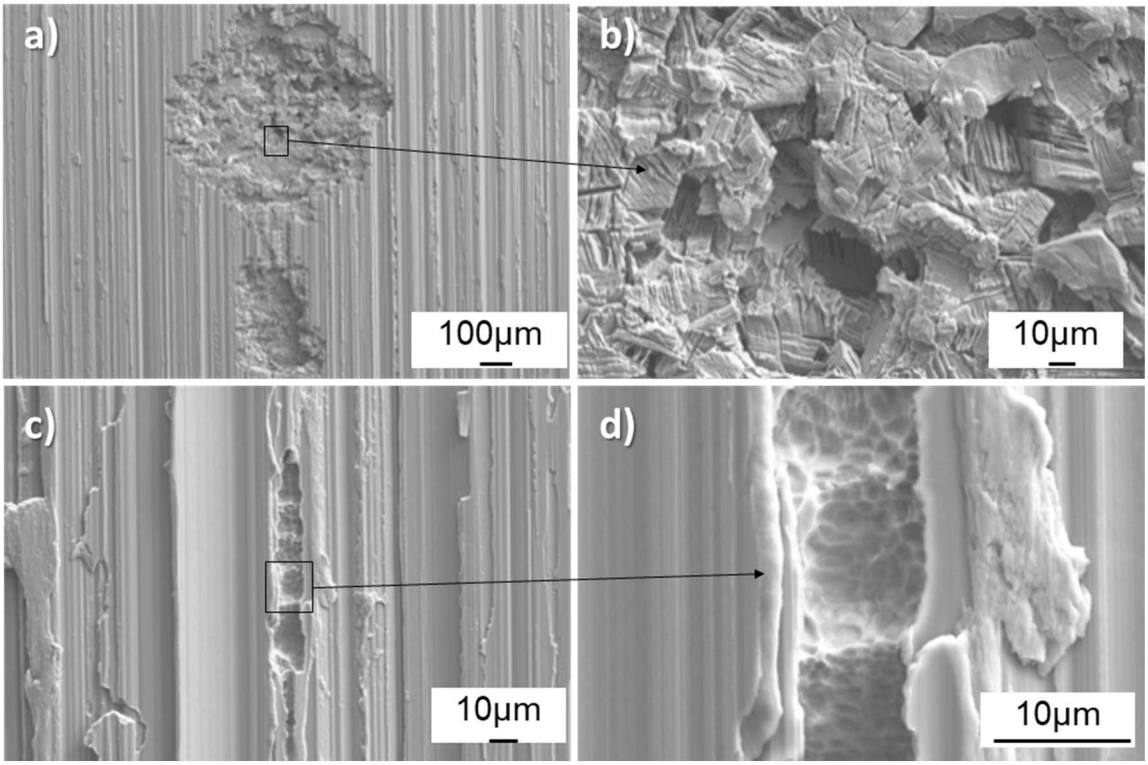

Figure 42. Pitting morphologies observed for 304 L SS exposed for 47 days full immersion in artificial seawater at 35°C at an equivalent concentration to a & b) 40 and c & d) 76% RH.

Efforts in FY20 will continue to pursue the creation and analysis of datasets for pitting statistics in ISFSI exposure relevant conditions. In Q1 we will expand the matrix to include increased temperature extremes, for example 50°C, and the influence of temperature on mirror polished surface pitting. Additionally, interest will be paid to the influence of salt coverage/ cathode area and the resultant corrosion damage. As observed from this dataset, RH, and thus cathode electrolyte, play a large role in pit morphology. FY20 will focus on exploring the relationship between electrolyte coverage, size, amount, and the resultant pit morphology to better develop pitting statistics that can inform cracking model based also on the influence or possible significance of pit geometry. In addition to the full immersion experiments mentioned, screening testing of influential parameters (size, deposition density, patterning, etc.) will be carried out on a smaller scale, with individual tests in the electrochemical microprobe station. The determined most deleterious parameters from these tests will be used to inform the development of large-scale coupon exposures with the most pertinent factors for pitting damage in order to develop a more valuable statistical pitting data sets for ISFSI exposure conditions. In addition to salt coverage/ cathode area, large scale coupon exposure will be initiated under cyclic humidity and temperature conditions to replicate the effects of diurnal variation in ambient weather. With regard to the latter, there is no information on how cyclic conditions expected on the canisters impact pitting kinetics. These data will be used to directly test the SNL SCC model which predicts maximum pit size over time and they will be used to develop statistical models. Additional statistics we are collecting pertain to pit morphology and include pit volume and principle curvature. The latter descriptor could be utilized to determine the probability of developing a pit geometry capable creating local stress concentrations expected to initiate cracking, as will be discussed in the next section. The resulting datasets and analysis

will be distributed to our collaborators to inform and benchmark statistical and semi-deterministic canister cracking models currently under development at SNL, CSM and OSU.

4.3 Pit-to-Crack Transition

In many susceptible alloys, corrosion pits are commonly observed as initiation sites for SCC cracks (see, for example Figure 43). Existing models for pit-to-crack transition relate pit size and shape to crack initiation through calculated stress intensity factors (Kondo, 1989; Turnbull et al., 2009; Horner et al., 2011). If the local stress intensity at the surface of a pit exceeds an empirically-determined SCC threshold stress (i.e., $K > K_{ISCC}$), a crack is assumed to initiate from that pit. The relevance of this relationship and accessible limits of these models, in general, are unknown for storage canister conditions. Furthermore, the validity of the assumption that general pit shape and size control pit-to-crack transition is not well understood. Other features, such as finer topography within pits (that could serve as stress concentrators) or microstructure could have a more commanding role in controlling pit-to-crack transition (Donahue and Burns, 2016). The aim of this work is to identify important features controlling pit-to-crack transition. Parameters of interest include pit shape, corrosion morphology (e.g. single versus satellite pits) and microstructure.

Our approach to understanding the controlling features for pit-to-crack transition and their prevalence under ISFSI-relevant conditions is to examine the cracking initiation behavior of salt-loaded 304L tensile test specimens of the similar material as the coupon samples discussed in Section 4 that are exposed to same environmental conditions (salt load, T, and RH) and under load. During the period of exposure, the specimens are held at a constant load with high R ripple fatigue load cycles that are periodically introduced. The ripple fatigue technique is meant to introduce marker bands on the fracture surface along the crack front as it grows. These bands can be followed, like tree rings, back to the point of crack initiation upon post-test SEM fractography examination (Donahue and Burns, 2016). We anticipate that this approach will help identify corrosion damage and microstructural features that act as crack initiation sites. Additional post-mortem characterization tools at SNL, such as microCT and serial sectioning, will be utilized to further characterize these specimens. Additionally, cracking activity during the tests are monitored via a direct current potential drop method to detect crack initiation events. Further experiments will be carried out where controlled pits are created in tensile specimens and then tested to refine these rankings. Assuming similar behavior between the tensile specimens and the exposed coupons, we will develop statistics on prevalence of these initiation-susceptible features with respect to exposure time and environment. These statistics could be used to validate the current pit-to-crack transition models based on stress intensity factor or be used in their place as input datasets for stochastic SCC models being developed by SNL, CSM and OSU. This task is being undertaken in collaboration with OSU.

Efforts in FY19 have focused on installing and bringing online two servo hydraulic load frames for testing, completion of salt-loaded tensile test exposures, and performing an initial load test on a specimen. Two hydraulic 22 kN load frames with direct current potential drop (DCPD) systems purchased at the end of FY18 were installed and calibrated in the corrosion labs at Sandia in FY19 Q1. Custom atmospheric environmental test chambers designed and constructed at OSU were also installed on the load frames. The chambers were fitted with temperature and humidity control systems. These systems allow for rigorous control of humidity within the range of <1 to 98% RH with ±0.1% precision and temperature from ambient to 80 ±0.1° C.

To date, salt-loaded tensile bars have been exposed in humidity chambers to the conditions given in Table 13 for up to 1 year. These specimens were not mechanically loaded when exposed and serve to provide baseline information on the pit morphology and cracking behavior of the unstressed material. Characterization of the corrosion attack morphology on these exposed samples using the approach described in Section 4 will be carried out in FY20. A subset of these tensile samples exposed in the humidity chambers are scheduled to be further exposed in the load frames under stress and under the same environmental conditions that they had seen in the humidity chamber. These crack initiation tests

will follow the general experimental approach outlined above and provide the preliminary data on crack initiation features.

An initial load test of one of the tensile bars exposed to the humidity chamber was carried out in FY18 and is currently undergoing post-mortem analysis. In this test, a salt-loaded tensile bar that was exposed in the humidity chamber at 35 °C, 40% RH for 6 months was placed under a load stress 1.2 times nominal yield strength in the same environmental conditions in the servo hydraulic frame. The sample was exposed under load for 6 months and monitored using a two-wire DCPD setup on one of the salt deposited faces. No change in potential drop nor load displacement was detected during the test. In other words, any cracking that may have occurred was below measurement resolution. After the test, rust was removed from the sample using nitric acid per ASTM G1 and it was examined via optical and electron microscopy. Corrosion damage morphology was similar in nature to the coupon tests described in Section 4 with cracks found in association with some of the pits (Figure 44). It is unclear whether these cracks formed during the humidity chamber exposure and prior to placing the sample under load. Furthermore, this preliminary examination provides little information on preferential initiation sites and the extent of crack propagation into the bulk material. Further post-mortem examination of this sample in conjunction with the unloaded humidity chamber exposed samples in FY20, including fractography, is planned to help elucidate these issues.

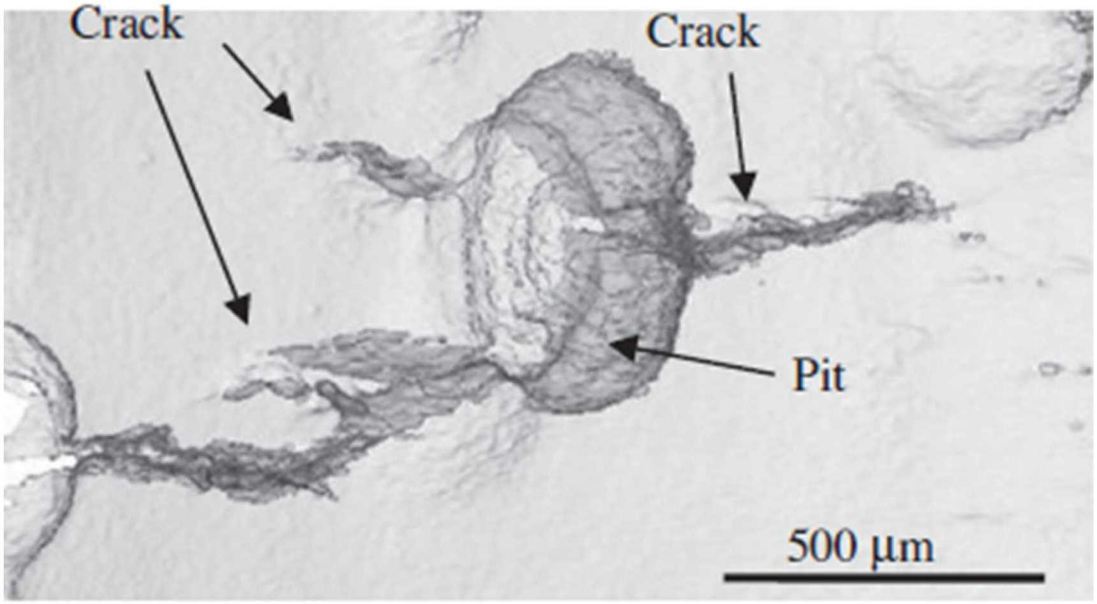

Figure 43. 3-D tomographic reconstruction of cracks emanating from a pit after exposure and mechanical loading of a 3 NiCrMoV disc. From (Horner et al., 2011).

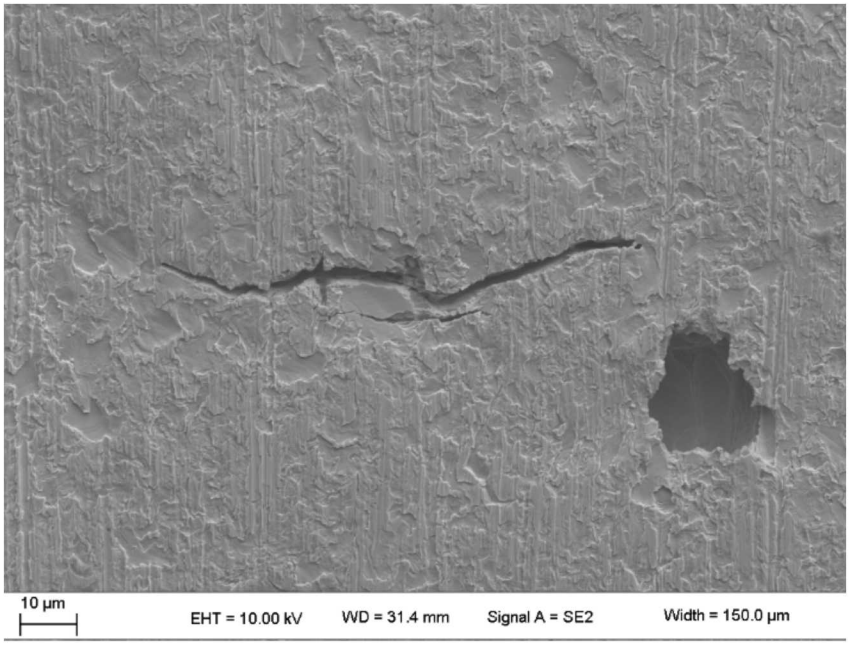

Figure 44. Detail of a crack associated with a pit on the shank surface of a 304L tensile test specimen that had been exposed under tensile load to 40% RH, 35 °C for 6 months. The test specimen was coated with 300 ug/cm^2 artificial sea salt prior to exposure. The load direction was vertical (up and down) with respect to the SEM image orientation.

This page is intentionally left blank.

5. SCC Crack Growth

One of the primary questions that we seek to answer with this overall research is how SCC susceptibility is affected by the atmospheric exposure environment. Specifically, how is the crack growth rate $\left(\frac{da}{dt}\right)$ and threshold stress intensity for SCC (K_{ISCC}) effected by ISFSI-relevant atmospheric conditions? As there is currently very limited data in the literature on crack growth rates (CGR) for SS304L, let alone atmospheric cracking data pertinent to ISFSI sites, there remains much work to pursue in this area. One of the main goals of the Sandia-led effort in this is to determine the relationship between the environmental conditions, the cathodic kinetics, and the subsequent control of the crack initiation and crack growth rate. Knowledge of this will enable both better predictions of SCC cracking as well as determination of the deleterious factors and possible enhancements for mitigation strategies.

5.1 Installation of load frames and initiation of testing

In FY19, we have established a contract to procure 4 electromechanical load frames in addition to the two servo-hydraulic load frames currently in use. The purpose of this new procurement is for the direct study of crack growth rates in atmospheric environments relevant to ISFSI exposure conditions. The collaboration has been established with DNV-GL, and the first objective is to build and supply SNL with four custom load frame systems for the study of chloride-induced stress corrosion cracking. Two of these frames are to be delivered and installed in Q1 of FY20, while the second two will be installed in Q2 of FY20. DNV-GL will aid in this by providing extensive training and by working with SNL to generate SCC CGR data on type 304L SS in concentrated brine solutions simulating the chemistry of near-marine atmospheric environments. This collaboration will help SNL to develop a specimen design and methodology for measuring CGR of 304L SS in both immersed and atmospheric laboratory simulated marine conditions; and generate CGR data for 304L SS immersed in seawater brine simulants using the developed specimen design and methodology. The specimens will be designed and optimized to understand the specific influences of atmospheric environments on CGR, specifically the interaction of the environment and the role it plays in governing the cathode area and how this in turn affects the CGR.

5.2 SCC Initiation and Growth Rates ($MgCl_2$ vs NaCl)

In FY20, we plan to generate CGR data for 304L SS immersed in seawater brine simulants ($MgCl_2$ and NaCl) using the specimen design developed in collaboration with DNV-GL. This will include CGR measurements in at least four plausible extremes of expected brine environment on the canister where SCC could be considered most aggressive (e.g., high, low temp; high, low concentration). We also plan to include exploration of electrochemical potential control. With these full immersion experiments of CGR we will develop a method for immersed CGR experiments that can also be applied to atmospheric conditions including a pre-crack procedure, determination of frequency and K threshold values and the ability to perform displacement control and K-control testing. Additionally, various sample designs, including both long and short cracks, pre-notched and ground off notch, will be tested to establish both validity of the novel sample geometries and determine the best method for atmospheric SCC testing.

This page is intentionally left blank.

6. Big Plate Samples and 4-point Bend Test

Starting in FY18, we began studies to evaluate the effect of material characteristics and mechanical environment (microstructure, composition, residual stress) on pitting damage distributions and rates, conditions of pit-to-crack transition, and crack growth under canister-relevant environments. The goal of these experiments is to (1) determine the relative importance of canister stress levels as a parameter in pitting susceptibility; and (2) determine crack initiation and growth behavior in canister-relevant materials and stress conditions. One important test involved exposing large canister mock-up plates to aggressive corrosion conditions. In addition to providing information on pitting and SCC, these tests were designed to provide information on the likely location and orientation of SCC cracks on in-service canisters—information that will aid in performing canister surface inspections as prescribed by ISFSI site aging management programs.

In FY19, we continued large mockup plate tests initiated in FY18, using higher salt loads and longer exposure times. These longer exposure times provide additional information regarding how the deposited $MgCl_2$ brine evolves when exposed to 80 ºC at 35 % RH for up to 12 months, as well as providing information on pitting, pit growth, pit-to-crack transition, and crack growth. A witness sample, a 4-point bend specimen with a stress level similar to that expected in weld regions of the mockup specimens, was subjected to the same test conditions.

Finally, a new test was initiated, exposing a mockup weld sample to a very aggressive potassium tetrathionate solution in an effort to force the plate to crack. This experiment was directed solely at determining the location and orientation of SCC that might form in canister weld regions.

6.1 80 ºC, 35 % RH Exposure Test

In FY18, three samples were prepared for an exposure test at 80ºC and 35% RH. These samples consisted of salt-loaded mockup canister plates exposed to elevated temperature and humidity conditions to evaluate the locations within canister weld regions that may be most susceptible to SCC—their relationship to material condition and mechanical environment (stress levels). The tests were also to provide information on the expected orientation of the SCC cracks. Three large (~18” × 20”) sections of the mockup canister, containing a longitudinal weld, a circumferential weld, and a weld intersection, were loaded with ~2 g/m^2 of $MgCl_2$ using a custom salt fog chamber. The salt-loaded plates were then placed into an environmental chamber at 80ºC, 35% RH. One sample (the weld intersection) was removed after two months, partially cleaned, and evaluated for SCC using vibrothermography and dye penetrant testing. No cracks were observed using either method, and the decision was made to more heavily coat the remaining two samples and the extend the test for several more months. An additional 8/g m^2 of $MgCl_2$ was added to the surfaces of the samples. Because the weld intersection sample had been cleaned, it was not recoated and re-used. However, a witness sample consisting of a 12″ × 4″ × 5/8″ beam mounted in a 4-point bend fixture was also coated and placed in the RH chamber. While there may be some uncertainty in the surface stresses on the mockup weld samples, the 4-pont bend specimen has well defined tensile surface stresses on the salt-deposited surface; the bend beam was tensioned to produce surface tensile stresses of ~250 MPa.

6.1.1 8 Month Exposure Time

After 8-months of exposure to 80ºC, 35% RH, the longitudinal weld plate was briefly removed from the oven to sample both loose and adhering corrosion product from a small area of the plate. The loose products were brushed off the plate with a small brush, and the adhering products were gently scraped off with a plastic spatula. As shown in Figure 45, when the plate was removed, it was evident that the brine had completely dried out. Bischofite ($MgCl_2$:$6H_2O$) is deliquesced under these conditions, since its deliquescence RH at 80 ºC is below 35 % RH. It is evident that some reaction had occurred, resulting in brine dry-out.

Figure 45. Image of mock-up canister plate after 8-month exposure time to 80ºC, 35 % RH showing the surface of the plate to be completely dry. The images show the removal of the loose corrosion products with a small brush.

The corrosion products were analyzed by SEM/EDS and XRD, and the results are shown in Figure 46. The SEM analysis showed that the corrosion products consisted of loose iron oxide "whiskers" and less abundant, adhering corrosion product frequently displaying a blister morphology. The metal corrosion products have distinct Ni-rich, Cr-rich and Fe- rich areas. From the EDS maps (Figure 46A), it is evident that chloride was pervasive in the corrosion products and associated with both metal oxide corrosion products and with magnesium. Magnesium phases occurred only with the blister material, and frequently displayed a fibrous or bladed texture, that we suspect, from previous work (e.g., Section 2.1), to be a magnesium hydroxychloride. An XRD analysis of the whisker-like corrosion products (Figure 46B) showed that the metal oxide was largely amorphous; however, small peaks for the mineral akaganeite could be identified. Akageneite is an iron oxyhydroxide that contains varying amounts of chloride; a typical composition is $Fe^{3+}_{7.6}Ni_{0.4}O_{6.4}(OH)_{9.7}Cl_{1.3}$, corresponding to about 6 wt% chloride.

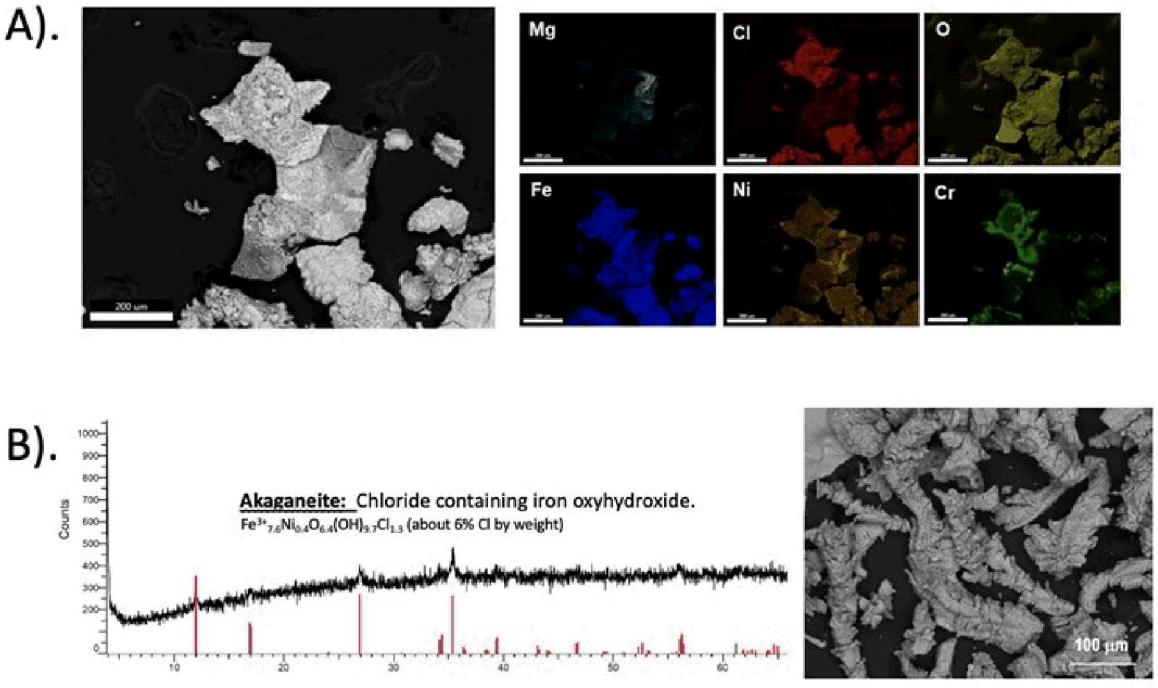

Figure 46. a.) SEM and EDS images of a corrosion product that contains different phases, showing Mg rich areas that appear to be depleted in Cl. Cr and Ni also appear to fractionate to form Ni and Cr rich regions. b.) XRD analysis of the corrosion product shows the presence of akageneite.

It was not possible to separate the magnesium phase from the iron corrosion products for XRD analysis, so the identity of the phase cannot be positively determined. However, some brine dripped off of the plates and onto the chamber racks, where it crystallized. This material was collected and analyzed by XRD and was identified as the 2-1-4 magnesium hydroxychloride phase—the same phase observed in the brine degassing experiments performed under the same temperature and RH conditions, in the absence of corrosion (Section 2.1).

Brine dry-out on the mockup plates may have been driven simply by degassing as seen in Section 2.1. However, it is likely that two other effects played a role as well. First, a significant fraction of the chloride in the brine was apparently sequestered in iron oxides as akaganeite (Figure 46). Second, the corrosion reaction itself may have contributed to magnesium hydroxychloride formation and brine-dry-out. As metal oxidation occurs in a corrosion pit (the anode), a corresponding cathodic current is generated via the oxygen reduction reaction (ORR) in the cathode region surrounding the pit (Figure 47). This reaction generates hydroxyl, and the pH rises in the cathode, potentially resulting in precipitation of Mg-hydroxychlorides. This was observed in experiments carried out in FY18 (Bryan and Schindelholz, 2018). Note that the HER reaction, which appears to be a contributing cathodic reaction in magnesium chloride brines (Section 3.2), also produces hydroxyl groups in the cathode region.

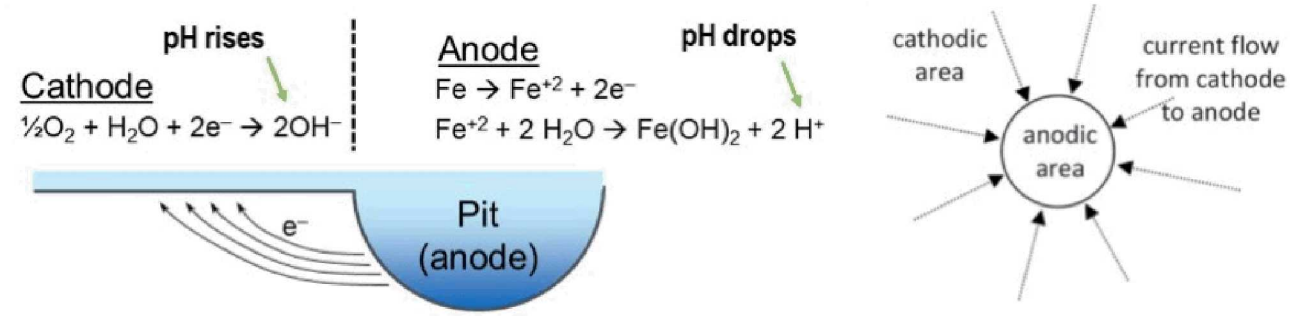

Figure 47. Reactions occurring in the pit and the surrounding cathode.

6.1.2 12 Month Exposure Time

After 12 months of exposure, all samples were removed from the environmental chamber. Each of the samples were completely dry but heavily corroded. Because the corroded surface was completely dry, the original $MgCl_2$ brine had apparently been completely consumed by brine evolution to magnesium hydroxychloride phases or by incorporation into the corrosion products. Photographs of the mock up plates and the 4-point bend specimen are shown in Figure 48.

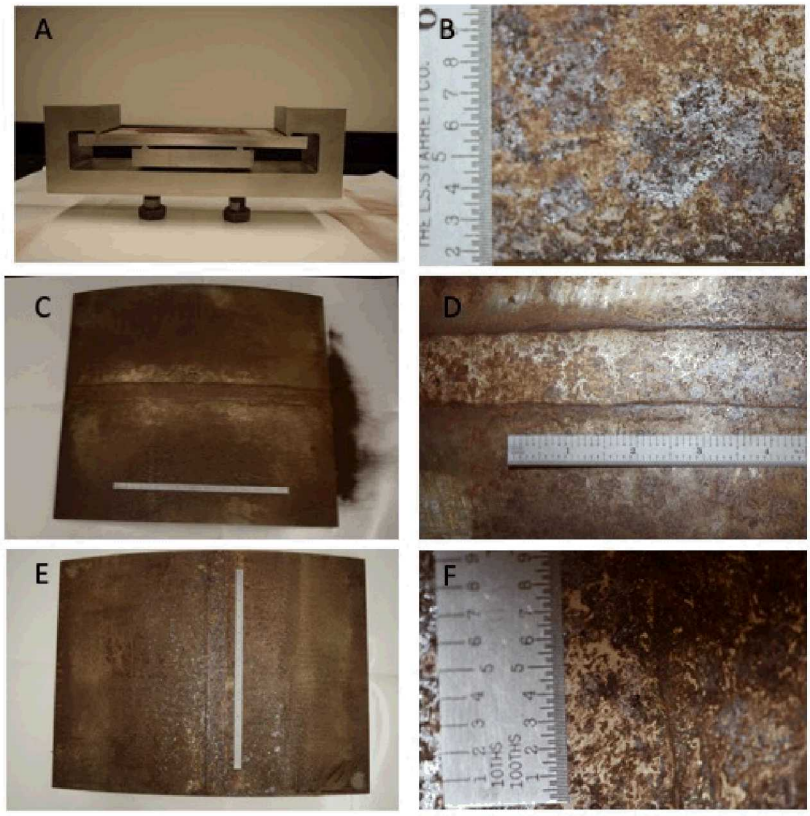

Figure 48. Photograph of the samples from the big plate test. 4-point bend specimen (a,b); circumferential weld specimen (c,d); longitudinal weld specimen (e,f).

The loose whisker-like corrosion products were removed from each sample using a brush, and retained for analysis by XRD, SEM, and IC. Figure 49 shows an SEM image with EDS analyses of corrosion products removed from the 4-point bend sample; there are discrete Mg-rich particles (Area 1) and Fe-rich corrosion products (Areas 2-4). In Area 1, the mineral is rich in Mg, Cl, and O, and displays a fibrous morphology, typical of magnesium hydroxychloride. This suggests that the $MgCl_2$ brine had evolved over the course of the experiment to form a magnesium hydroxychloride, presumably the 2-1-4 phase observed previously under these temperature and RH conditions. These findings help explain why brine dry-out occurred on the surface of the plates. At 80ºC, 35 %RH bischofite is stable and would not dry-out; if completely converted to less deliquescent magnesium hydroxychloride, dry-out would occur.

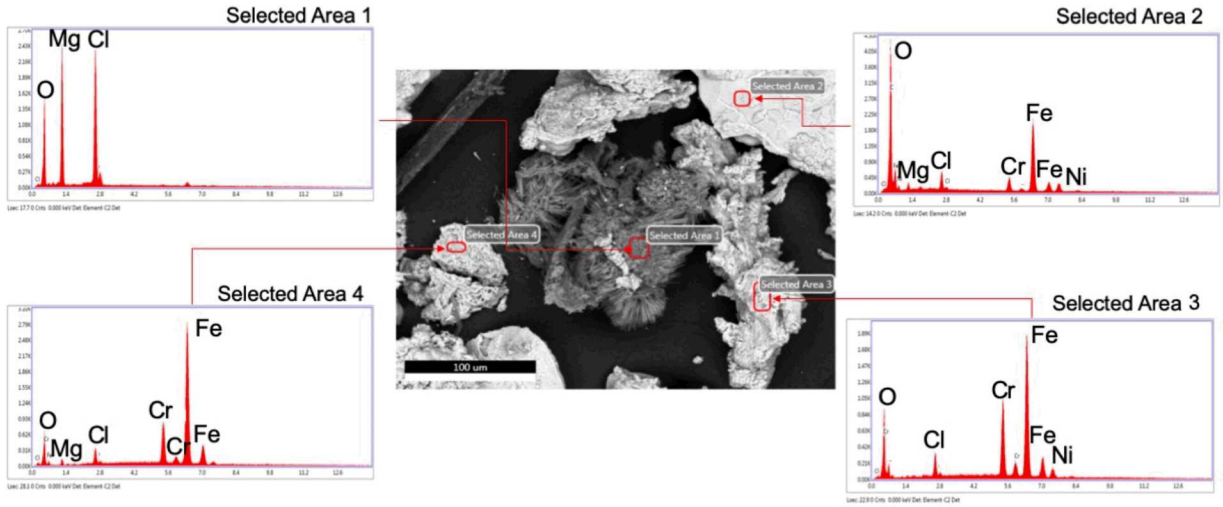

Figure 49. EDS of material from 4-point bend specimen, showing the composition at four locations in the sample.

Further EDS analysis indicates that different Mg-rich phases existed on the sample surface (Figure 50). In Figure 50, the area highlighted in green Mg- and O-rich, but is Cl-depleted. This is likely caused by the degassing of HCl and the conversion from bischofite to less chloride-rich phase, possibly even brucite, which contains no Cl^-. The area highlighted in orange is Mg- and Cl-rich, but contains less oxygen. Given the fibrous morphology, it is likely a magnesium hydroxychloride. It shows significantly more Cl^- present than the phase highlighted in green. In an EDS map of the loose corrosion products found on the longitudinal weld (Figure 51), there is a Mg-rich particle shown in teal. This particle is also Cl-rich and O-rich, suggesting again that the $MgCl_2$ brine had converted to a less deliquescent magnesium hydroxychloride phase.

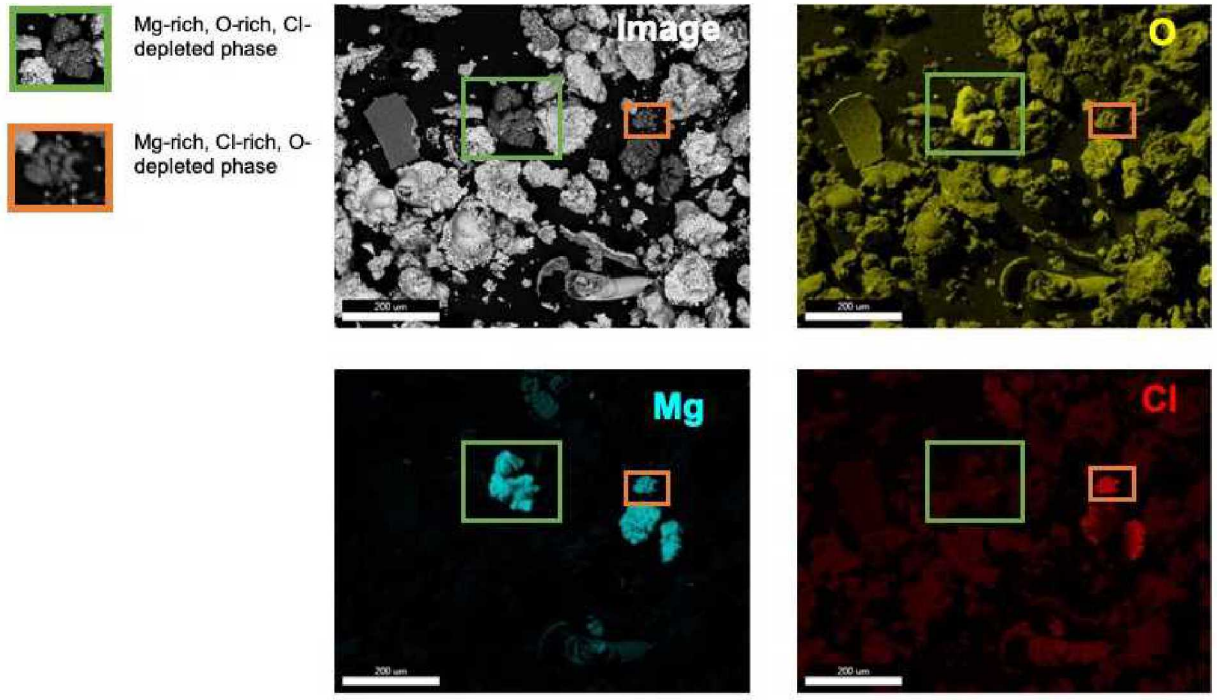

Figure 50. EDS elemental map showing the formation of two different Mg-rich complexes. Highlighted in each of the elemental maps in green is a Mg and O rich phase, but depleted in Cl, suggests brucite formation. Highlighted in orange is a Mg and Cl rich, with slightly less O than in green, suggesting the potential formation of a magnesium hydroxychloride phase or bischofite.

The Fe-rich corrosion products in Figure 49 and Figure 51 are primarily Fe-oxides, and XRD analyses show that akageneite, a chloride-containing iron oxhydroxide, is present. Hence, at least some sequestration of Cl into the Fe-corrosion products occurred. It is not certain how incorporation of chloride into corrosion products may have affected the evolution of the magnesium chloride brine on the metal surface.

Additionally, some fractionation of the different metals occurred in the corrosion products, visible in Figure 51 as Cr-rich and Ni-rich areas. In some spots, Mg appears to be associated with the corrosion products; possibly as a Mg-Fe spinel phase or layered double hydroxide. Lastly, flakes of aluminum hydroxide scale are present, from the aluminum baffles in oven heat exchanger. The environment in the oven was very corrosive as the HCl is degassed, leading to corrosion of the baffles.

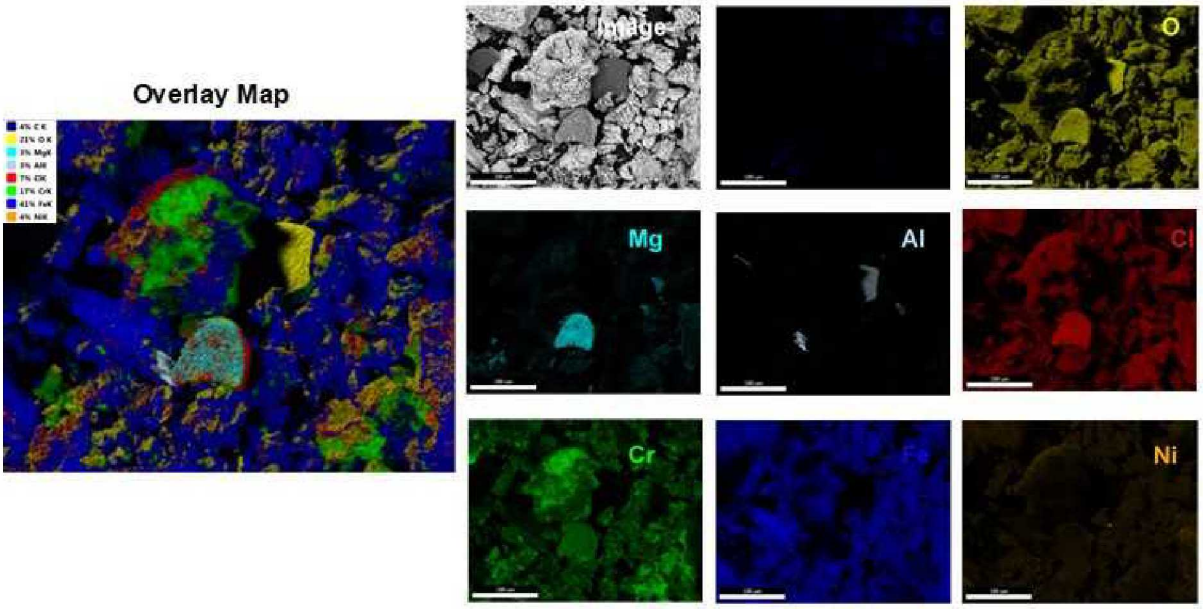

Figure 51. EDS map of the loose corrosion products from the longitudinal weld.

6.1.2.1 Surface Cleaning to Remove Corrosion Products

In order to evaluate the mock up plates and the 4-point bend witness specimen for SCC cracks, the sample surfaces had to be cleaned of corrosion products. Although the loose whisker-like corrosion products were readily removed, attempts to remove the more strongly adhering blister-like corrosion products were only partially successful. Photos of the samples after they were removed from the oven are shown in Figure 48. After removal, the samples were cleaned of corrosion products by soaking in 0.66 M diammonium citrate solution as per ASTM G1. This was only partially successful, and due to concerns that SCC cracks, if present, would be filled with corrosion products, concentrated nitric acid was also applied for short periods in an effort to further clean the samples. The cleaned samples (Figure 52) were then taken to the SNL non-destructive evaluation (NDE) group to be analyzed by dye penetrate testing for SCC cracks. Details on the surface analysis techniques and results are described in Section 6.3.

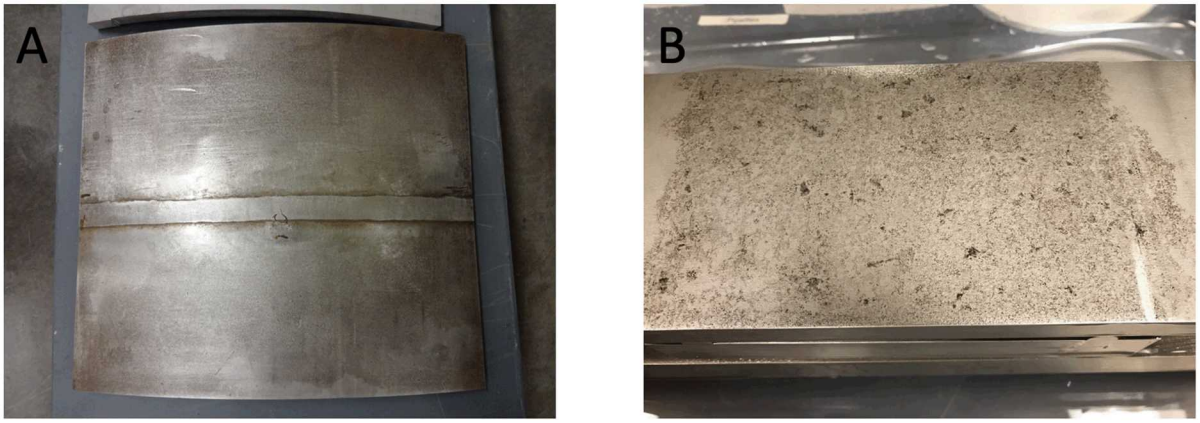

Figure 52. Photographs of a.) circumferential weld mock up plate and b.) 4-point bend specimen post cleaning treatment.

6.2 Potassium Tetrathionate Test

A circumferential weld plate sample from the Sandia mock-up canister was selected to induce SCC using aggressive chemical methods. The goal of this test was to determine where in the weld zone SCC was likely to occur, and what orientation the cracks would likely have relative to the weld. The chemical method used to induce SCC was treatment with potassium tetrathionate ($K_2S_4O_6$). The weld specimen was placed in a 18″ × 24″ × 6″ high density polyethylene (HDPE) tray and immersed with ~15 L of 3% $K_2S_4O_6$, adjusted to pH = 1 using H_2SO_4. The solution immediately reacted with the plate; the heat affected zone (HAZ) turned dark, and the solution became cloudy and rusty in color and emitted a strong sulfurous odor. The $K_2S_4O_6$ solution at low pH values is strongly reducing, and studies have suggested that the cathodic reaction, which determines the corrosion potential, is the reduction of the polythionate to elemental sulfur (Cragnolino and Macdonald, 1982). The cathodic reaction is as follows,

$$S_4O_6^- + 12\,H^+ + 10e^- \rightarrow 4S + 6H_2O \qquad \text{(Eq. 9)}$$

Where, when the solution pH ~ 1, the redox potential is 0.339 V_H, which is about 100 mV higher than the maximum calculated value of the corrosion potential (Cragnolino and Macdonald, 1982). The sample was fully immersed in the room temperature solution for 3 months; then, using a water bath as a heat exchanger, the sample and solution were heated to 40 ºC for the remaining 3 months of the test. Four months into the test, the solution was drained and the sample was inspected for SCC via microscope. No visible cracks were observed and the sample was re-submerged into a fresh 15 L of 3% $K_2S_4O_6$, adjusted to pH = 1 by H_2SO_4, for the remainder of the experiment.

After 7 months of total exposure, the plate was removed from the tetrathionate bath. The surface of the plate was heavily etched. The $K_2S_4O_6$ had reacted with the surface and removed much of the oxide layer, leaving behind a light gray matte finish. To clean the plate, the HDPE tray was filled with deionized water to fully submerge the sample for roughly 24 hours. Periodically, a toothbrush was used to scrub the sample to remove any adhering products that may have formed during the reaction. The tray was drained and refilled with DI water for an additional soak of a few hours. Finally, the cleaned plate was wiped off and allowed to dry (Figure 53). The plate was then taken to the SNL non-destructive evaluation (NDE) group to be analyzed by dye penetrate testing for SCC cracks.

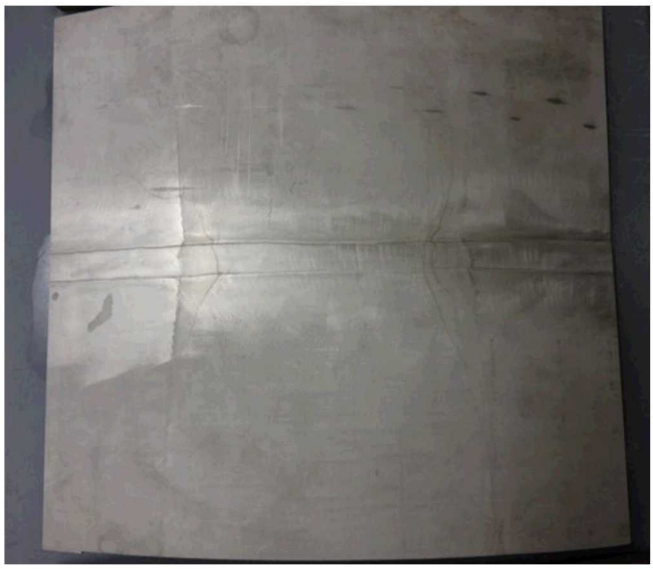

Figure 53. Circumferential weld mockup sample after potassium tetrathionate treatment and cleaning.

6.3 Post-Exposure Analysis for SCC

Fluorescent dye penetrant testing was used to inspect the 4-point bend specimen and the longitudinal and circumferential welds from the Sandia mock-up canister exposed to 80ºC, 35%RH for 12 months, and also the circumferential weld sample exposed to potassium tetrathionate. First, a nonaqueous solvent was used to clean the parts. Then, Method C, Level III Fluorescent penetrant was strategically applied over the entire weld face and heat-effected zone and allowed to dwell on the parts for 30 minutes. The excess penetrant was wiped away using dry wipes, then a nonaqueous developer was applied and allowed to dwell for 15 minutes. The parts were inspected in a darkened room using a black-light, looking for surface breaking defects. The 4-point bend test specimen showed multiple crack indications, all located along the edges of the specimen (Figure 54). None of the three mockup welded plate samples showed any indication of cracking (Figure 55). After the inspection, the parts were cleaned once again with the nonaqueous solvent. A summary of the analysis is presented in Table 15.

It is possible that cracks are present in the mockup weld samples, but are filled with corrosion products, and hence did not absorb the dye during dye penetrant testing. To assess this, the plates are currently undergoing eddy current/ultrasound testing.

Table 15. Inspected Specimen and Noted Indications

Part Inspected	Exposure	Crack Indications	Notes
Circumferential Welded Plate	3% potassium tetrathionate, pH = 1	No	
Circumferential Welded Plate	80 ºC, 35 % RH	No	
Longitudinal Welded Plate	80 ºC, 35 % RH	No	High background due to corroded surface
4-point Bend Specimen	80 ºC, 35 % RH	Yes	

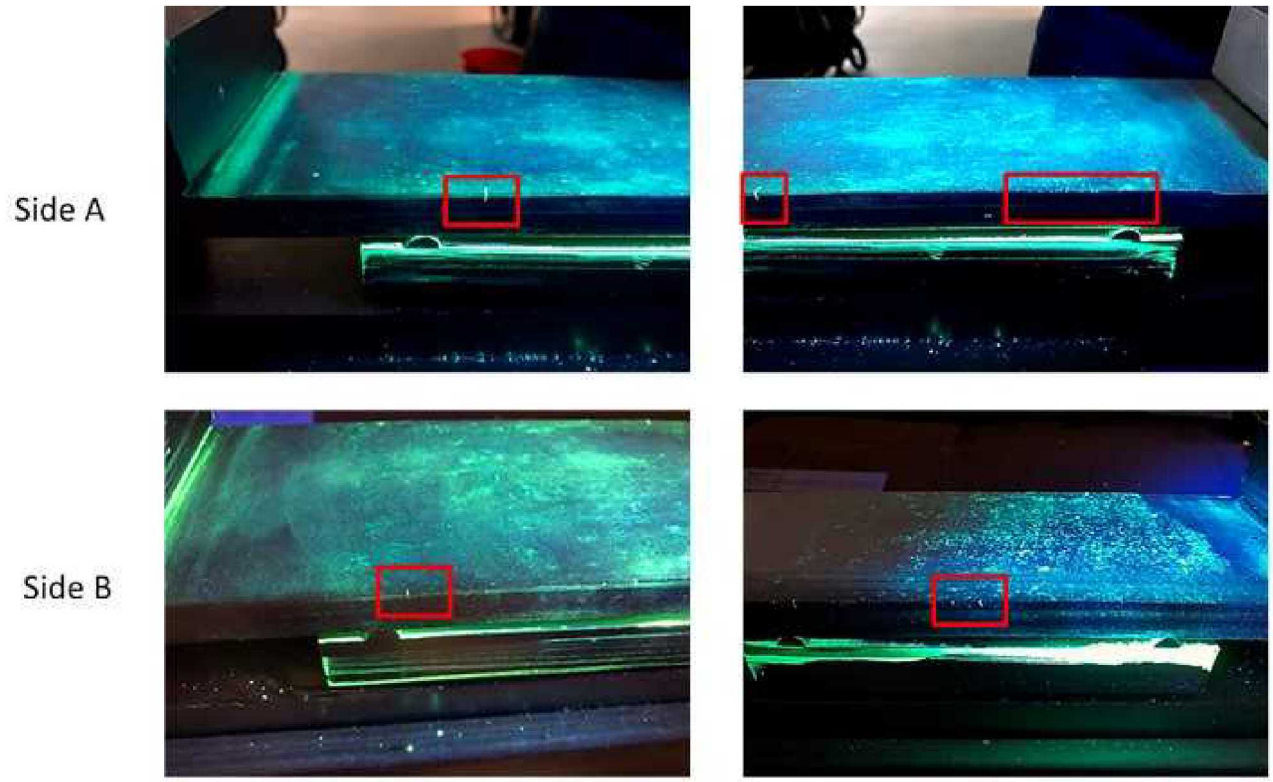

Figure 54. Photographs of the 4-point bend specimen under an ultraviolet light. The upper two figures show a series of cracks on one edge (Side A) of the 4-point bend specimen, with one large crack and several smaller cracks. The other two figures show cracks on the opposite side (Side B) of the specimen.

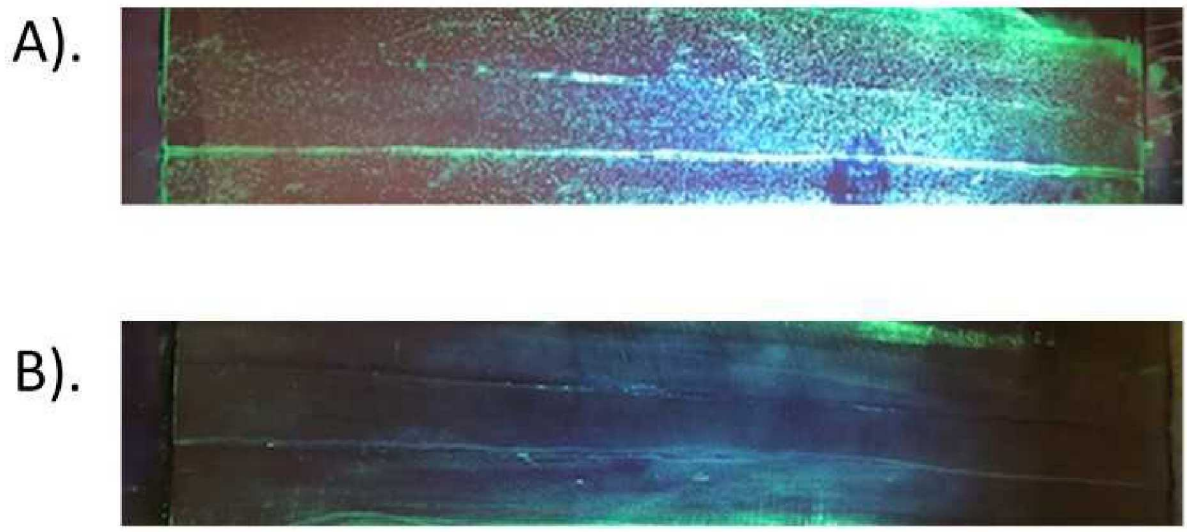

Figure 55. Photographs of the a.) circumferential weld mock up plate exposed to 80°C, 35% RH for 12 months and chemically cleaned b.) circumferential weld mock up plate exposed to 3% potassium tetrathionate for 7 months and cleaned

7. FY20 FUTURE EXPERIMENTAL DIRECTIONS

Experimental efforts in FY20 will focus on continued work to understand the chemical environment on heated canister surfaces, and on understanding the relationship between surface environment, corrosion damage, and susceptibility to SCC.

In FY20, SNL will work with EPRI and with industry to continue collection and characterization of dusts and salts deposited on the surface of in-service canisters when opportunities present themselves. Early in F20, we will collect witness coupons and 4-point bend samples deposited in in-service storage systems at the Maine Yankee Nuclear facility. These samples have been exposed for 2 years and will provide information of the relative aggressiveness of the environment at the site.

SNL will also continue experiments to determine the stability and evolution of sea-salt brines, with a focus on magnesium chloride-rich brines. We will work with German collaborators to develop our ability to predict magnesium hydroxychloride phase formation as a function of temperature and brine composition, and will synthesize and characterize magnesium hydroxychloride phases to determine their deliquescence properties.

Experimental evaluation of magnesium chloride brine stabilities will also continue in FY20. An improved flow system for evaluating brine stabilities has been developed and is currently in use. This system is capable of much higher air-flow rates, enabling assessment of degassing reactions at lower temperatures, where degassing is much slower.

Finally, in FY20, we will begin to evaluate the effects of additional atmospheric reactions on brine stability. These include reactions with NO_x and SO_x, the likely products of which, nitrates and sulfates, have frequently been observed in dusts collected from in-service canisters. Both thermodynamic modeling and experimental methods will be sued to assess these processes.

In FY20, the corrosion work will continue to focus on four thrust areas: (1) generation of an expanded statistical pitting data set as function of environment, specifically at elevated temperatures, under cyclic conditions, and exploring material and microstructural influences; (2) hierarchal identification of features controlling pit-to-crack transitions; (3) further parameterization of the surface environment-electrochemical relationship driving pitting and SCC to validate and/or refine currently applied models; (4) definition of the relationship between surface environmental conditions, cathodic kinetics, and subsequent control of SCC CGR and susceptibility.

Regarding (1), in Q1 we will expand the pitting matrix to include increased temperature extremes. Additionally, FY20 will focus on exploring the relationship between electrolyte coverage, size, amount, and the resultant pit morphology to better develop pitting statistics that can be used incorporate the influence or possible significance of pit geometry into SCC cracking models. Pitting statistics will also be generated for a large-scale coupon exposure under cyclic humidity and temperature conditions to replicate the effects of diurnal variation in ambient weather. These data will be used to directly test the SNL probabilistic SCC model predictions of maximum pit size as a function of environmental conditions, and they will also be used to develop statistical models. Continued collaboration with OSU is planned.

For (2), further post-mortem examination of the initial tensile specimen in conjunction with the unloaded humidity chamber exposed samples will be carried out in FY20, including fractography, to help elucidate these issues. FY20 will also include the design and initial implementation of experiments highlighting possible deleterious features for crack initiation determined from detailed pitting tests described in Section 4. Continued collaboration with OSU is planned.

Regarding (3), FY20 will continue to explore the relationship between initial brine conditions, brine evolution and corrosion product formation, total corrosion current, and corrosion damage to determine the corrosion pathways in ISFSI-relevant environments. Longer-term dual electrode experiments will be carried out for determination of brine evolution and the effects of changing brine composition, properties,

and volume, on corrosion. These data will help enable validation and/or refinement of assumptions made in the maximum pit size model to better enhance the overall SCC cracking predictions. Additionally, a manuscript on the cathodic kinetics measured in FY19 for $MgCl_2$ brines is under preparation for submission in Q1 of FY20.

For thrust (4), in FY20, four additional load frames will be installed at SNL. This will enable SNL to develop appropriate tests and generate CGR data to evaluate the environmental dependencies of SCC crack initiation and growth rates. Initial tests will validate novel sample designs under immersed conditions in canister-relevant brines. Then, application of these samples under atmospheric conditions will enable the study of the influence of the environment exposure conditions and cathodic kinetics on CGR. Continued collaboration with DNV-GL is expected.

Additional work regarding the analysis of 4-point bend specimens provided by CSM to understand how stress impacts pitting behavior will be completed in Q1 of FY20, with preparation of a manuscript for submission. Finally, continued characterization of the long-term exposure salt-loaded mock-up plates will be carried out to better determine the interactions of material variance on localized corrosion and SCC behavior.

8. CONCLUSIONS

This progress report describes work done in FY19 at Sandia National Laboratories (SNL) to assess the localized corrosion performance of container/cask materials used in the interim storage of spent nuclear fuel (SNF). Of particular concern is stress corrosion cracking (SCC), by which a through-wall crack could potentially form in a canister outer wall over time intervals that are shorter than possible dry storage times. Work in FY19 refined our understanding of the chemical and physical environment on canister surfaces and evaluated the relationship between chemical and physical environment and the form and extent of corrosion that occurs.

Work to define the chemical and physical environment that could develop on storage canister surfaces in near-marine environments included continued characterization of samples from experiments run in FY18, to evaluate the thermal stability of magnesium chloride brines, representative of the first brines to form when sea-salts deliquesce, with the specific goal of understanding and interpreting results of sea-salt and magnesium chloride corrosion experiments carried out under accelerated conditions. The experiments confirmed that magnesium chloride brines, and by extension, low RH sea-salt deliquescent brines, are not stable at elevated temperatures, losing chloride *via* degassing of HCl and conversion to Mg-hydroxychlorides and carbonates. The experiments were carried out on an inert substrate to eliminate the effects of corrosion reactions, simulating brine stabilities in the absence of corrosion. In FY18, analysis of salts recovered from actively corroding metal samples showed that corrosion also drives conversion of magnesium chloride less deliquescent hydroxychloride phases. Samples collected from additional corrosion experiments in FY19 confirmed these reactions, and three different Mg-hydroxide or hydroxychloride phases have now been identified as forming. This process has significant implications on corrosion, as the secondary phases are less deliquescent than magnesium chloride; the conversion reaction results in decreases in brine volume, and potentially ultimately results in brine dry-out. To better predict the stability of Mg-chloride (and sea-salt) brines, SNL is working to develop a thermodynamic database for known magnesium hydroxide, chloride, and hydroxychloride phases. Thermodynamic and solubility data, available for a few phases, has been compiled, and a component contribution method has been used to estimate thermodynamic data for the other Mg phases of interest; those data are being refined by fitting of available solubility data.

Experimental efforts in FY19 to understand the relationship between surface environment and corrosion damage focused on four thrust areas: (1) generation of temporal statistical pitting data as function of environment; (2) hierarchal identification of features controlling pit-to-crack transitions; (3) definition of the surface environment-electrochemical relationship driving pitting and SCC; (4) definition of relative governance on material condition and stress relative to surface environmental conditions on electrochemical kinetics and SCC susceptibility. In FY19, work to characterize pitting damage and surface chemistry on 304L coupons loaded with sea-salt and exposed to ISFSI-relevant fixed RH, T conditions continued. The final samples, exposed for two years in RH chambers, have been collected. Working with the Ohio State University (OSU), we have used optical profilometry to generate initial pit datasets for coupon exposure times up to 1.5 years. These data will be used to directly test the maximum pit size model incorporated into the SNL SCC model, and to develop statistical models in collaboration with Colorado School of Mines (CSM). Regarding (2), and in collaboration with OSU, experiments have been initiated to identify pit-to-crack transition features. Accomplishments include deposition of salt and exposure of tensile test specimens to the environmental conditions used in thrust (1) for up to six months, followed by an initial tensile loading experiment to identify pit features that might provide focal points for SCC initiation. Additionally, we have developed and tested a method for periodic loading of the specimens while under said environments. Regarding (3), the cathodic electrochemical kinetics that drive corrosion on stainless steel were measured for NaCl and $MgCl_2$ brines as analogs to expected brines compositions on the canisters at the upper end of expected ISFSI surface humidity range. These data were incorporated into SNL's SCC model and findings communicated in a peer-reviewed journal publication. Additional work with surrogate cathodic brines (without the influence of chlorides) was also

carried out. Work in area (4) included completion of 4-point bend experiments using stressed 304L bars loaded with sea salt and exposed to 35%RH, 50°C conditions in collaboration with CSM. The pit distribution on one of these bars was analyzed via optical profilometry with initial results suggesting pit frequency, depth and diameter was independent on material stress state within expected canister conditions. Comparisons to electrochemical investigations of similarly stressed 304L bars corroborate this finding for canister-relevant brines. Finally, we completed exposure of a salt-loaded mockup canister plates to elevated RH, T conditions to determine what portions of the canister may be most susceptible to SCC and their relationship to material condition and mechanical environment. Those samples are currently being evaluated for SCC cracks using three different NDE methods.

9. REFERENCES

Altmaier, M., Metz, V., Neck, V., Muller, R. and Fanghanel, T. (2003). Solid-liquid equilibria of Mg(OH)(2)(cr) and Mg-2(OH)(3)Cl center dot 4H(2)O(cr) in the system Mg-Na-H-OH-O-Cl-H2O at 25 degrees C. *Geochimica et Cosmochimica Acta* **67**, 3595-3601.

ASTM International. (2008). *D1141-98: Standard Practice for the Preparation of Substitute Ocean Water.* American Society for Testing and Materials, p.

Ba, H. J. and Guan, H. (2009). Influence of MgO/MgCl2 molar ratio on phase stability of magnesium oxychloride cement. *Journal of Wuhan University of Technology-Materials Science Edition* **24**, 476-481.

Bethke, C. (2008). *Geochemical and Biogeochemical Reaction Modeling*: Cambridge Press.

Brown, P. L., Drummond, S. E. and Palmer, D. A. (1996). Hydrolysis of magnesium(II) at elevated temperatures. *Journal of the Chemical Society-Dalton Transactions*, 3071-3075.

Bryan, C. and Enos, D. (2016). *Analysis of Dust Samples Collected from an In-Service Interim Storage System at the Maine Yankee Nuclear Site.* SAND2016-10266. Sandia National Laboratories, 51 p.

Bryan, C. and Schindelholz, E. (2018). *FY18 Status Report: SNL Research into Stress Corrosion Cracking of SNF Interim Storage Canisters.* Milestone # M2SF-18SN010201049. U.S. Department of Energy, 77 p.

Bryan, C., Schindelholz, E., Knight, A. and Taylor, J. (2019). Composition and Evolution of Sea-salt Deliquescent Brines on SNF Storage Canister Surfaces. *PATRAM 2019*. New Orleans, LA: World Nuclear Transport Institute, 9 p.

Burstein, G. and Pistorius, P. (1995). Surface roughness and the metastable pitting of stainless steel in chloride solutions. *Corrosion* **51**, 380-385.

Carpenter, J. H. (1965). The Chesapeake Bay Institute Technique for the Winkler Dissolved Oxygen Method. *Limnology and Oceanography* **10**, 141-143.

Chen, Z. and Kelly, R. (2010). Computational modeling of bounding conditions for pit size on stainless steel in atmospheric environments. *Journal of the Electrochemical Society* **157**, C69-C78.

Chermak, J. A. and Rimstidt, J. D. (1989). Estimating the Thermodynamic Properties (Delta-Gfo and Delta-Hfo) of Silicate Minerals at 298-K from the Sum of Polyhedral Contributions. *American Mineralogist* **74**, 1023-1031.

Clynne, M. A. and Potter, R. W. (1979). Solubility of Some Alkali and Alkaline-Earth Chlorides in Water at Moderate Temperatures. *Journal of Chemical and Engineering Data* **24**, 338-340.

Cragnolino, G. and Macdonald, D. D. (1982). Intergranular Stress-Corrosion Cracking of Austenitic Stainless-Steel at Temperatures Below 100-C - a Review. *Corrosion* **38**, 406-424.

de Abreu, C. P., Costa, I., de Melo, H. G., Pebere, N., Tribollet, B. and Vivier, V. (2017). Multiscale Electrochemical Study of Welded Al Alloys Joined by Friction Stir Welding. *Journal of the Electrochemical Society* **164**, C735-C746.

Dick, J. M. (2019). CHNOSZ: Thermodynamic Calculations and Diagrams for Geochemistry. *Frontiers in Earth Science* **7**.

Donahue, J. R. and Burns, J. T. (2016). Effect of chloride concentration on the corrosion–fatigue crack behavior of an age-hardenable martensitic stainless steel. *International Journal of Fatigue* **91**, 79-99.

Einaga, H. (1981). The Hydrolytic Precipitation Reaction of Mg(Ii) from Aqueous Nano3 Solution. *Journal of Inorganic & Nuclear Chemistry* **43**, 229-233.

Enos, D. and Bryan, C. (2016). *Final Report: Characterization of Canister Mockup Weld Residual Stresses.* FCRD-UFD-2016-000064. U.S. DOE, 62 p.

EPRI. (2015). *Susceptibility Assessment Criteria for Chloride-Induced Stress Corrosion Cracking (CISCC) of Welded Stainless Steel Canisters for Dry Cask Storage Systems.* Electric Power Research Institute, 206 p.

Giauque, W. F. and Archibald, R. C. (1937). The entropy of water from the third law of thermodynamics - The dissociation pressure and calorimetric heat of the reaction Mg(OH)(2) = MgO+H2O- The heat capacities of Mg(OH)(2) and MgO from 20 to 300(o)K. *Journal of the American Chemical Society* **59**, 561-569.

Harvie, C. E., Moller, N. and Weare, J. H. (1984). The Prediction of Mineral Solubilities in Natural-Waters - the Na-K-Mg-Ca-H-Cl-So4-Oh-Hco3-Co3-Co2-H2o System to High Ionic Strengths at 25-Degrees-C. *Geochimica et Cosmochimica Acta* **48**, 723-751.

Hazen, R. M. (1985). Comparative Crystal-Chemistry and the Polyhedral Approach. *Reviews in Mineralogy* **14**, 317-346.

Horner, D., Connolly, B., Zhou, S., Crocker, L. and Turnbull, A. (2011). Novel images of the evolution of stress corrosion cracks from corrosion pits. *Corrosion Science* **53**, 3466-3485.

Kadowaki, M., Muto, I., Sugawara, Y., Doi, T., Kawano, K. and Hara, N. (2017). Real-time microelectrical observations of very early stage pitting on ferrite-pearlite steel in chloride solutions. *Journal of Electrochemical Society* **164**.

Knacke, O., Kubaschewski, O. (1990). *Thermochemical Properties of Inorganic Substances 2nd*. Berlin, Germany: Springer-Verlag.

Kondo, Y. (1989). Prediction of fatigue crack initiation life based on pit growth. *Corrosion* **45**, 7-11.

Konigsberger, E., Konigsberger, L. C. and Gamsjager, H. (1999). Low-temperature thermodynamic model for the system Na2CO3-MgCO3-CaCO3-H2O. *Geochimica et Cosmochimica Acta* **63**, 3105-3119.

Krumgalz, B. S. (2017). Temperature Dependence of Mineral Solubility in Water. Part I. Alkaline and Alkaline Earth Chlorides. *Journal of physical and chemical reference data* **46**.

Liu, Z. Z., Balonis, M., Huang, J., Sha, A. M. and Sant, G. (2017). The influence of composition and temperature on hydrated phase assemblages in magnesium oxychloride cements. *Journal of the American Ceramic Society* **100**, 3246-3261.

Lothenbach, B., Matschei, T., Moschner, G. and Glasser, F. P. (2008). Thermodynamic modelling of the effect of temperature on the hydration and porosity of Portland cement. *Cement and Concrete Research* **38**, 1-18.

Macdonald, D. D. and Urquidi-Macdonald, M. (1991). A coupled environment model for stress-corrosion cracking in sensitized Type-304 stainless-steel in LWR environments. *Corrosion Science* **32**, 51-81.

Moayed, M. H., Laycock, N. and Newman, R. (2003). Dependence of the critical pitting temperature on surface roughness. *Corrosion Science* **45**, 1203-1216.

Mostafa, A. T. M. G., Eakman, J. M., Montoya, M. M. and Yarbro, S. L. (1996). Prediction of Heat Capacities of Solid Inorganic Salts from Group Contributions. *Industrial & Engineering Chemistry Research* **35**, 343-348.

Navai, F. and Debbouz, O. (1999). AES study of passive films formed on a type 316 austenitic stainless-steels in a stress field. *Journal of Materials Science* **34**, 1073-1079.

Nazarov, A., Vivier, V., Thierry, D., Vucko, F. and Tribollet, B. (2017). Effect of Mechanical Stress on the Properties of Steel Surfaces: Scanning Kelvin Probe and Local Electrochemical Impedance Study. *Journal of the Electrochemical Society* **164**, C66-C74.

Newman, J. and Raju, I. (1981). An empirical stress-intensity factor equation for the surface crack. *Engineering Fracture Mechanics* **15**, 185-192.

Newman, J. C. and Raju, I. S. (1979). *Analysis of Surface Cracks in Finite Plates Under Tension or Bending Loads.* Technical Paper 1578 NASA, p.

Newman, R. C. (2002). Stress-corrosion cracking mechanisms. *CORROSION TECHNOLOGY-NEW YORK AND BASEL-* **17**, 399-450.

O'Brien, C. J., Alexander, C., Bryan, C. R., Schindelholz, E. and Dingreville, R. (2019). *Status Report: Uncertainty Quantification of Environmentally Assisted Stress Corrosion Cracking in Used Fuel Canisters.* Milestone # M3SF-19N010201047. Sandia National Laboratories, 123 p.

Pabalan, R. T. and Pitzer, K. S. (1987). Thermodynamics of Concentrated Electrolyte Mixtures and the Prediction of Mineral Solubilities to High-Temperatures for Mixtures in the System Na-K-Mg-Cl-So4-Oh-H2o. *Geochimica et Cosmochimica Acta* **51**, 2429-2443.

Pannach, M. (2019). Löslichkeitsgleichgewichte basischer Magnesiumchlorid- und Magnesiumsulfat-Hydrate in wässrigen Lösungen bei 25 °C bis 120 °C Freiberg, Germany: Der Fakultät für Chemie und Physik der Technischen Universität Bergakademie Freiberg genehmigte

Pannach, M., Bette, S. and Freyer, D. (2017). Solubility Equilibria in the System Mg(OH)(2)-MgCl2-H2O from 298 to 393 K. *Journal of Chemical and Engineering Data* **62**, 1384-1396.

Phutela, R. C., Pitzer, K. S. and Saluja, P. P. S. (1987). Thermodynamics of Aqueous Magnesium-Chloride, Calcium-Chloride, and Strontium Chloride at Elevated-Temperatures. *Journal of Chemical and Engineering Data* **32**, 76-80.

Robie, R. A., Hemingway, B. S. (1995). Thermodynamic properties of minerals and related substances 298.15 K and 1 Bar(10^5 Pascals) pressure and at higher temperatures. . *U.S. Geological Survey Bulletin.*

Robinson, W. O., Waggaman W. H. . (1908). Basic Magnesium Chlorides. *Journal of Physical Chemistry* **13**, 673-678.

Schindelholz, E., Bryan, C. and Alexander, C. (2017). *FY17 Status Report: Research on Stress Corrosion Cracking of SNF Interim Storage Canisters.* SFWD-SFWST-2017-000003. U.S. Department of Energy, 59 p.

Schindelholz, E., Bryan, C., Alexander, C. (2017). FY17 Status Report: SNL Research Into Stress Corrosion Cracking of SNF Interim Storage Canisters. In: Energy, U. S. D. o. (ed.).

Schindelholz, E. and Kelly, R. G. (2010). Application of Inkjet Printing for Depositing Salt Prior to Atmospheric Corrosion Testing. *Electrochemical and Solid State Letters* **13**, C29-C31.

Schindelholz, E., Rodelas, J., M., M. and Montoya, T. (2019). *Corrosion Testing of Friction Stir Welded 304L Stainless Steel* Sandia National Laboratories, 24 p.

Thurmond, V. L., Potter, R. W. and Clynne, M. A. (1984). The Densities of Saturated Solutions of NaCl and KCl from 10 ºC to 105 ºC In: Survey, U. S. G. (ed.), 10.

Turnbull, A., Horner, D. and Connolly, B. (2009). Challenges in modelling the evolution of stress corrosion cracks from pits. *Engineering Fracture Mechanics* **76**, 633-640.

Turnbull, A., McCartney, L. and Zhou, S. (2006). Modelling of the evolution of stress corrosion cracks from corrosion pits. *Scripta materialia* **54**, 575-578.

Wagman, D. D., Evans, W. H., Parker, V. B., Schumm, R. H., Halow, I., Bailey, S. M., Churney, K. L. and Nuttall, R. L. (1982). The Nbs Tables of Chemical Thermodynamic Properties - Selected Values for Inorganic and C-1 and C-2 Organic-Substances in Si Units. *Journal of physical and chemical reference data* **11**, 1-&.

Wolery, T. J. (2010). *EQ3/6 A Software Package for Geochemical Modeling*: ; Lawrence Livermore National Lab. (LLNL), Livermore, CA (United States).

Xiong, Y. L., Deng, H. R., Nemer, M. and Johnsen, S. (2010). Experimental determination of the solubility constant for magnesium chloride hydroxide hydrate (Mg3Cl(OH)(5)center dot 4H(2)O, phase 5) at room temperature, and its importance to nuclear waste isolation in geological repositories in salt formations. *Geochimica et Cosmochimica Acta* **74**, 4605-4611.

Yang, Q., Yu, J. G. and Luo, J. L. (2003). The influence of hydrogen and tensile stress on passivity of type 304 stainless steel. *Journal of the Electrochemical Society* **150**, B389-B395.

Zhou, Z., Chen, H. S., Li, Z. J. and Li, H. J. (2015). Simulation of the properties of MgO-MgfCl(2)-H2O system by thermodynamic method. *Cement and Concrete Research* **68**, 105-111.

Appendix A

Weirich T.D., Srinivasan J., Taylor J., Melia M., Noell P., Bryan C., & Schindelholz E. (2019). Humidity Effects on Pitting of Ground Stainless Steel Exposed to Sea Salt Particles. *Journal of The Electrochemical Society*, *166*(11), C3477-C3487.

Journal of The Electrochemical Society, **166** (11) C3477-C3487 (2019) C3477

JES Focus Issue on Advanced Techniques in Corrosion Science in Memory of Hugh Isaacs

Humidity Effects on Pitting of Ground Stainless Steel Exposed to Sea Salt Particles

Timothy D. Weirich,[1] Jayendran Srinivasan,[1,*] Jason M. Taylor,[2] Michael A. Melia,[2] Philip J. Noell,[2] Charles R. Bryan,[2] Gerald S. Frankel,[1,] Jenifer S. Locke,[1,*] and Eric J. Schindelholz[2,*,z]**

[1]*Fontana Corrosion Center, Department of Materials Science and Engineering, The Ohio State University, Columbus, Ohio 43210, USA*
[2]*Sandia National Laboratories, Albuquerque, New Mexico 87185, USA*

The effect of relative humidity (RH) on the corrosion of coarse-ground 304 stainless steel exposed for one year under sea salt particles was investigated. Total corrosion damage accumulation was higher at 40% RH than at 76% RH. At 40% RH, pits were numerous and irregularly shaped with a rough, cross-hatched structure. At 76% RH, pits were much fewer in number and ellipsoidal with crystallographically faceted surfaces. Higher E_{pit} resulting from lower [Cl^-] impeded initiation at 76% RH. Cathodic resource competition likely limited growth and resulted in lower total volume loss. At 40% RH, lower E_{pit} due to higher [Cl^-] led to initiation of multiple pits supported by discrete cathodes under individual droplets. Despite more cathodic current available at 76% RH, higher damage accumulation at 40% RH was due to lower anodic stability requirements resulting from higher [Cl^-]. At 76% RH, pitting proceeded with increasing active area at conditions above critical stability, leading to ellipsoidal pits with facets. The cross-hatched morphology at 40% RH was ascribed to growth at the critical stability conditions, driven by constant current through a fixed active area. Small cracks at the 40% RH pits might have been caused by hydrogen environment assisted cracking.
 [DOI: 10.1149/2.0551911jes]

Manuscript submitted March 25, 2019; revised manuscript received June 20, 2019. Published July 8, 2019. *This paper is part of the JES Focus Issue on Advanced Techniques in Corrosion Science in Memory of Hugh Isaacs.*

Chloride-containing environments cause pitting in stainless steel (SS), which can lead to the initiation of stress corrosion cracking (SCC).[1–5] In marine coastal areas, hygroscopic sea salt particles that are deposited on metallic surfaces deliquesce into chloride brines, forming a corrosive environment. Corrosion upon exposure to these brines is strongly influenced by the relative humidity (RH), temperature, and the amount and chemistry of salt deposited.[6–11]

Specifically, the RH determines the volume, surface distribution, chemistry, and physicochemical properties of the brine electrolyte, which in turn affect corrosion kinetics and damage distribution.[10–14] Work on corrosion damage of SS exposed to sea salt or its primary constituents has shown that pitting and SCC initiation rates generally increase with decreasing RH.[8,10,11,15–20] Street et al.[17] characterized pits on 304L SS under microliter-sized $MgCl_2$ droplets after 24 hours of exposure to RH values between 33% and 56%. Circular dish-shaped crystallographic pits with satellite pits on the edge were seen at low RH, as also reported by Maier and Frankel,[20] while the pits that grew at high RH were spiral-shaped. Guo et al.[15] conducted a similar study with mixed salts, reporting that crevice corrosion on 304 SS occurred under NaCl crystals that had precipitated out of solution when the RH fell below 76%. The observed damage morphology included irregular crystallographic crevice attack under NaCl crystals and dish-shaped pits that formed between the crystals.

Notwithstanding the contribution of these studies toward revealing critical aspects of RH effects on SS corrosion damage, the combined effects of humidity, salt loading, and salt distribution on pit evolution in marine atmospheric environments are still not understood completely. Studies to date have examined corrosion under microliter-sized drops of diameters between 1 and 10 mm.[1,3,15,17–19] However, excluding sea spray, dewing, and precipitation, surfaces exposed to marine coastal environments are usually covered in assemblages of nano- to microscale sea salt particles that create droplets that are orders of magnitude smaller in volume.[21–24] Further, while controlled laboratory studies have dealt primarily with the initial stages of corrosion (usually up to a week), information on how pitting matures over longer time periods (years) is necessary to provide the basis for the development and validation of pitting damage function models for service life applications.[25,26]

Given that SS structural components often undergo surface machining or grinding prior to use, it is imperative to consider the effects of any associated microstructural changes on corrosion susceptibility. Previous studies of the effects of RH on corrosion damage morphology[6,17–19] have not explicitly considered surface finish and have typically employed finely ground/polished surfaces. These surfaces do not necessarily reflect actual use conditions where finish is often coarser (milled or ground).[27–30] Damage from impact and transport may also introduce surface defects. Surface preparation and roughness have been reported to affect pit initiation[31–33] and SCC[5,27,28,30,34–36] in SS exposed to both atmospheric and full immersion conditions. In studies of pitting and SCC susceptibility of 304 SS exposed to $MgCl_2$ droplets, Turnbull et al.[5] evaluated the residual stresses that arise from surface grinding procedures on 304 SS and characterized the resulting deformed subsurface nanocrystalline microstructure. The authors observed cracks that were noted to be potentially linked to these effects of grinding. Other studies of SCC susceptibility in full immersion have also shown a dependence on residual stress and preferential dissolution along slip bands introduced by surface deformation.[1,27,28,35] Further, SCC was almost always found in association with pits,[5,30,36] supporting the notion that these pits may serve as crack initiation sites.

The objective of this study was to understand how changes in RH affect corrosion in ground SS exposed over an extended period of time to aerosol-sized sea salt particles. Predetermined volumes of artificial sea salt solution simulating marine aerosol deposition[24,37] were printed onto ground 304 SS surfaces that were then exposed for one year to two RH conditions: 40% and 76%. The resulting corrosion damage morphology and distribution were interpreted in terms of the RH effects on the surface coverage, volume, and chemistry of the electrolyte and subsequent effects on the anodic and cathodic parameters controlling pitting. Distinct microstructural features associated with surface preparation were observed upon characterization of the damage morphology. The possible mechanisms by which such features and changes in pit chemistry due to RH may determine pitting and SCC susceptibility of SS in marine atmospheres are discussed.

*Electrochemical Society Member.
**Electrochemical Society Fellow.
[z]E-mail: ejschi@sandia.gov

This page is intentionally left blank.

Appendix B

Katona R., Carpenter J., Schindelholz E., & Kelly, R. (2019). Prediction of Maximum Pit Sizes in Elevated Chloride Concentrations and Temperatures. Journal of The Electrochemical Society, 166(11), C3364-C3375.

C3364 *Journal of The Electrochemical Society*, **166** (11) C3364-C3375 (2019)

JES Focus Issue on Advanced Techniques in Corrosion Science in Memory of Hugh Isaacs

Prediction of Maximum Pit Sizes in Elevated Chloride Concentrations and Temperatures

R. M. Katona,[1,2] J. Carpenter,[3] E. J. Schindelholz,[3,*] and R. G. Kelly[1,**,z]

[1] *Materials Science and Engineering, University of Virginia, Charlottesville, Virginia 22904, USA*
[2] *Storage and Transportation Technology, Sandia National Laboratories, Albuquerque, New Mexico 87123, USA*
[3] *Materials Reliability, Sandia National Laboratories, Albuquerque, New Mexico 87123, USA*

Calculated maximum pit sizes for stainless steel 304L (SS304L) are presented for atmospheric conditions with elevated chloride concentrations and temperatures. These calculations were carried out by experimentally determining the pit stability product ($(i \cdot x)_{sf}$), repassivation potential (E_{rp}), and cathodic kinetics. These results were aided by determination of a solubility curve as a function of temperature for a stoichiometric metal salt mixture of iron chloride ($FeCl_2$), chromium chloride ($CrCl_3$), and nickel chloride ($NiCl_2$). Based on these newly measured saturation concentrations, metal ion diffusivities were calculated. Overall, it was found that $(i \cdot x)_{sf}$ decreases with increasing chloride concentration and increases with increasing temperature. E_{rp} was determined to decrease with increasing concentration and increase with increasing temperature. When incorporated into the maximum pit size model, these experimental results yielded a small increase in maximum pit size with increasing bulk chloride concentrations and/or increasing temperature.

 [DOI: 10.1149/2.0451911jes]

Manuscript submitted March 25, 2019; revised manuscript received May 28, 2019. Published June 7, 2019. *This paper is part of the JES Focus Issue on Advanced Techniques in Corrosion Science in Memory of Hugh Isaacs.*

Type 300 stainless steels (SS) are used heavily in marine environments due to their overall excellent corrosion resistance.[1,2] Although characterized as a corrosion resistant alloy, the 300 grade SS are susceptible to localized corrosion in the presence of aggressive anion species, including chloride, which is the dominant anion in marine atmospheres. The stability of localized corrosion propagation is governed by the alloying elements in the sample of interest, the bulk environment (including oxidizing potential) and the critical chemistry within the pit cavity.[1]

Pitting corrosion involves localized metal oxidation creating metal cations in the pit cavity which results in low pH, high chloride concentrations due to hydrolysis reactions, electromigration of chloride, and the limited diffusion of these species out of the pit.[1,3] Critical conditions for pit stability and further propagation have been described by the repassivation potential (E_{rp}) and the pit stability product ($(i \cdot x)_{sf}$) where i is current density, x is pit depth and the subscript sf indicates the presence of a salt film.[2,4] E_{rp} is a lower bound of electrochemical potential below which propagation will no longer occur, and the pit will repassivate.[4] Galvele[5] originally showed that for a one-dimensional pit to sustain dissolution, the quantity $(i \cdot x)$ must exceed a critical value connected to the critical chemistry (pH) required to prevent oxide film formation. It is noted that Galvele's original formulism did not require the presence of a salt film on the surface of the alloy. If at a certain depth (x) the anodic dissolution current density (i) is insufficient to meet the pit stability criterion, the pit will repassivate because the critical chemistry will be lost to the bulk by diffusion. Pit stability is a battle between the production of acidity (via hydrolysis of metal cations produced by the dissolution current density, i) and diffusion of that concentrated solution to the bulk, which is controlled by the diffusion distance, x. Thus, a shallow pit requires a high current density to maintain stability, whereas a deeper pit requires lower current density.

Atmospheric exposure testing of SS in different environmental conditions has shown pit sizes reach a limiting value over time.[6–10] The complex process of pitting corrosion under freely corroding conditions has been previously modeled based on the inherent coupling between anodic and cathodic kinetics, and a brief summary of this method is included in the Appendix.[11] Simply put, the anodic dissolution at the base of the pit must have an associated cathodic current supply sufficient to meet the anodic current. However, in thin electrolyte conditions, ohmic drop considerations in the thin electrolyte film limit the cathodic current supply. Through the inherent coupling of the cathode and anode, a finite cathode therefore implies a finite anode, i.e., a finite pit size. Finding the maximum pit size can be achieved by determining: (a) the maximum cathode current the external surface can generate, and (b) the minimum dissolution current needed to maintain the critical chemistry in the pit as a function of the pit size. Combining these two relations results in an expression for the maximum pit size obtainable under the given conditions.

Pit sizes in exposure testing have been shown to be dependent upon both electrolyte composition and concentration and temperature in bulk solution.[2,12] In the framework of the maximum pit size model, this dependence implies that anodic and/or cathodic kinetics are dependent on temperature and chloride concentration. Anodic kinetics parameters ($(i \cdot x)_{crit}$, E_{rp}) have been explored as function of electrolyte composition (including chemical species and concentration)[4,12–25] and temperature.[14–18,22] However, as both dilute and concentrated salt solutions can be present on a metal surface when considering a wide range of temperatures and relative humidity in service conditions,[24] the parameter space for SS304L material has not been sufficiently explored to inform decisions about anodic kinetics.

Anodic metal dissolution can also lead to saturation in the pit of metal cations ($C_{M^{n+}}^{sat}$) and corresponding anions, generally chloride, leading to a diffusion limited current density through a metal salt film.[22] The saturation point not only impacts the pit stability product, but also impacts the repassivation characteristics of the pit. Although it is thought that the critical solution composition is substantially less than saturation,[14,25,26] much can be understood about pitting by consideration of saturation conditions. Experimental determination of the saturation concentration has been explored by multiple authors.[13,19,25,27–33] As a surrogate for pit chemistries, ferrous chloride ($FeCl_2$) has generally been used as SS alloys are iron-based.[13,22] The saturation point of $FeCl_2$ has been studied extensively as a function of temperature.[31–34] However, SS alloys contain considerable amounts of chromium and nickel which can impact saturation concentrations.[23,34] Assuming stoichiometric dissolution of SS304, iron-, chromium- and nickel-containing metal salts will form. As these metal salts will reach saturation during anodic pit growth at concentrations likely different than that of $FeCl_2$ alone, it is of importance to understand the behavior of the metal salt mixture.

*Electrochemical Society Member.
**Electrochemical Society Fellow.
[z]E-mail: rgk6y@virginia.edu

This page is intentionally left blank.